Ziyang Ju

A Filter Bank Based Reconfigurable Receiver Architecture for Universal Wireless Communications

kassel university press

This work has been accepted by the faculty of Electrical Engineering and Computer Science of the University of Kassel as a thesis for acquiring the academic degree of Doktor der Ingenieurwissenschaften (Dr.-Ing.).

Supervisor: Prof. Dr. Dirk Dahlhaus
Co-Supervisor: Prof. Dr. Hartmut Hillmer

Defense day: 24th March 2010

Bibliographic information published by Deutsche Nationalbibliothek
The Deutsche Nationalbibliothek lists this publication in the Deutsche Nationalbibliografie; detailed bibliographic data is available in the Internet at http://dnb.d-nb.de.

Zugl.: Kassel, Univ., Diss. 2010
ISBN print: 978-3-89958-906-1
ISBN online: 978-3-89958-907-8
URN: http://nbn-resolving.de/urn:nbn:de:0002-9074

© 2010, kassel university press GmbH, Kassel
www.upress.uni-kassel.de

Printed by: Unidruckerei, University of Kassel
Printed in Germany

Acknowledgements

I would like to express my deep thanks and appreciation to my supervisor Prof. Dirk Dahlhaus for supporting my work in all the years and guiding my research activities. I owe Prof. Hartmut Hillmer a debt of gratitude for accepting to be my second referee, reading the thesis and giving me valuable comments. Special thanks go to Dr. Thomas Hunziker for introducing me to the topic of time-frequency analysis, supporting me during the URANUS project, for important discussions and the great experience of writing common papers as well as his infinite tolerance and patience throughout the stages of this research. Furthermore, I would like to thank Prof. Klaus David for being member of the disputation committee and reviewing my thesis.

I am grateful to all the Communications Laboratory members, namely Herbert Lindenborn, Thomas Edlich, Marc Selig and our secretary Hannelore Abel for creating such a comfortable working environment.

Finally, I would like to express my deep gratitude to my parents for their support and understanding even though they are far away. My warmest thanks go to my husband Xiao for his endless love and continuous encouragement in the course of my PhD project.

Abstract

Motivated by the heterogeneity of today's world of wireless communications, there is a growing demand for terminals supporting different services and applications over a variety of networks. Reconfigurability is a key ingredient of such terminals in order to deliver optimal quality of service over diverse communication environments. We consider a reconfigurable baseband receiver architecture which is capable of dealing with signal formats from different existing and future air interfaces. The receiver employs signal processing in the time-frequency (TF) domain implemented by Discrete Fourier Transform (DFT) filter banks, which is a generalization of the block-wise frequency domain processing in orthogonal frequency-division multiplexing (OFDM) receivers.

The most challenging task for the reconfigurable receiver design is to handle dispersive channels in a uniform way when processing signals from different air interfaces. In cyclic prefix based OFDM systems the diagonalization of the time-invariant channel facilitates the practical implementation. We propose a TF domain channel diagonalization approach, which offers similar advantages as the aforementioned channel diagonalization in OFDM systems and, at the same time, can be applied to arbitrary types of signals. A central issue in the approach is the choice of a suitable so-called Gabor window function used for TF signal representation. Some properties of the overall approach, namely the freedom in the choice of the aforementioned Gabor window function and its scalability in time and frequency, facilitate the handling of diverse signal types. Furthermore, the design can be adapted to radio channels with different delay and Doppler spreads. We establish a general mathematical framework for window optimization minimizing the mean-squared sample error caused by the channel diagonalization under the assumption of a wide-sense stationary uncorrelated scattering impulse response of the considered wireless channel. With an enhanced scheme for the parameterization of tight Gabor frames, the design of the window function defining paraunitary filter banks is formulated as a convex optimization problem.

Finally, a matched filtering/equalizer based baseband receiver architecture employing the TF channel diagonalization is proposed which can be considered an important component for application in future reconfigurable radio systems. The bit-error rate performance and the computational complexity of the receiver are analyzed for the downlink in the universal mobile telecommunications system terrestrial radio access (UTRA) with direct-sequence spread-spectrum signalling (DSSS) and frequency division duplexing.

Contents

List of Figures

List of Tables

List of Abbreviations

ADC	**A**nalog-to-**D**igital **C**onverter
BER	**B**it-**E**rror **R**ate
CA	**C**omplex **A**ddition
CDMA	**C**ode-**D**ivision **M**ultiple **A**ccess
CM	**C**omplex **M**ultiplication
DAC	**D**igital-to-**A**nalog **C**onverter
DFT	**D**iscrete **F**ourier **T**ransform
DPCCH	**D**edicated **P**hysical **C**ontrol **CH**annel
DPCH	**D**edicated **P**hysical **CH**annel
DPDCH	**D**edicated **P**hysical **D**ata **CH**annel
DSSS	**D**irect-**S**equence **S**pread-**S**pectrum
DVB-T	**D**igital **V**ideo **B**roadcast **T**errestrial
FB	**F**ilter **B**ank
FDD	**F**requency **D**ivision **D**uplexing
FEC	**F**orward **E**rror **C**orrection
FFT	**F**ast **F**ourier **T**ransform
FIRST	**F**lexible **I**ntegrated **R**adio **S**ystems **T**echnology
GSM	**G**lobal **S**ystem for **M**obile communication
ISI	**I**nter-**S**ymbol-**I**nterference
IST	**I**nformation **S**ociety **T**echnologies
LMMSE	**L**inear **M**inimum **M**ean-**S**quared **E**rror
LTI	**L**inear **T**ime-**I**nvariant
LTV	**L**inear **T**ime-**V**ariant
MAI	**M**ultiple **A**ccess **I**nterference

ML	**M**aximum-**L**ikelihood
MLMMSE	**M**odified **L**inear **M**inimum **M**ean-**S**quared **E**rror
MSE	**M**ean-**S**quared **E**rror
OFDM	**O**rthogonal **F**requency-**D**ivision **M**ultiplexing
OVSF	**O**rthogonal **V**ariable **S**preading **F**actor
PHY	**PHY**sical layer
PR	**P**erfect **R**econstruction
QAM	**Q**uadrature **A**mplitude **M**odulation
RF	**R**adio **F**requency
RMS	**R**oot **M**ean **S**quared
RRC	**R**oot-**R**aised **C**osine
SDP	**S**emidefinite **P**rogramming
SDR	**S**oftware **D**efined **R**adio
SNR	**S**ignal-to-**N**oise **R**atio
TF	**T**ime-**F**requency
TFCI	**T**ransport **F**ormat **C**ombination **I**ndicator
TFR	**T**ime-**F**requency **R**epresentation
TPC	**T**ransmit **P**ower **C**ontrol
TRUST	**T**ransparently **R**econfigurable **U**biquitou**S** **T**erminals
UMTS	**U**niversal **M**obile **T**elecommunications **S**ystem
URANUS	**U**niversal **RA**dio-link platform for efficie**N**t **U**ser-centric acces**S**
US	**U**ncorrelated **S**cattering
UTRA	**U**niversal mobile **T**elecommunications system terrestrial **R**adio **A**ccess
WiMAX	**W**orldwide **i**nteroperability for **M**icrowave **A**ccess
WLAN	**W**ireless **L**ocal **A**rea **N**etwork
WSS	**W**ide-**S**ense **S**tationary
WSSUS	**W**ide-**S**ense **S**tationary **U**ncorrelated **S**cattering
2G	second-generation
3G	third-generation

List of Symbols

$\mathbf{A}$	pulse cross-correlation matrix
$c\,(t, \tau)$	time-continuous time-variant impulse response
$c\,[k, q]$	time-discrete time-variant impulse response
$C\,(t, f)$	time-continuous time-variant transfer function
$C\,(k, \omega)$	time-discrete time-variant transfer function
$d\,[k]$	impulse response of an analysis filter bank
$D_m\,(z)$	transfer function of the mth filter of an analysis filter bank
$\mathbf{D}_{\mathrm{P}}(z)$	polyphase matrix of an analysis filter bank
E	TF representation of the error from channel diagonalization
E_g	energy of the Gabor atom $g\,[k]$
g_{CO}	optimized window function via convex optimization
$g_{\ell,m}\,[k]$	Gabor atom $g\,[k]$ at the ℓth time slot and mth frequency slot
g_{rect}	window function with rectangular shape
g_{RRC}	Gabor atom with root-raised cosine shaped magnitude spectrum
g_{SDP}	optimized window function via semidefinite programming
$\mathcal{G}$	Gabor analysis operator based on atom $g\,[k]$
$G\,(z)$	z-transform of $g[k]$
H	TF domain channel parameter
$\mathcal{H}$	channel operator
i	index of the information symbol
$\mathbf{I}_N$	identity matrix of dimension $N \times N$
$\mathcal{I}$	identity operator
k, k', k''	sample indices of time-discrete signals

k_Δ	difference of time indices
K	number of sub-bands
ℓ, ℓ'	indices of time slots
m, m'	indices of frequency slots
N	down-sampling factor
N_0	spectral power density of $v[k]$
p	pilot signal
P	maximum polynomial order of matrix $\mathbf{W}_b(z)$ plus one
$\mathbf{P}$	TF representation of the pilot signal
q, q'	delay indices
Q	total number of the elementary waveforms
$\mathbf{R}_\mathrm{f}$	covariance matrix of the channel in frequency dimension
$\mathbf{R}_h$	covariance matrix of the channel
$\mathbf{R}_\mathrm{P}(z)$	polyphase matrix of the synthesis filter bank
$R\left(t_\Delta, f_\Delta\right)$	autocorrelation function of the time-variant transfer function
$\mathbf{R}_\mathrm{t}$	covariance matrix of the channel in time dimension
s	information symbol
$\hat{\mathbf{s}}_\mathrm{ML}$	ML estimate
$\hat{\mathbf{s}}_\mathrm{LMMSE}$	MMSE estimate
$\hat{\mathbf{s}}_\mathrm{ZF}$	ZF estimate
S_delay	delay power spectrum of the channel
S_Doppler	Doppler power spectrum of the channel
S_F	spreading factor
$S\left(\tau, \lambda\right)$	scattering function of the channel
$\mathcal{S}$	Gabor frame operator
$\mathcal{S}_T$	vector space of symmetric matrices of dimension T
u	sufficient statistic
$\mathbf{u}$	vector with components of sufficient statistics
v	additive front-end noise
$v_m\left[\ell\right]$	mth sub-band signal of the filter bank
$\mathbf{v}$	noise vector

$w_{\ell,m}[k]$	Gabor atom $w[k]$ at the ℓth time slot and mth frequency slot
$\mathbf{W}$	TF channel diagonalization error including thermal noise
$\mathcal{W}$	Gabor analysis operator based on atom $w[k]$
$x[k]$	channel input signal
X	TF representation of the channel input signal
$y[k]$	channel output signal
Y	TF representation of the channel output signal
z_q	qth elementary waveform
$\mathbf{Z}_q$	TF representation of the qth elementary waveform
ϵ_{T}	time domain MSE
ϵ_{TF}	TF domain MSE
τ_{RMS}	RMS delay spread
ϕ_{t}	time correlation function of the channel
ϕ_{f}	frequency correlation function of the channel
ν	index of Doppler dimension
ν_{RMS}	RMS Doppler spread
ω	index of frequency dimension
ω_{Δ}	difference of frequency indices
Ω	codebook for demodulation
$\|\cdot\|$	norm
$\odot$	element-wise multiplication
$E[\cdot]$	expectation
$\mathrm{tr}(\cdot)$	trace of a matrix
$\mathrm{Diag}[\mathbf{a}]$	diagonal matrix composed from the components of vector $\mathbf{a}$
$\mathrm{diag}[\mathbf{A}]$	vector constructed from the diagonal elements of $\mathbf{A}$
$\Re(\cdot)$	real part of complex arguments
$\Im(\cdot)$	imaginary part of complex arguments
$\lfloor x \rfloor$	$\max\{n \in \mathbb{Z} : n \leq x\}$
$\lceil x \rceil$	$\min\{n \in \mathbb{Z} : n \geq x\}$

Chapter 1

Introduction

1.1 Motivation

Wireless communications has become an inherent part of our everyday life and is still an active area of research and development. The area of wireless communications comprises a variety of different systems. The latter include, for example, satellite systems, cellular radio like the universal mobile telecommunications system (UMTS), radio access systems like Worldwide interoperability for Microwave Access (WiMAX) and wireless local area networks (WLANs), digital video broadcast (DVB), short-range radio like Bluetooth, wireless body area networks, sensor networks and others. The large number of the aforementioned systems and advanced wireless systems to be expected in the near future motivate a trend towards reconfigurable devices with multi-standard capabilities.

The growing demand of making terminals more flexible and adaptive, which can cope with today's and future air interfaces in an integrated fashion, comes from the following aspects. First of all, for different regions such as Europe, North America, and Asia, there are different wireless standards and spectrum allocation schemes employed. Secondly, when the users are able to access two or more systems with a single device in an efficient and seamless manner, they can freely choose different services and applications provided by such systems. Thirdly, compatibility with the existing standards and the upcoming ones should be ensured from an economic point of view. For example, terminals of a

third-generation (3G) network like UMTS are designed to also support second-generation (2G) networks like e.g. the global system for mobile communication (GSM) and to allow seamless dual-mode operation. Such devices play an important role in the transition period until the old standard is fully replaced.

A terminal which is able to operate independently of the specific environment is referred to as *universal*. With regard to the technology of universal terminals, the software-defined radio (SDR) concept is a presently popular approach towards reconfigurable system architectures for wireless networks and user terminals. The basic concept of SDR is to introduce flexible terminal reconfiguration by replacing radios completely implemented in hardware by ones that are configurable or even programmable in software [4, 5]. The SDR concept includes not only signal processing issues in the complex baseband like varying sampling rates, different filtering schemes and modulation/demodulation as well as encoding/decoding schemes, but also reconfiguration in the radio frequency (RF) front-end and in protocol layers above the physical layer (PHY). Clearly, these layers comprise radio resource management, networking issues and applications and services which lend themselves to a pure software implementation.

Reconfigurable systems require different support mechanisms to allow for dynamic air interface operation at the PHY [4]. The PHY of a wireless terminal usually contains the blocks for source and channel coding/decoding and the baseband system which is coupled via analog-to-digital (ADC) and digital-to-analog (DAC) converters, resp., with the RF front-end terminated by the antennas as shown in Fig. 1.1.

Ideally, the RF front-end of a reconfigurable system should be capable of fulfilling the RF specifications of the corresponding systems and, at the same time, be tunable over a wide range of frequency bands. In [6], RF front-end architectures and technologies for reconfigurable systems are discussed with applications to UMTS and WLAN standards. Apart from the flexible front-ends, an efficient baseband implementation of the PHY plays the key role in the design of universal terminals. The objective of the baseband reconfiguration of SDR is to adapt the functionality of the baseband transceiver chains. This means that the digital signal processing algorithms making up these chains are to be adapted so that their post-reconfiguration functionality satisfies the corresponding

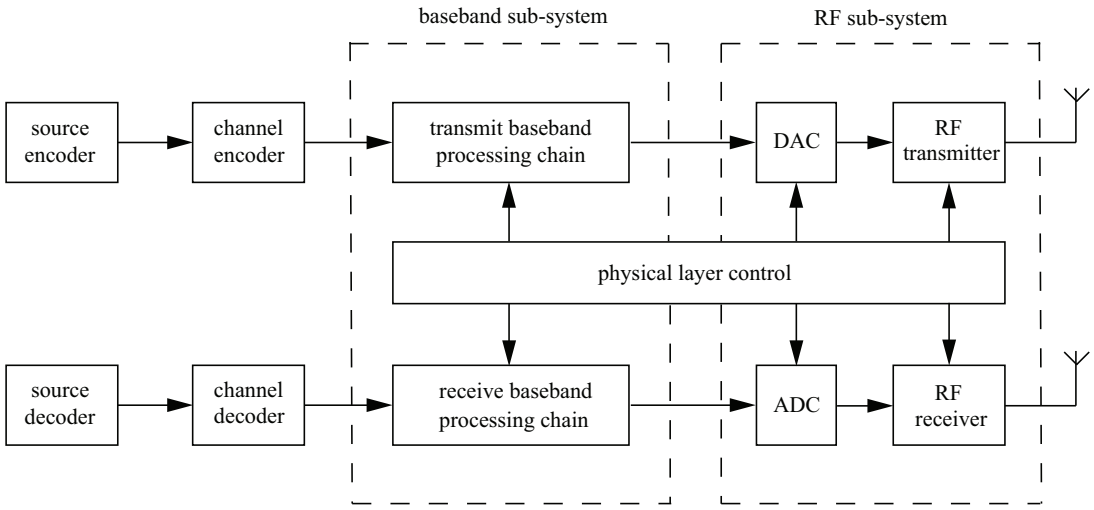

FIGURE 1.1: Typical signal processing blocks in the PHY of a wireless transceiver [4].

specifications [7]. Here, we concentrate primarily on the digital signal processing aspects of the receive baseband processing chain, which includes modulation/demodulation, signal detection algorithms, equalizers, etc. It is envisaged that baseband reconfigurations may involve a change in modulation, channel description, etc. This may be necessary if the terminal is to be reconfigured to support a different standard than the one currently in use.

Devices supporting multiple air interfaces in the form of parallel implementations of the baseband systems are widely available. In case of a parallel implementation, each separate wireless interface can be optimized within the supported standard and designed to include a dedicated set of functional blocks. The air interfaces encountered in today's access networks include single-carrier, spread-spectrum or multi-carrier modulation and are combined with different multiple-access schemes. Therefore, the parallel implementation of common modem functions for an increasing number of wireless interfaces to be supported becomes more and more inefficient which is particularly critical for portable terminals with their usually strict limitations in power consumption and required large stand-by times.

In view of the still increasing number of wireless standards, a more future-proof design approach is to adopt integrated solutions which can be implemented by a monolithic receiver architecture and which are capable of dealing with different signal formats. A

monolithic receiver enables a uniform processing of different signals by means of reconfigurable multi-purpose signal processing units. Reconfigurability is attained by a limited set of parameters that determine the operations of the receiver components. The use of fixed, efficiency-optimized signal processing components for the signal expansion, demodulation, channel estimation and decoding is expected to enable real-time operation. However, many technical challenges remain in designing reconfigurable receivers with a performance being sufficient for supporting future wireless applications.

1.2 State of the Art

The design of reconfigurable systems aims to provide a common platform for multiple air interfaces [4]. The Fourth Generation Mobile Forum, the Wireless World Research Forum, the Information Society Technologies (IST) project Transparently Reconfigurable UbiquitouS Terminals (TRUST) [8] and the IST program Network of Excellence in Wireless COMmunications (NEWCOM), among others, are all targeted to promote the integration of different evolving and emerging wireless access technologies into a common flexible and extendable platform, so as to provide multiple possibilities for current and future services and applications within a single terminal [9]. The European research project Flexible Integrated Radio Systems Technology (FIRST) shows that it is feasible to deploy intelligent multi-mode terminals via SDR technologies, capable of operation with multiple standards, with the ability to deliver multimedia services to mobile users [10]. Most of the SDR literature [4, 11] focuses on flexible radio front-ends, higher layer issues such as radio resource management, and architectural concepts. For the baseband system of the PHY, a pure SDR system usually has a list of baseband modules with various functionalities and implementing different algorithms. A piece of software needs to be downloaded to the terminal when handling the signal from a new air interface. For the signal demodulation and decoding, some form of hardware acceleration seems inevitable in view of the high complexity. Rather than by means of software download, reconfigurability can be enabled through parametric control of fixed receiver elements [12]. This is the concept we advocate in this work, with the fixed elements being filter banks (FBs) and Fast Fourier Transform (FFT) algorithms.

The transform of time-discrete signals into the time-frequency (TF) domain can be accomplished by Discrete Fourier Transform (DFT) FBs, for which similarly efficient FFT-based implementations are available as for plain DFTs [13]. Originally proposed for the application in speech compression, FBs are used for image processing, and more recently, in digital communication systems. Some of the latter applications include the design of oversampled modulated trans-multiplexers with perfect reconstruction (PR) FBs [14], FB precoding for channel equalization [15], the design of channel coding [16], blind equalization in wireless channels [17], and most importantly, generalized multi-carrier modulation in wireless communications [18, 19]. The DFT-based signal representation in conventional orthogonal frequency-division multiplexing (OFDM) receivers can be viewed as a special case where the prototype of the FBs has a rectangular shape. The block-wise Fourier transform used in OFDM is adequate only for signal processing in the context of linear time-invariant (LTI) systems, which preserve stationarity during the cyclic extensions of OFDM signals, but lacks desired frequency resolution in cases of linear time-variant (LTV) systems. Better results in this respect are obtained by FBs if based on a smoothly shaped analysis/synthesis window. Different analysis/synthesis windows of the aforementioned reconfigurable receiver can be tuned to the different standards to be supported.

A large amount of work has been done on FB design in the context of generalized multi-carrier/multi-tone modulation in wireless/wired communications. Replacing the block-wise inverse DFT and DFT in the transmitter and receiver, resp., leads to more general FBs which allow for operation without the rigid framework of rectangular windows and cyclic prefixes (CPs) in OFDM systems [20, 21]. Interference between adjacent sub-bands or multi-carrier symbols can be avoided, or at least substantially limited, by choosing appropriate transmit pulses. In [22], DFT FBs are designed to minimize interference, and good pulses for both transmitting filters and receiving filters are presented. At the receiver end the advantages over conventional OFDM include reduced susceptibility to Doppler spreads, frequency offsets, and phase noise [23]. Suitable detection methods for non-orthogonal multi-carrier signaling are discussed in [20, 24], while FBs for transmission over dispersive channels with limited inter-channel and inter-symbol interference are designed in [19, 25, 26]. In this work we are concerned with FB design for channel *diagonalization*

of *doubly dispersive* wireless channels, which is an important aspect for our design of the reconfigurable receiver.

As we know, the most difficult challenge for the design of a universal baseband receiver architecture is the signal distortion caused by the delay and Doppler dispersive radio channel as explained below. A signal propagating through a wireless channel experiences random fluctuations in time if the transmitter, receiver, or surrounding objects are moving, which is termed time selectivity or Doppler dispersion of the radio channel, respectively. Simultaneously, the multipath propagation leads to delay dispersion or frequency selectivity, respectively. Such channels are usually regarded as doubly dispersive in both delay and Doppler frequency. Hence, the characteristics of the channel makes it difficult to design reliable systems with guaranteed performance. For dealing with signal dispersion, fundamentally different approaches are followed in traditional radios depending on the type of modulation and bandwidth. Receivers for single-carrier signals typically model the channel as a tapped delay line [27]. From the appropriate coefficients, denoted as $q_0, \ldots, q_D$ in Fig. 1.2, the information in the transmitted signal can be recovered by means of a matched filtering followed by a sequence detector or using instead an equalizer followed by a simple detector [28]. Such a time domain channel model is often

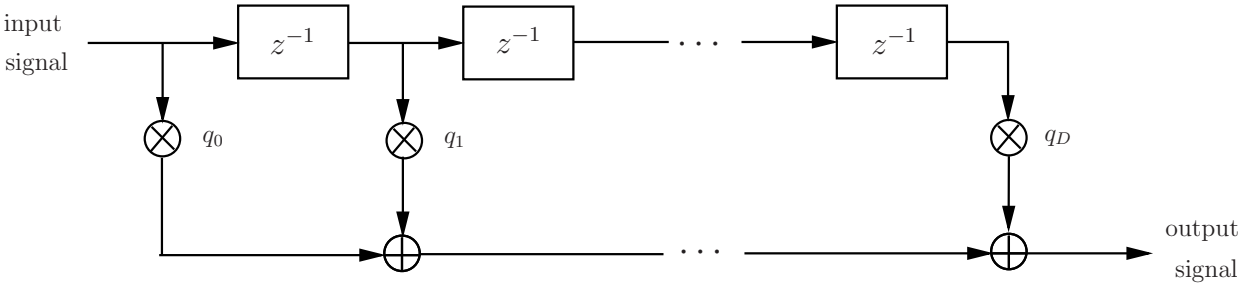

FIGURE 1.2: Representation of mappings by radio channels: time domain model.

used in Code-Division Multiple Access (CDMA) [29]. The complexity of the coefficient estimation and detection schemes increases with the delay dispersion and thus with the number of taps. OFDM can evade the need for complex equalizers in high data rate systems with a frequency domain channel model [30]. The cyclic extensions in OFDM

signals and the frequency domain channel model facilitate a diagonalization of the channel operators. In the case of sufficiently *underspread* channels, this scheme approximately diagonalizes the time-variant multipath channel. This channel *diagonalization* enables straightforward demodulation and coefficient estimation and has, along with the availability of FFT algorithms, led to the popularity of OFDM. Indeed, there are numerous applications of OFDM which range from digital audio and video broadcasting to WLAN standards.

While the concept of OFDM receivers requires a CP and a transmission over essentially time-invariant channels, these limitations can be overcome by resorting to alternative signal representations, in particular so-called TF signal representations. Most time-frequency representations (TFRs) are time-variant spectral representations which are conceptually similar to a musical score with the time running along one axis and instantaneous frequency along the other axis [31]. This kind of signal decomposition plays an important role in mathematics, physics and engineering [32]. One of the most interesting applications of TFR is in the area of wireless communications. For a linear signal space, which is a collection of signals such that any linear combination of two elements is again an element of the space, we consider the subspace $L^2(\mathbb{Z})$ which is equipped with an inner product. While the Fourier transform is adequate for the analysis of stationary signals, TFRs are often more appropriate for revealing the TF characteristics of transient signals. There are two main classes of TFRs, namely quadratic TFRs and linear TFRs. Linear TFRs, which include the short-time Fourier transform, the wavelet transform [33], and the Gabor transform [34], are of prime interest since they obey the superposition principle.

In [35], it is shown that signal analysis and synthesis via Gabor frames are efficiently implemented by DFT FBs while tight Gabor frames are related to paraunitary FBs. We concentrate on tight frames, which are the generalizations of orthonormal bases [36], and the corresponding paraunitary FBs. Optimal FBs may be found for certain constraints, namely when the design problem can be formulated as a convex optimization (CO) problem [26], as in [37] for the design of a two-channel multirate FB. CO methods are also employed in [38] for the design of pulse shapes which minimize inter-carrier

interference due to frequency offsets in OFDM systems, in [39] for the design of prototype filters for filtered multi-tone modulation used in digital subscriber line systems, and in [40] for the design of FBs for sub-band signal processing under minimal aliasing and induced distortion. Semidefinite programming (SDP), a branch of CO for which efficient numerical solution methods are available, has been employed in [41] for the design of a linear-phase prototype filter with high stop-band attenuation for cosine-modulated FBs. In [42], two-channel FBs are optimized by SDP where the optimization is based on similar objective functions as in [41]. The optimization of orthonormal FBs for noise-suppression applications via CO is discussed in [43].

1.3 Thesis Contribution

The main subject of the thesis is the design of a reconfigurable baseband receiver architecture with multi-standard capabilities. The baseband receiver supports air interfaces defined in various standards and standard extensions, and it is adapted to different air interfaces without the need of software download, which can be viewed as an alternative to SDR. Furthermore, it can be easily upgraded to future standards and even personalized communications where the involved peers of the communication link, rather than a wireless standard, define the signalling parameters (user-defined modes). In fact, the adaptability of the receiver can also be attained in response to changing environmental (channel) characteristics and interference phenomena.

The configuration to different modes is achieved by representing each mode uniquely using a corresponding set of parameters. The choice of parameters describing each mode translates the corresponding operational requirements into a corresponding reconfigurable receiver architecture. The proposed baseband receiver has a fixed overall structure, thus maintaining the efficiency and compactness of hardware. Moreover, with the parametric control, we can typically attain a flexibility similar to a SDR approach.

Fig. 1.3 shows the related concepts for designing the reconfigurable receiver. The four blocks illustrated in the figure are different aspects investigated in this thesis, which are

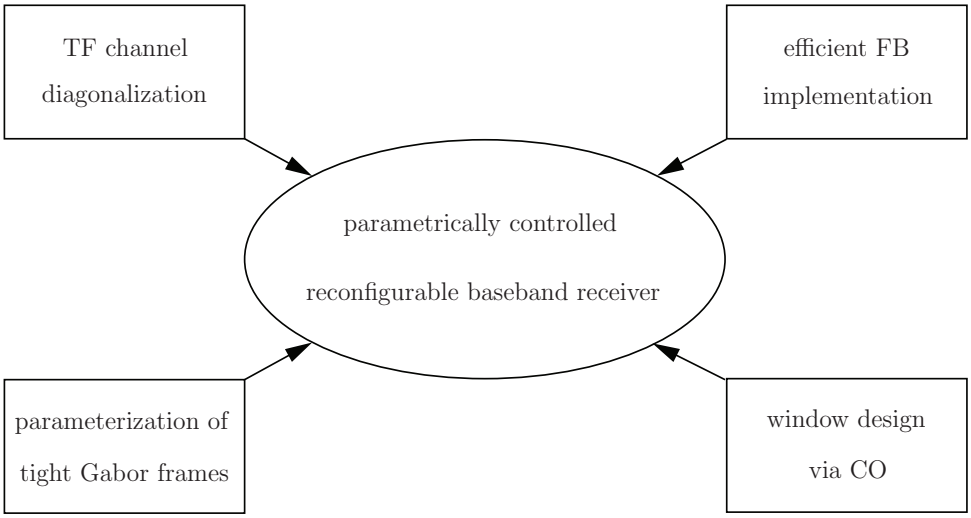

FIGURE 1.3: Related concepts for the design of a reconfigurable baseband receiver.

required for a reconfigurable baseband receiver design. Among them, the most important concept is the channel diagonalization model in the TF domain based on Gabor theory of signal representations, which allows signal receptions over doubly dispersive channels to be processed by the receiver. The natural choice for the signal transform is the time-discrete Gabor expansion [44] based on a system of TF shifted versions of a certain window function. Even though this TF domain channel diagonalization is approximative in the general case of time-variant channels and aperiodic signals, for the typical underspread channels encountered in mobile radio scenarios, the inherent model error can be limited to a usually acceptable level by choosing an adequate window underlying the signal transform [45, 46].

Another essential aspect is the design of optimized windows underlying the FBs of different channel characteristics. By extending the work of parameterization of tight Gabor frames in [47], we constrain the DFT FBs to be paraunitary. We use time and TF domain errors of the channel diagonalization as objective functions. With the PR condition of the paraunitary FBs transformed to the time domain, the design of paraunitary FBs is formulated as a CO problem involving suitable relaxations. Although CO methods are widely employed for the design of different types of FBs [39, 40], our contribution is the use of CO methods for the design of paraunitary FBs minimizing the aforementioned TF channel diagnolization error.

Finally, a reconfigurable architecture of the baseband receiver has been developed which makes use of FBs for the sake of efficient signal synthesis and analysis. The parametric configurations of the signal processing units of the receiver associated with certain modes are discussed, together with the performance evaluation and complexity analysis.

1.4 Outline of the Thesis

In Chap. 2, the mathematical concepts of the TF representation and processing of signals are introduced. Oversampled DFT FBs with PR capability are characterized in the polyphase domain. For paraunitary FBs, the window function defining a tight Gabor frame is properly parameterized. The signal transform associated with time-discrete tight Gabor frames fulfills Parseval's identity. This property is crucial for reconfigurable receivers as it lets the correlation between two time domain signals be computed based on the respective TF signal representations.

A TF channel diagonalization is proposed in Chap. 3, where we model the signal distortion in wide-sense stationary uncorrelated scattering (WSSUS) channels in a way compatible with the Gabor expansion. A main concern of this chapter is the design of tight Gabor frames facilitating TF domain channel diagonalization with minimal model error for given channel conditions. More specifically, we minimize the mean-squared error (MSE) resulting from the diagonalization of random channels with known second-order statistical properties, complying with the WSSUS model. Window functions minimizing the MSE appearing in both the TF and time domains are obtained via CO. Finally, the optimized window functions are presented for different scenarios and their MSE performance is investigated.

Chap. 4 describes a reconfigurable baseband receiver employing the TF domain channel diagonalization presented in Chap. 3. It is shown that the proposed receiver can be configured to both matched filtering and equalizer based receivers. Oversampled DFT FBs discussed in Chap. 2 are important elements of the reconfigurable receiver since they allow the signal processing to be accomplished in the TF domain. The receiver

architecture is addressed with a description of each functional block. Moreover, the channel estimation and detection algorithms are described in detail.

In Chap. 5, the baseband receiver configurations for signals from different legacy systems are shown, e.g. for OFDM and UMTS signals. In particular, the receiver configuration for UMTS signals is discussed in detail, where the optimized window is adapted to different channel characteristics, and the performance is compared against a conventional matched filtering receiver. Furthermore, some of the related issues of the multi-mode transceiver investigated in the European project Universal RAdio-link platform for efficieNt User-centric accesS (URANUS) conducted from 2006 until 2008 are summarized.

Chap. 6 gives a summary of the thesis and an outlook to some further research activities.

1.5 Notation

We enclose the arguments of functions defined on a discrete domain Λ in square brackets in order to distinguish them from functions defined on $\mathbb{R}^n$, e.g. $g[i]$ with $i \in \Lambda$. The Hilbert space of square summable functions $f : \Lambda \rightarrow \mathbb{C}$ is denoted as $L^2(\Lambda)$, and the associated inner product $\langle f, g \rangle$ and L^2-norm $\|f\|$ are given by $\sum_{i \in \Lambda} f[i]g^*[i]$ and $\sqrt{\langle f, f \rangle}$, resp., where the asterisk in the superscript denotes complex conjugation. Furthermore, we use $\odot$ to denote the element-wise multiplication of two functions f and g with $f, g : \Lambda \rightarrow \mathbb{C}$, i.e., $h = f \odot g$ corresponds to $h[i] = f[i]g[i]\ \forall i \in \Lambda$. Vectors are represented using lowercase and matrices using uppercase boldface characters, respectively. The transpose and Hermitian transpose of a matrix $\mathbf{A}$ are denoted as $\mathbf{A}^{\mathrm{T}}$ and $\mathbf{A}^{\mathrm{H}}$, resp., $\mathrm{tr}(\cdot)$ represents the trace, and $\mathbf{I}_N$ denotes the identity matrix of size $N \times N$. The vector obtained from $\mathbf{A}$ by stacking its columns is denoted as $\mathrm{st}\,[\mathbf{A}]$, $\mathrm{Diag}\,[\mathbf{a}]$ represents the diagonal matrix composed from the components of the vector $\mathbf{a}$, and $\mathrm{diag}\,[\mathbf{A}]$ the vector constructed from the diagonal elements of $\mathbf{A}$. The paraconjugate of a polynomial matrix $\mathbf{A}(z)$ is represented as $\widetilde{\mathbf{A}}(z)$, and it is obtained from $\mathbf{A}(z)$ by transposing it, conjugating all of the coefficients of the rational functions in $\mathbf{A}(z)$, and replacing z by z^{-1} [13]. The nth element of the mth row of a matrix $\mathbf{A}$ is represented as $[\mathbf{A}]_{m,n}$. We also use $\odot$ to denote the element-wise multiplication of two matrices $\mathbf{A}$ and $\mathbf{B}$ of size $M \times N$, i.e.

$[\mathbf{A} \odot \mathbf{B}]_{m,n} = [\mathbf{A}]_{m,n}[\mathbf{B}]_{m,n}$. Furthermore, $E[\cdot]$ denotes the expected value, $\Re(\cdot)$ and $\Im(\cdot)$ represent the real and imaginary part, resp., of complex arguments, mod the modulo operation, $\jmath \triangleq \sqrt{-1}$, $\lfloor x \rfloor \triangleq \max\{n \in \mathbb{Z} : \ n \leq x\}$, and $\lceil x \rceil \triangleq \min\{n \in \mathbb{Z} : \ n \geq x\}$.

Chapter 2

Time-Frequency Signal Representation Concepts

2.1 Introduction

In this chapter, concepts for the TF representation of signals are introduced. The mathematical operations as well as the discussed implementations of these operations using FBs provide the basis for the reconfigurable receiver techniques presented in the following chapters. TFRs combine a temporal analysis and a spectral analysis of signals by representing signals using their TF coordinates. Linear and quadratic TFRs are two important classes of TFRs. Linear TF signal representations satisfy the superposition principle, which states that if the signal $x(t)$ is a linear combination of some signals then the TFR of $x(t)$ corresponds to the linear combination of the respective TFRs. A quadratic TF signal representation involves the signal in a quadratic form, describing the energy distribution or the joint TF correlation of the signal.

Gabor analysis is a branch of TF analysis which deals with linear TFRs, being concerned with the use of discrete coherent families [32]. Such families are obtained by shifting a given atom (or window) function in time and frequency. The resulting family of TF-shifted replicas can be used for the transform of a time domain signal into the TF domain.

The so-called *Gabor transform* is accomplished by projecting the time domain signal onto the aforementioned family.

The transform of time-discrete signals into the TF domain can be accomplished by DFT FBs, for which similarly efficient FFT-based implementations are available as for plain DFTs [13]. There is a close relationship between a number of mathematical concepts from Gabor analysis and elements from FB theory, a branch of digital signal processing. Dual Gabor frames, for instance, relate to PR FBs, while tight Gabor frames relate to paraunitary FBs [35].

Moreover, *tight frames* can be seen as natural generalizations of orthonormal bases which are used for instance for the signal representation in OFDM systems. In this work we are interested exclusively in tight Gabor frames and related paraunitary FBs since the associated signal transform fulfills Parseval's identity. This property is crucial for flexible receivers discussed in Chap. 4.

In Sect. 2.2, the mathematical concepts for TFR and TF processing of signals are introduced. Oversampled DFT FBs, which efficiently implement Gabor frame expansions, are discussed in Sect. 2.3. A parameterization of tight Gabor frames, needed for the constraint optimization in Sect. 3.6, is presented in Sect. 2.4.

2.2 Fundamentals of Gabor Analysis

In 1946, Gabor proposed a method to represent a one-dimensional signal in two dimensions, with time and frequency as coordinates [48]. In what was later named the Gabor expansion, a signal is expanded by means of a family of elementary functions, each of which is obtained from a certain so-called Gabor atom by translation in time and modulation in frequency [32]. While originally conceived for continuous signals, the same concept can be applied to discrete signals [44]. In the following, we will focus on the time-discrete case.

Let N and K be two positive integer constants and $\Lambda \triangleq \mathbb{Z} \times \{0, \ldots, K-1\}$. Given an atom $g \in L^2(\mathbb{Z})$, the set

$$\{g_{\ell,m}[k] : (\ell, m) \in \Lambda\} \tag{2.1}$$

with

$$g_{\ell,m}[k] \triangleq g[k - \ell N] \exp(\jmath 2\pi (k - \ell N) m/K) \tag{2.2}$$

is referred to as a (time-discrete) *Gabor system* in $L^2(\mathbb{Z})$. The elements of the Gabor system can be seen as relating to the grid points $\{(\ell N, 2\pi m/K) : (\ell, m) \in \Lambda\}$ of a lattice overlaying the TF[1] plane $\mathbb{Z} \times [0, 2\pi)$. As shown in Fig. 2.1, the element $g = g_{0,0}$ is localized in the origin and its time shifted and frequency modulated version $g_{\ell,m}$ is localized at $(\ell N, \frac{2\pi m}{K})$.

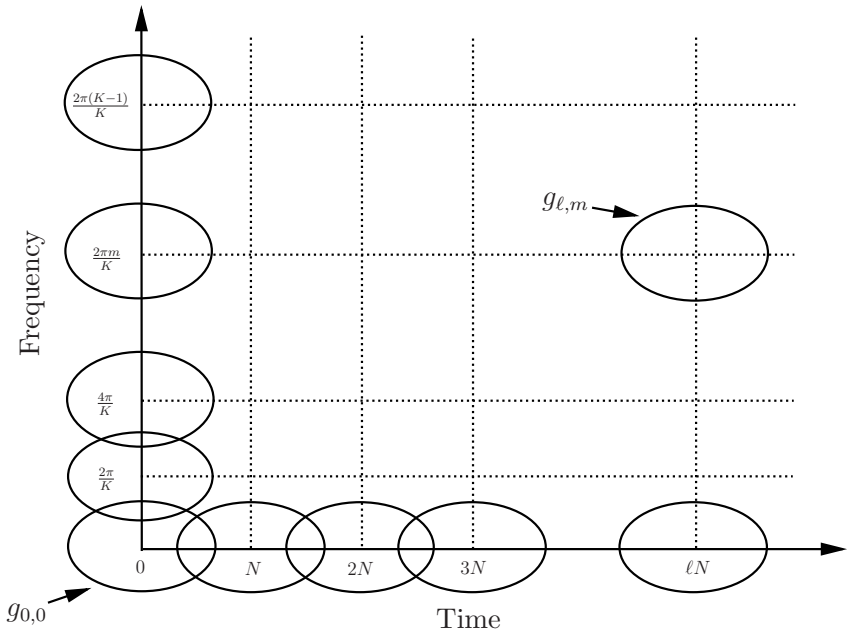

FIGURE 2.1: Elements of a Gabor system in the TF plane.

The size of the TF lattice determines the sampling density in the TF plane. The Gabor system $\{g_{\ell,m}[k] : (\ell, m) \in \Lambda\}$ can be classified according to the sampling density of the TF lattice [32]:

- *Overcritical sampling* ($N < K$): The elements of $\{g_{\ell,m}[k] : (\ell, m) \in \Lambda\}$ are linearly dependent, and the oversampling rate of the Gabor system equals K/N.

[1]With a slight abuse of notation, we will not distinguish between frequency and angular frequency in the following, where the domain of the latter is defined as $[0, 2\pi)$.

- *Critical sampling* ($N = K$): Gabor systems $\{g_{\ell,m}[k] : (\ell, m) \in \Lambda\}$ consisting of linearly independent elements are possible.

- *Undercritical sampling* ($N > K$): The Gabor family is incomplete in the sense that the linear span of $\{g_{\ell,m}[k] : (\ell, m) \in \Lambda\}$ is a proper subspace of $L^2(\mathbb{Z})$.

In this work we consider Gabor systems with $N/K \leq 1$, which is a necessary condition for *Gabor frames*. To discuss the properties of Gabor frames we shall recall the definitions of bases and frames. A sequence $e_1, e_2, \ldots$ is a basis for a Hilbert space with a countably infinite number of dimensions if the following conditions are satisfied:

- The elements $e_1, e_2, \ldots$ span the Hilbert space, i.e., every element f in the Hilbert space can be represented as
$$f = \sum_{j=1}^{\infty} a_j e_j, \tag{2.3}$$
where $a_1, a_2, \ldots$ are scalar coefficients.

- $e_1, e_2, \ldots$ are linearly independent.

Furthermore, $\{e_j : j \in \mathbb{N}\}$ is an *orthonormal basis* if $\langle e_i, e_j \rangle = \delta_{i,j}$, where $\delta_{i,j}$ denotes the Kronecker delta function. In this case the coefficients are easily found as $a_j = \langle f, e_j \rangle$, $j \in \mathbb{N}$.

If there exist two positive constants A_0 and B_0 such that

$$A_0 \|f\|^2 \leq \sum_{j \in \mathbb{N}} |\langle f, e_j \rangle|^2 \leq B_0 \|f\|^2, \tag{2.4}$$

for every f in the Hilbert space, then $\{e_j : j \in \mathbb{N}\}$ represents a frame [36]. The numbers A_0 and B_0 are the lower and upper frame bounds, respectively. The elements of a frame are not necessarily linearly independent. It may be possible to remove elements from a frame without losing property (2.4). If so, given f, the expansion $f = \sum_{j \in \mathbb{N}} a_j e_j$ is not unique. A frame is said to be *exact* if the removal of any element results in a family which does not span the entire Hilbert space anymore. A sequence $e_1, e_2, \ldots$ is in fact an exact frame if and only if it is a *Riesz basis* [36]. In a Hilbert space a Riesz basis is

related to an orthonormal basis in the sense that the Riesz basis can be obtained from the orthonormal basis by means of a bounded and invertible operator.

If $A_0 = B_0$, $\{e_j : j \in \mathbb{N}\}$ is called a *tight frame*, and in this case

$$\sum_{j\in\mathbb{N}} |\langle f, e_j\rangle|^2 = A_0\|f\|^2. \tag{2.5}$$

Every element in the Hilbert space can be represented as a linear combination of the elements of a tight frame in analogy to (2.3).

Clearly there are many choices of g, N and K such that $\{g_{\ell,m}[k] : (\ell, m) \in \Lambda\}$ represents a frame or even an orthonormal basis for $L^2(\mathbb{Z})$. As an example for an orthonormal basis, let the atom g have the form of a rectangular window with size N and $N = K$. However, as commonly known such rectangularly shaped signals have low resolution in the frequency domain. The difficulty in designing orthonormal bases (or Gabor frames with $N = K$) comprising elements with high resolution in both time and frequency is expressed formally by the Balian-Low Theorem [18, 32]. In fact, the inherent difficulty of such bases or Gabor frames, discussed in detail in [49], can be overcome by resorting to an over-critical sampling. Thus, useful Gabor frames are often overcomplete. The greater design freedom with Gabor frames at $N/K < 1$ as compared to orthonormal bases offers advantages in many applications in signal and also image processing.

For an arbitrary signal $x \in L^2(\mathbb{Z})$ the inner products of $x[k]$ with every element of a Gabor system (2.1) form a linear TF representation. In the following, the corresponding transform onto $L^2(\Lambda)$ is represented by the analysis operator

$$\mathcal{G} : x \mapsto \mathcal{G}x = \langle x, g_{\ell,m}\rangle, \quad (\ell, m) \in \Lambda, \tag{2.6}$$

where $X[\ell, m] = \mathcal{G}x$ is sometimes called a Gabor coefficient. Conversely, a synthesis operator $\mathcal{G}^*$ can be defined based on (2.1) which maps an arbitrary TF representation $Y \in L^2(\Lambda)$ onto an element of $L^2(\mathbb{Z})$ according to

$$\mathcal{G}^* : Y \mapsto \mathcal{G}^*Y = \sum_{(\ell,m)\in\Lambda} Y[\ell, m]\, g_{\ell,m}[k]. \tag{2.7}$$

The analysis operator $\mathcal{G}$ and synthesis operator $\mathcal{G}^*$ are linear operators and they are adjoint with respect to the inner product operation. If (2.1) defines a Gabor frame, then there is a so-called *Gabor frame operator* $\mathcal{S} \triangleq \mathcal{G}^*\mathcal{G}$. Explicitly,

$$\mathcal{S} : x \mapsto \mathcal{S}x = \sum_{(\ell,m)\in\Lambda} \langle x, g_{\ell,m}\rangle g_{\ell,m}. \tag{2.8}$$

The Gabor frame operator $\mathcal{S}$ is a bounded invertible operator subject to

$$A_0 \leq \|\mathcal{S}\| \leq B_0. \tag{2.9}$$

Furthermore,

$$w = \mathcal{S}^{-1}g \tag{2.10}$$

is called the *canonical dual* window of g. The window w defines another Gabor frame $\{w_{\ell,m}[k] : (\ell, m) \in \Lambda\}$ with

$$w_{\ell,m}[k] \triangleq w[k - \ell N] \exp(\jmath 2\pi(k - \ell N)m/K), \tag{2.11}$$

and the associated analysis and synthesis operators $\mathcal{W}$ and $\mathcal{W}^*$, respectively. The two frames defined by g, w, N, and K are a dual pair of frames because

$$x = \mathcal{W}^*(\mathcal{G}x) = \sum_{(\ell,m)\in\Lambda} \langle x, g_{\ell,m}\rangle w_{\ell,m} \quad \forall x \in L^2(\mathbb{Z}). \tag{2.12}$$

In [34] several examples of dual windows with different lattice parameters are shown.

Moreover, if $\{g_{\ell,m}[k] : (\ell, m) \in \Lambda\}$ is a tight frame, then the dual window has the form $w[k] = cg[k]$ for some constant $c > 0$ [36]. Therefore, in case of tight Gabor frames, (2.12) can be rewritten as

$$x = c\,\mathcal{G}^*(\mathcal{G}x) \quad \forall x \in L^2(\mathbb{Z}), \tag{2.13}$$

where the constant c equals $\frac{1}{A_0}$. Hence, the Gabor frame operator is given as $\mathcal{S} = A_0\mathcal{I}$ with $\mathcal{I}$ denoting the identity operator on $L^2(\mathbb{Z})$, and

$$x = \frac{1}{A_0} \sum_{(\ell,m)\in\Lambda} \langle x, g_{\ell,m}\rangle g_{\ell,m} \quad \forall x \in L^2(\mathbb{Z}). \tag{2.14}$$

The signal representation using tight frames (2.14) shows great similarity with using orthonormal bases: the difference is that the elements of a tight frame are not necessarily linearly independent, which implies that tight frames are a generalization of orthonormal bases [36]. One of the advantages of tight frames is that the canonical dual frame of the tight frame $\{g_{\ell,m}[k] : (\ell,m) \in \Lambda\}$ with frame bound A_0 is simply given as $\{\frac{1}{A_0} g_{\ell,m}[k] : (\ell,m) \in \Lambda\}$, which is shown in (2.14). When $A_0 = B_0 = 1$, $\{g_{\ell,m}[k] : (\ell,m) \in \Lambda\}$ represents a normalized tight frame. This special Gabor frame is also sometimes called *Parseval* frame since it fulfills Parseval's identity

$$\|x\|^2 = \|\mathcal{G}x\|^2 \quad \forall x \in L^2(\mathbb{Z}). \tag{2.15}$$

Furthermore, the inner product $\langle x, y\rangle$ of any two $x, y \in L^2(\mathbb{Z})$ can be computed on the basis of the respective TF representations $\mathcal{G}x$ and $\mathcal{G}y$, that is,

$$\langle x, y\rangle = \langle \mathcal{G}x, \mathcal{G}y\rangle \quad \forall x, y \in L^2(\mathbb{Z}). \tag{2.16}$$

Henceforth we assume that (2.1) represents a normalized tight Gabor frame. In this case, it is clear that $\mathcal{G}^*\mathcal{G}$ is an identity operator on $L^2(\mathbb{Z})$. The operator $\mathcal{G}\mathcal{G}^*$, on the other hand, represents the *orthogonal projection* from $L^2(\Lambda)$ onto $\mathcal{F}_g \triangleq \{(\mathcal{G}x)[k] : x \in L^2(\mathbb{Z})\}$. When $N/K < 1$, the vector space $\mathcal{F}_g$ is a proper subset of $L^2(\Lambda)$, i.e., $\mathcal{F}_g \subset L^2(\Lambda)$. Fig. 2.2 illustrates the orthogonal projection of X onto $X_g = \mathcal{G}\mathcal{G}^*X$, where the vector space $\mathcal{F}_g$ is represented as a one-dimensional space having the form a straight line through the origin of $L^2(\Lambda)$.

It is obvious that

$$\|\mathcal{G}^*X\|^2 \leq \|X\|^2 \quad \forall X \in L^2(\Lambda). \tag{2.17}$$

We further note that the mapping $\mathcal{G} : L^2(\mathbb{Z}) \to \mathcal{F}_g$ is an isometry, and $\|g\|^2 = N/K$. The properties (2.15) and (2.16) of tight Gabor frames are of prime interest since they let operations for the signal demodulation at the reconfigurable receiver, such as signal energy computations and cross-correlations with reference waveforms, be performed directly in the TF domain.

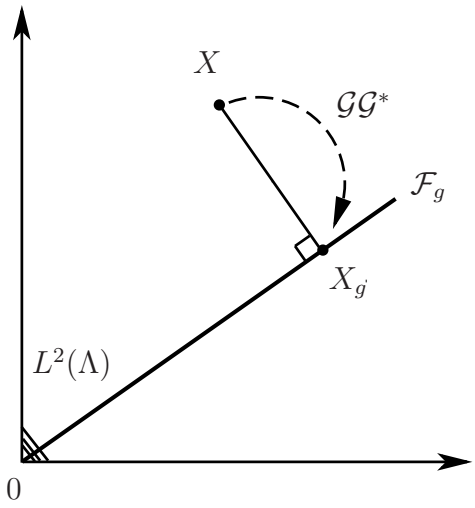

FIGURE 2.2: Orthogonal projection of $X \in L^2(\Lambda)$ onto $\mathcal{F}_g$.

2.3 Oversampled DFT Filter Banks

For an efficient computation of TFRs of time-discrete signals on a digital signal processor, FBs can be employed. Fig. 2.3 shows the notations used in the following to draw the digital FB diagrams. Uniform FBs are FBs with the same decimation factor in each sub-

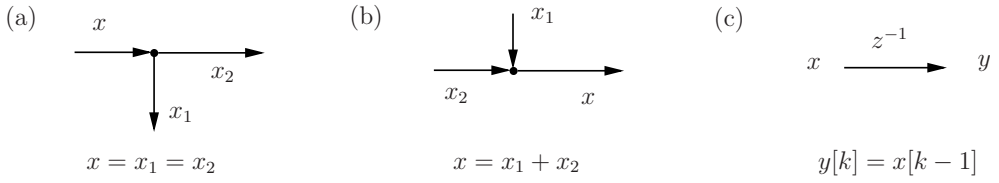

FIGURE 2.3: (a) A node that branches out, (b) adder, (c) delay element.

band. Signal expansions using uniform FBs with the decimation factor N equal to the number of sub-bands K, which are called maximally decimated or critically sampled FBs, are discussed in [13]. FBs with $N < K$, on the other hand, are referred to as oversampled FBs, and they are often the preferred option due to the greater design freedom.

Fig. 2.4 depicts a K-channel oversampled FB. The analysis FB splits the input signal $x[k]$ into K sub-bands by a bank of possibly non-causal, either finite impulse response or infinite impulse response filters with passband characteristics followed by a down-sampling. The filters are defined by the transfer functions $D_m(z), m = 0, \ldots, K-1$, that is, the z-transforms of the impulse responses $d_m[k], m = 0, \ldots, K-1$. An important class

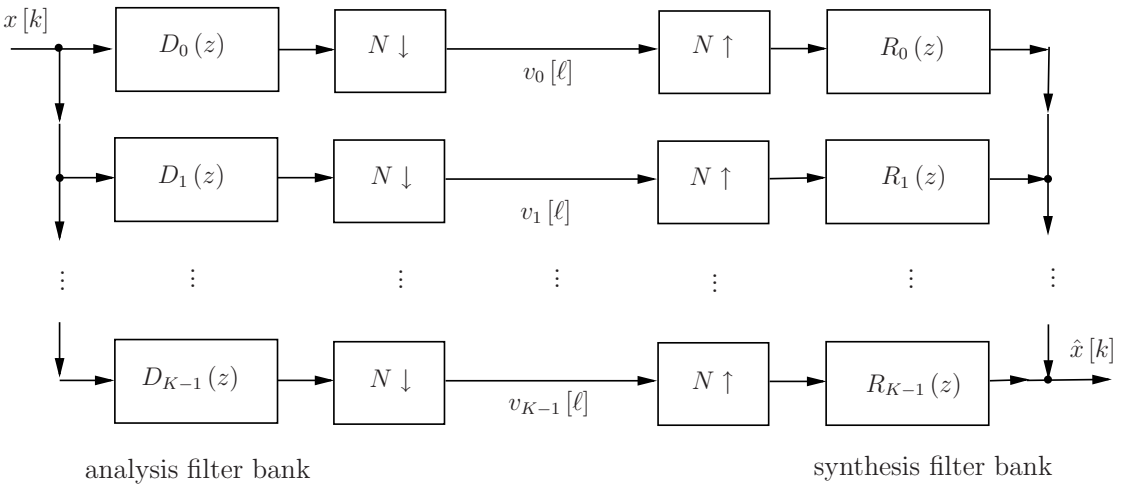

FIGURE 2.4: K-channel oversampled FB.

of uniform FBs are DFT FBs, where the impulse response of the mth filter is given by $d_m[k] = d[k]\,\mathrm{e}^{\jmath 2\pi km/K}$ with $d[k]$ denoting the impulse response of the analysis prototype filter. The down-sampler, also called N-fold decimator, reduces the output sampling rate by a factor N. The resulting sub-band signals, denoted as $v_0[\ell], \ldots, v_{K-1}[\ell]$, are given by

$$v_m[\ell] = \sum_{k=-\infty}^{\infty} x[k]\, d_m[\ell N - k], \quad m = 0, \ldots, K-1. \tag{2.18}$$

With $d_{\ell,m}[k] = d_m^*[\ell N - k], m = 0, \ldots, K-1$, (2.18) can further be written as

$$v_m[\ell] = \langle x, d_{\ell,m} \rangle, \quad m = 0, \ldots, K-1. \tag{2.19}$$

The subsequent synthesis FB usually aims to reconstruct the signal $x[k]$ from the sub-band signals $v_m[\ell], m = 0, \ldots, K-1$. In general, the output of the synthesis FB is given as

$$\hat{x}[k] = \sum_{m=0}^{K-1} \sum_{\ell=-\infty}^{\infty} v_m[\ell]\, r_m[k - \ell N], \tag{2.20}$$

where in the case of DFT FBs $r_m[k] = r[k]\mathrm{e}^{\jmath 2\pi km/K}$ denotes the impulse response of the mth synthesis filter with $r[k]$ representing the impulse response of the synthesis prototype filter. With $r_{\ell,m}[k] = r_m[k - \ell N]$, the signal $\hat{x}[k]$ is given by

$$\hat{x}[k] = \sum_{m=0}^{K-1} \sum_{\ell=-\infty}^{\infty} \langle x, d_{\ell,m} \rangle\, r_{\ell,m}[k]. \tag{2.21}$$

The transfer functions of the synthesis filters are denoted as $R_0(z), \ldots, R_{K-1}(z)$ in Fig. 2.4.

2.3.1 Relationship between Oversampled DFT Filter Banks and Discrete Gabor Frames

As suggested by (2.21), there is a close relationship between the analysis and synthesis operations based on Gabor frames on the one hand, and the signal transforms by DFT analysis and synthesis FBs on the other hand. Clearly, the lattice constants underlying the Gabor expansion can be regarded as corresponding to the down-sampling factor and the number of sub-bands of an oversampled DFT FB. Furthermore, a one-to-one relationship can be established between the atom $g[k]$ of a Gabor frame and the impulse response $d[k] = d_0[k]$ of the analysis prototype filter according to

$$g[k] = d^*[-k], \tag{2.22}$$

as well as between the Gabor coefficients and the FB sub-band signals, i.e.,

$$X[\ell, m] = v_m[\ell]. \tag{2.23}$$

A similar relationship applies to the synthesis operations. Given (2.23), the signal obtained from a synthesis FB with a prototype filter having impulse response $r[k] = r_0[k]$ equals the result of a synthesis operation (2.7) based on a Gabor frame with atom

$$w[k] = r[k]. \tag{2.24}$$

Tab. 2.1 summarizes the relationships between oversampled DFT FBs and Gabor frames.

Hence, the Gabor analysis and synthesis operations can be implemented by the corresponding DFT analysis and synthesis FBs. The mapping (2.6) can be implemented by a K-channel DFT (analysis) FB with prototype filter impulse response $d[k] = g^*[-k]$ followed by a down-sampling by factor N [35]. The signal synthesis (2.7) can be implemented

	DFT FB	Gabor frame
$g[k] = d^*[-k]$	analysis prototype filter $d[k]$	Gabor atom (or window)$g[k]$
$w[k] = r[k]$	synthesis prototype filter $r[k]$	Gabor atom $w[k]$
N	down/up-sampling factor	time shift
K	number of sub-bands	frequency shift
$v_m[\ell] = X[\ell, m]$	sub-band signal $v_m[\ell]$	Gabor coefficient $X[\ell, m]$

TABLE 2.1: The relation of oversampled DFT FBs and Gabor frames.

by an up-sampling by factor N followed by a K-channel DFT (synthesis) FB with prototype filter impulse response $r[k] = w[k]$. When the two frames $\{g_{\ell,m}[k] : (\ell, m) \in \Lambda\}$ and $\{w_{\ell,m}[k] : (\ell, m) \in \Lambda\}$ represent a dual frame pair, a concatenation of the associated analysis and synthesis FBs provides a PR of the signal, and the construct is thus referred to as a PR FB. Furthermore, tight Gabor frames are related to *paraunitary* DFT FBs. As a consequence of (2.14), paraunitary DFT FBs are special variants of PR FBs where the prototype filters of the analysis and synthesis FBs are related according to $d[k] = r^*[-k]$. Fig. 2.5 shows a paraunitary FB based on a prototype filter with impulse response $d[k]$. Here, the transfer functions of the analysis FBs are given as $D_0(z), \ldots, D_{K-1}(z)$. The

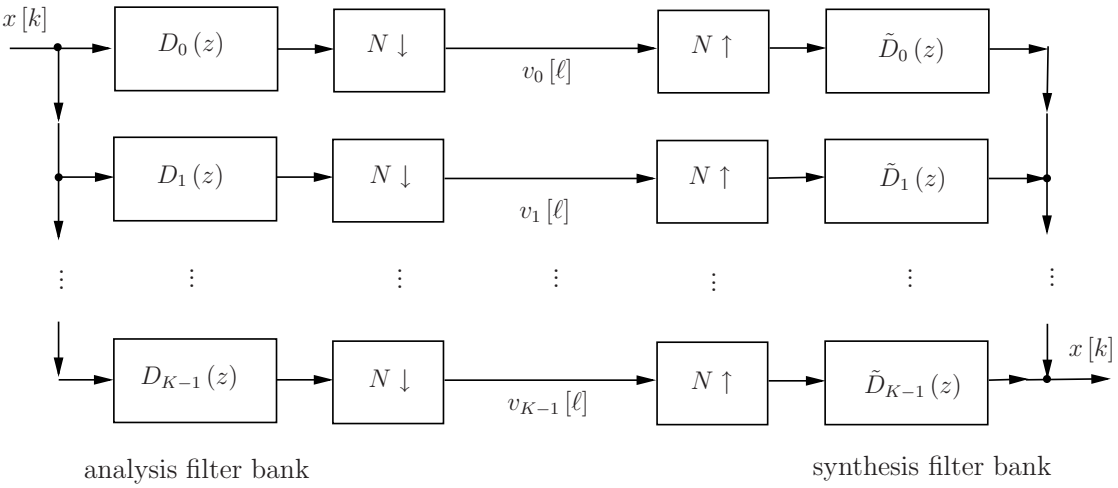

FIGURE 2.5: K-channel paraunitary FB.

transfer functions of the synthesis FBs are the paraconjugates of the transfer functions $D_0(z), \ldots, D_{K-1}(z)$. The paraconjugate $\tilde{D}_m(z)$ of $D_m(z)$ is obtained by conjugating all of the coefficients of the polynomial function $D_m(z)$, and replacing z by z^{-1}, i.e., $\tilde{D}_m(z) = D_m^*(z^{-1})$ [13].

2.3.2 Polyphase Implementation

To discuss the PR condition in the polyphase domain, we first introduce the polyphase representation of oversampled FBs. The polyphase representation [50] is an important concept in multirate signal processing, which leads to efficient implementations of FBs [13].

Let M denote the least common multiple of N and K, and define L and J such that

$$LN = JK = M. \tag{2.25}$$

The M-component polyphase representation of the analysis prototype filter $D(z)$ reads

$$D(z) = \sum_{j=0}^{M-1} z^{-j} D_j\left(z^M\right), \tag{2.26}$$

where

$$D_j(z) = \sum_{k\in\mathbb{Z}} d[j+kM]\, z^{-k} \tag{2.27}$$

is the j-th polyphase component of $D(z)$ with $d[k]$ denoting the impulse response of the analysis prototype filter. The $(j+1)$th element of the $(i+1)$th row of the $K \times N$ polyphase matrix $\mathbf{D}_{\mathrm{P}}(z)$ of the analysis FB is defined as

$$D_{ij}(z) = \sum_{l=0}^{L-1} W_K^{i(j+lN)} z^{-l} D_{j+lN}\left(z^L\right), \tag{2.28}$$

where $W_K = \mathrm{e}^{2\pi\jmath/K}$. Similarly, the $(j+1)$th element of the $(i+1)$th row of the $K \times N$ polyphase matrix $\mathbf{R}_{\mathrm{P}}(z)$ of the synthesis FB is given as

$$R_{ij}(z) = \sum_{l=0}^{L-1} W_K^{i(j+lN)} z^{-l} R_{j+lN}\left(z^L\right), \tag{2.29}$$

where $R_j(z) = \sum_{k\in\mathbb{Z}} r^*[-j-kM]\, z^{-k}$.

Fig. 2.6 shows an equivalent implementation of an oversampled FB. The analysis filters with the following down-sampling by factor N are realized as a delay chain of size N

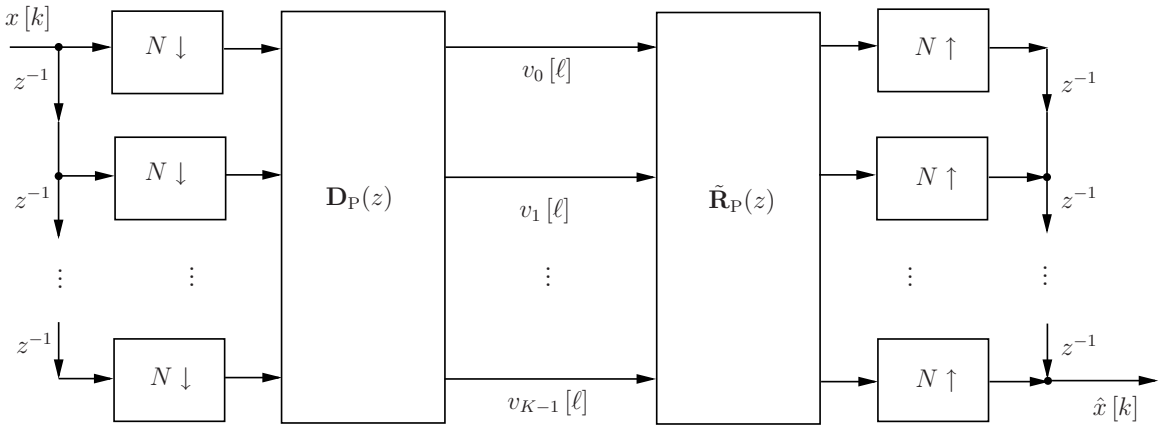

FIGURE 2.6: Oversampled FB using polyphase representation.

followed by the polyphase matrix $\mathbf{D}_{\mathrm{P}}(z)$, while the up-sampling and signal synthesis is realized by the polyphase matrix $\tilde{\mathbf{R}}_{\mathrm{P}}(z)$ followed by an up-sampling and signal adding. The paraconjugate $\tilde{\mathbf{R}}_{\mathrm{P}}(z)$ of the polynomial matrix $\mathbf{R}_{\mathrm{P}}(z)$ is obtained by transposition followed by element-wise paraconjugation.

The input-output relation (2.21) can be expressed in the polyphase domain as $\hat{\mathbf{x}}(z) = \tilde{\mathbf{R}}_{\mathrm{P}}(z)\mathbf{D}_{\mathrm{P}}(z)\mathbf{x}(z)$, where $\mathbf{x}(z) = [X_0(z), \ldots, X_{N-1}(z)]^{\mathrm{T}}$ and $\hat{\mathbf{x}}(z) = [\hat{X}_0(z), \ldots, \hat{X}_{N-1}(z)]^{\mathrm{T}}$ with $X_j(z) = \sum_{k\in\mathbb{Z}} x[-j+kN]z^{-k}$ and $\hat{X}_j(z) = \sum_{k\in\mathbb{Z}} \hat{x}[-j+kN]z^{-k}$. It follows that an oversampled FB satisfies the PR condition with zero delay, i.e, $\hat{x}\,[k] = x\,[k]$, if and only if

$$\tilde{\mathbf{R}}_{\mathrm{P}}(z)\mathbf{D}_{\mathrm{P}}(z) = \mathbf{I}_N, \tag{2.30}$$

where $\mathbf{I}_N$ is the $N \times N$ identity matrix [13].

Furthermore, in case of an oversampled DFT FB the analysis polyphase matrix $\mathbf{D}_{\mathrm{P}}(z)$ can be written as the product of the inverse DFT matrix $\mathbf{F}_K^{\mathrm{H}}$ and a polynomial matrix $\mathbf{B}(z)$, i.e., $\mathbf{D}_{\mathrm{P}}(z) = \mathbf{F}_K^{\mathrm{H}}\mathbf{B}(z)$, with $\mathbf{F}_K$ denoting the DFT matrix of size $K \times K$ (defined as $[\mathbf{F}_K]_{m,n} = \mathrm{e}^{-\jmath 2\pi(m-1)(n-1)/K}$). As can be shown, the polynomial matrix $\mathbf{B}(z)$ is given as

$$\mathbf{B}(z) \triangleq [\mathbf{I}_K \cdots \mathbf{I}_K]\mathrm{Diag}\big[D_0\left(z^L\right), \ldots, D_{M-1}\left(z^L\right)\big] \begin{bmatrix} \mathbf{I}_N \\ z^{-1}\mathbf{I}_N \\ \vdots \\ z^{-(L-1)}\mathbf{I}_N \end{bmatrix}. \tag{2.31}$$

The synthesis polyphase matrix, on the other hand, can be expressed as $\mathbf{R}_{\mathrm{P}}(z) = \mathbf{F}_K^{\mathrm{H}}\mathbf{C}(z)$ with some polynomial matrix $\mathbf{C}(z)$. The resulting implementation is shown in Fig. 2.7. Usually, because of the simple forms of $\mathbf{B}(z)$ and $\mathbf{C}(z)$ as compared to $\mathbf{D}_{\mathrm{P}}(z)$ and $\mathbf{R}_{\mathrm{P}}(z)$

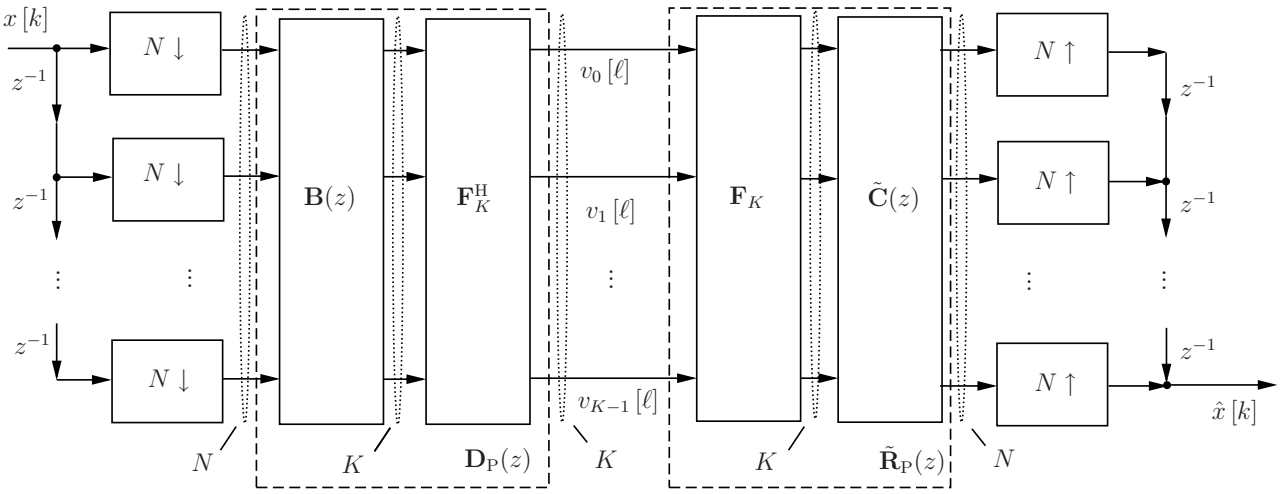

FIGURE 2.7: Oversampled DFT FB using polyphase representation.

and due to the availability of FFT algorithms, the implementation in Fig. 2.7 is computationally more favorable than the implementation in Fig. 2.6.

As follows from (2.22) and (2.24), in the case of a paraunitary FB $d\,[k] = r^*\,[-k]$ and thus $\mathbf{R}_{\mathrm{P}}(z) = \mathbf{D}_{\mathrm{P}}(z)$. Here, due to the PR condition, $\tilde{\mathbf{D}}_{\mathrm{P}}(z)\mathbf{D}_{\mathrm{P}}(z) = \mathbf{I}_N$. It also follows that

$$\tilde{\mathbf{B}}(z)\mathbf{B}(z) = K^{-1}\mathbf{I}_N. \tag{2.32}$$

Fig. 2.8 shows a paraunitary FB implemented based on the polyphase representation.

2.4 Parameterization of Tight Gabor Frames

To enable the computation of optimized paraunitary FBs in Chap. 3, some further elaboration of the PR constraints is needed. In [47], a parameterization of tight Gabor frames on the basis of the polyphase representation was presented. The starting point has been, however, the polyphase representation of the atom $g[k]$ rather than the polyphase representation of the impulse response $d\,[k]$ as employed in Sect. 2.3.1. The jth polyphase

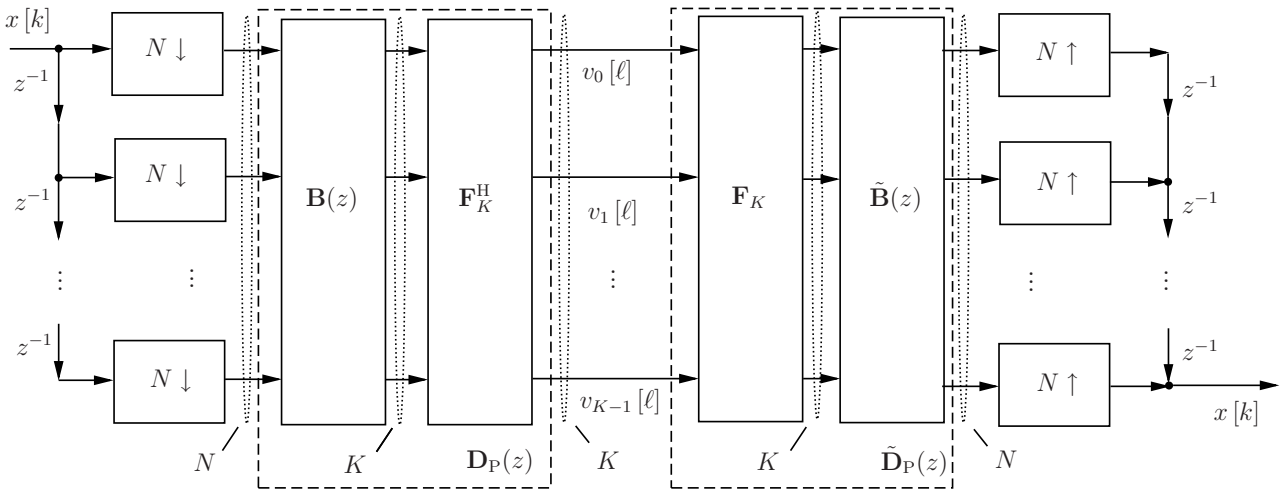

FIGURE 2.8: Paraunitary FB using polyphase representation.

component $G_j(z)$ is given by

$$G_j(z) = \sum_{k\in\mathbb{Z}} g[j+kM]z^{-k}. \tag{2.33}$$

Due to (2.22), $G_j(z) = \tilde{D}_j(z)$. As easily seen, (2.32) is fulfilled iff (i.e., if and only if) $\widetilde{\mathbf{V}}(z)\mathbf{V}(z) = K^{-1}\mathbf{I}_N$, where

$$\mathbf{V}(z) \triangleq [\mathbf{I}_K \cdots \mathbf{I}_K]\mathrm{Diag}\big[G_0\left(z^L\right), \ldots, G_{M-1}\left(z^L\right)\big] \begin{bmatrix} \mathbf{I}_N \\ z^{-1}\mathbf{I}_N \\ \vdots \\ z^{-(L-1)}\mathbf{I}_N \end{bmatrix}. \tag{2.34}$$

Hence, the Gabor system represents a tight frame in $L^2(\mathbb{Z})$ iff $\mathbf{V}(z)$ is paraunitary with $\widetilde{\mathbf{V}}(z)\mathbf{V}(z) = K^{-1}\mathbf{I}_N$. Note that there are L nonzero elements in each column of $\mathbf{V}(z)$ and J nonzero elements in each row, that is,

$$[\mathbf{V}(z)]_{m,n} = 0 \quad \text{if}\big((m-n) \bmod B\big) \neq 0, \tag{2.35}$$

where $B = N/J = K/L$. Consequently, $\mathbf{V}(z)$ is paraunitary iff the B matrices $\mathbf{V}_0(z), \ldots, \mathbf{V}_{B-1}(z)$ of size $L \times J$, which comprise the possibly non-zero elements of $\mathbf{V}(z)$ according to

$$[\mathbf{V}_b(z)]_{m,n} = [\mathbf{V}(z)]_{1+B(m-1)+b,1+B(n-1)+b} \quad b = 0, \ldots, B-1, \tag{2.36}$$

are all paraunitary. As follows from (2.34) the elements of the B matrices are given as

$$[\mathbf{V}_b(z)]_{m,n} = z^{-\lfloor f(m,n)/J \rfloor} G_{Bf(m,n)+b}\left(z^L\right), \quad b = 0, \ldots, B-1 \tag{2.37}$$

with

$$f(m,n) \triangleq \sum_{j=0}^{J-1} \sum_{\ell=0}^{L-1} (m + jL - 1)\delta_{m+jL,n+\ell J} \tag{2.38}$$

and $\delta_{i,j}$ denoting the Kronecker delta.

Example: $K = 8$, $N = 6$

Assume a FB with $K = 8$ sub-bands and a down-sampling factor of $N = 6$. According to (2.34), the polynomial matrix $\mathbf{V}(z)$ is given as

$$\mathbf{V}(z) = \begin{bmatrix} G_0(z^4) & 0 & z^{-1}G_8(z^4) & 0 & z^{-2}G_{16}(z^4) & 0 \\ 0 & G_1(z^4) & 0 & z^{-1}G_9(z^4) & 0 & z^{-2}G_{17}(z^4) \\ z^{-3}G_{18}(z^4) & 0 & G_2(z^4) & 0 & z^{-1}G_{10}(z^4) & 0 \\ 0 & z^{-3}G_{19}(z^4) & 0 & G_3(z^4) & 0 & z^{-1}G_{11}(z^4) \\ z^{-2}G_{12}(z^4) & 0 & z^{-3}G_{20}(z^4) & 0 & G_4(z^4) & 0 \\ 0 & z^{-2}G_{13}(z^4) & 0 & z^{-3}G_{21}(z^4) & 0 & G_5(z^4) \\ z^{-1}G_6(z^4) & 0 & z^{-2}G_{14}(z^4) & 0 & z^{-3}G_{22}(z^4) & 0 \\ 0 & z^{-1}G_7(z^4) & 0 & z^{-2}G_{15}(z^4) & 0 & z^{-3}G_{23}(z^4) \end{bmatrix}.$$

We notice that there are $L = 4$ and $J = 3$ nonzero elements in each column and each row of $\mathbf{V}(z)$, respectively. Furthermore, $\mathbf{V}(z)$ is split into $B = 2$ matrices $\mathbf{V}_0(z)$ and $\mathbf{V}_1(z)$ with dimension 4×3. The matrix $\mathbf{V}_0(z)$ is generated by collecting the nonzero elements in the odd-numbered rows of $\mathbf{V}(z)$, while $\mathbf{V}_1(z)$ comprises the nonzero elements in the even-numbered rows of $\mathbf{V}(z)$. It is obvious that the matrix $\mathbf{V}(z)$ is paraunitary iff

$$\mathbf{V}_0(z) = \begin{bmatrix} G_0(z^4) & z^{-1}G_8(z^4) & z^{-2}G_{16}(z^4) \\ z^{-3}G_{18}(z^4) & G_2(z^4) & z^{-1}G_{10}(z^4) \\ z^{-2}G_{12}(z^4) & z^{-3}G_{20}(z^4) & G_4(z^4) \\ z^{-1}G_6(z^4) & z^{-2}G_{14}(z^4) & z^{-3}G_{22}(z^4) \end{bmatrix}, \tag{2.39}$$

and

$$\mathbf{V}_1(z) = \begin{bmatrix} G_1\left(z^4\right) & z^{-1}G_9\left(z^4\right) & z^{-2}G_{17}\left(z^4\right) \\ z^{-3}G_{19}\left(z^4\right) & G_3\left(z^4\right) & z^{-1}G_{11}\left(z^4\right) \\ z^{-2}G_{13}\left(z^4\right) & z^{-3}G_{21}\left(z^4\right) & G_5\left(z^4\right) \\ z^{-1}G_7\left(z^4\right) & z^{-2}G_{15}\left(z^4\right) & z^{-3}G_{23}\left(z^4\right) \end{bmatrix} \tag{2.40}$$

are both paraunitary. The index matrix $\mathbf{F}_{\text{index}}$, defined such that $[\mathbf{F}_{\text{index}}]_{m,n} = f(m,n)$, equals

$$\mathbf{F}_{\text{index}} = \begin{bmatrix} 0 & 4 & 8 \\ 9 & 1 & 5 \\ 6 & 10 & 2 \\ 3 & 7 & 11 \end{bmatrix} \tag{2.41}$$

in this example.

Note that if the sequence $(\lfloor f(m,n)/J \rfloor)_{m=1,\ldots,L}$ was identical for all column indices $n = 1,\ldots,J$, then the factor $z^{-\lfloor\cdots\rfloor}$ could be omitted in (2.37) without any effect on the condition, i.e.,

$$\widetilde{\mathbf{V}}_b(z)\mathbf{V}_b(z) = K^{-1}\mathbf{I}_J, \quad \forall b \in \{0,\ldots,B-1\}\,. \tag{2.42}$$

Replacing some $G_m\left(z^L\right)$ by the equivalent $z^{-L}G_{M+m}\left(z^L\right)$ is a way to align the sequences. After doing so, we can discard the factors $z^{-\lfloor\cdots\rfloor}$ and additionally replace z^L in the arguments of the elements of $\mathbf{V}_b(z)$ by z. We denote the resulting matrices of size $L \times J$ as $\mathbf{W}_0(z),\ldots,\mathbf{W}_{B-1}(z)$, given by

$$[\mathbf{W}_b(z)]_{m,n} = G_{B\bar{f}(m,n)+b}\left(z\right), \quad b = 0,\ldots,B-1 \tag{2.43}$$

with the index map

$$\bar{f}(m,n) \triangleq \begin{cases} f(m,n) & \text{if } f(m,n) \geq f(1,n) \\ f(m,n) + M/B & \text{if } f(m,n) < f(1,n) \end{cases}. \tag{2.44}$$

Since the polynomial matrices $\mathbf{V}_0(z),\ldots,\ \mathbf{V}_{B-1}(z)$ are paraunitary iff the matrices $\mathbf{W}_0(z),\ldots,\mathbf{W}_{B-1}(z)$ are paraunitary, the Gabor system (2.1) represents a tight frame in $L^2(\mathbb{Z})$ iff

$$\widetilde{\mathbf{W}}_b(z)\mathbf{W}_b(z) = K^{-1}\mathbf{I}_J \quad \forall b \in \{0,\ldots,B-1\}\,. \tag{2.45}$$

We note that the size of each polynomial matrix $\mathbf{W}_b(z)$, their number B, and the index map $\bar{f}(m,n)$ are fully determined by N and K. Given these two constants, any tight Gabor frame is uniquely defined by an instance of $\mathbf{W}_0(z),\ldots,\mathbf{W}_{B-1}(z)$ satisfying (2.45). Clearly, the degree of freedom in choosing any $\mathbf{W}_b(z)$ subject to (2.45) increases with the oversampling ratio K/N. The length of the window $g\,[k]$ is related to the polynomial orders of the matrices $\mathbf{W}_0(z),\ldots,\mathbf{W}_{B-1}(z)$. We define P as the maximal polynomial order of the B matrices plus 1. In the case $P=1$, all elements of the matrices are scalars. Hence, the support of the representable functions $g[k]$ is limited to $\{B\bar{f}(m,n)+b\ :\ m=1,\ldots,L; n=1,\ldots,J; b=0,\ldots,B-1\}$. This set is usually not of the form $\mathbb{Z}\cap[a_0,b_0]$ for some $a_0\leq b_0$ but exhibits "gaps". By increasing P longer windows can be found as will be shown in the example below.

As a consequence of (2.43) and (2.33), the matrices $\mathbf{W}_0(z),\ldots,\mathbf{W}_{B-1}(z)$ and the samples of $g\,[k]$ are related through

$$[\mathbf{W}_b(z)]_{m,n}=\sum_{p=0}^{P-1} g\left[B\bar{f}(m,n)+b+Mp\right]z^{-p},\quad b=0,\ldots,B-1. \tag{2.46}$$

The polynomial matrices $\mathbf{W}_b(z)$ can also be written in the form of a matrix polynomial, i.e.,

$$\mathbf{W}_b(z)=\mathbf{W}_{b,0}+z^{-1}\mathbf{W}_{b,1}+\cdots z^{-(P-1)}\mathbf{W}_{b,P-1},\quad b=0,\ldots,B-1. \tag{2.47}$$

Here, $\mathbf{W}_{b,0},\ldots,\mathbf{W}_{b,P-1}$ are matrices with scalar elements, which correspond to the samples of the window $g\,[k]$.

Returning to the above example, the index matrix $\bar{\mathbf{F}}_{\text{index}}$ relating to the index map $\bar{f}(m,n)$, resulting from (2.44), reads

$$\bar{\mathbf{F}}_{\text{index}}=\begin{bmatrix}0 & 4 & 8\\ 9 & 13 & 17\\ 6 & 10 & 14\\ 3 & 7 & 11\end{bmatrix}. \tag{2.48}$$

Furthermore, the matrices (2.43) are given as

$$\mathbf{W}_0(z) = \begin{bmatrix} G_0(z) & G_8(z) & G_{16}(z) \\ G_{18}(z) & G_{26}(z) & G_{34}(z) \\ G_{12}(z) & G_{20}(z) & G_{28}(z) \\ G_6(z) & G_{14}(z) & G_{22}(z) \end{bmatrix}, \tag{2.49}$$

and

$$\mathbf{W}_1(z) = \begin{bmatrix} G_1(z) & G_9(z) & G_{17}(z) \\ G_{19}(z) & G_{27}(z) & G_{35}(z) \\ G_{13}(z) & G_{21}(z) & G_{29}(z) \\ G_7(z) & G_{15}(z) & G_{23}(z) \end{bmatrix}. \tag{2.50}$$

When $P = 1$, the matrices $\mathbf{W}_b(z)$ comprise scalars, i.e.,

$$\mathbf{W}_0(z) = \mathbf{W}_{0,0} = \begin{bmatrix} g[0] & g[8] & g[16] \\ g[18] & g[26] & g[34] \\ g[12] & g[20] & g[28] \\ g[6] & g[14] & g[22] \end{bmatrix} \tag{2.51}$$

and

$$\mathbf{W}_1(z) = \mathbf{W}_{1,0} = \begin{bmatrix} g[1] & g[9] & g[17] \\ g[19] & g[27] & g[35] \\ g[13] & g[21] & g[29] \\ g[7] & g[15] & g[23] \end{bmatrix}, \tag{2.52}$$

and the length T of the support of $g[k]$ is $T = M = LJB$.

When $P = 2$, $\mathbf{W}_0(z)$ and $\mathbf{W}_1(z)$ are polynomial matrices with maximal polynomial order 1, which can be written as

$$\mathbf{W}_0(z) = \underbrace{\begin{bmatrix} g[0] & g[8] & g[16] \\ g[18] & g[26] & g[34] \\ g[12] & g[20] & g[28] \\ g[6] & g[14] & g[22] \end{bmatrix}}_{\mathbf{W}_{0,0}} + z^{-1} \underbrace{\begin{bmatrix} g[24] & g[32] & g[40] \\ g[42] & g[50] & g[58] \\ g[36] & g[44] & g[52] \\ g[30] & g[38] & g[46] \end{bmatrix}}_{\mathbf{W}_{0,1}} \tag{2.53}$$

and

$$\mathbf{W}_1(z) = \underbrace{\begin{bmatrix} g[1] & g[9] & g[17] \\ g[19] & g[27] & g[35] \\ g[13] & g[21] & g[29] \\ g[7] & g[15] & g[23] \end{bmatrix}}_{\mathbf{W}_{1,0}} + z^{-1} \underbrace{\begin{bmatrix} g[25] & g[33] & g[41] \\ g[43] & g[51] & g[59] \\ g[37] & g[45] & g[53] \\ g[31] & g[39] & g[47] \end{bmatrix}}_{\mathbf{W}_{1,1}}. \tag{2.54}$$

The support of the window $g[k]$ now includes twice the number of samples than in the case $P = 1$, i.e., $T = 2M$. Note that an element of $\mathbf{W}_{0,0}$ or $\mathbf{W}_{1,0}$ and the corresponding element of $\mathbf{W}_{0,1}$ or $\mathbf{W}_{1,1}$ represent two samples of $g[k]$ separated by M samples. In general, the support of the window includes $T = PM = PLJB$ samples. Thus with fixed N and K, it is possible to have an arbitrarily long window by choosing an appropriate polynomial order. As shown in Fig. 2.9 for $P = 1$ and $P = 2$, there are some 'gaps' in

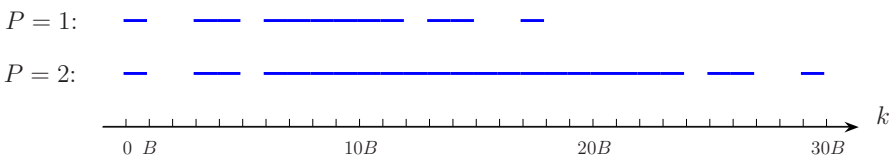

FIGURE 2.9: Support of the window functions $g[k]$ relating to matrices $\mathbf{W}_0(z), \ldots, \mathbf{W}_{B-1}(z)$ with maximal polynomial order $P-1$ for $L = 4$, $J = 3$, $P = 1, 2$.

the support of the representable functions $g[k]$.

For the window optimization in Sect. 3.6.1 and Sect. 3.6.2, it is helpful to introduce a window function $r[k]$ which contains the samples of $g[k]$ in a permuted order. Let us define $(r[0], \ldots, r[T-1])$ as

$$r[k] = g[B\bar{f}(m,n) + b + Mp], \quad k = 0, \ldots, T-1 \tag{2.55}$$

with $m = (k \bmod L) + 1$, $n = \lfloor (k \bmod LJ)/L \rfloor + 1$, $p = \lfloor (k \bmod LJP)/(LJ) \rfloor$, and $b = \lfloor k/(LJP) \rfloor$. As follows from (2.46) and (2.55), the matrices $\mathbf{W}_0(z), \ldots, \mathbf{W}_{B-1}(z)$ are now related to the permuted window $r[k]$ through

$$[\mathbf{W}_b(z)]_{m,n} = \sum_{p=0}^{P-1} r[L(J(bP+p)+n-1)+m-1] z^{-p}. \tag{2.56}$$

The result can easily been seen in the above example. For $P = 1$, the window $r[k]$ can be generated by reading the elements of first the matrix $\mathbf{W}_{0,0}$ and then the matrix $\mathbf{W}_{1,0}$ column-wise. For $P = 2$, $r[k]$ is obtained in a similar way by reading from the four matrices $\mathbf{W}_{0,0}$, $\mathbf{W}_{0,1}$, $\mathbf{W}_{1,0}$ and $\mathbf{W}_{1,1}$.

With the above discussed parameterization of tight Gabor frames, the tight frame condition is formulated by constraining B polynomial matrices to be paraunitary. As shown in this section, the samples of the window function are directly related to the entries of these polynomial matrices, and windows with any lengths can be handled by an appropriate polynomial order. The discussed theory will be used for the window optimization in Chap. 3.

Chapter 3

Efficient Time-Frequency Channel Representation

3.1 Introduction

In the previous chapter the TF signal representation via Gabor frames and the related FB implementation have been introduced. In addition to an appropriate signal representation, reconfigurable receivers can be derived based on a suitable format for the description of wireless channels.

For dealing with signal dispersion caused by the channel fundamentally different methods are employed for different signal formats. In systems using OFDM transmission, the multipath channel can be represented equivalently in the form of parallel single-tap channels. These taps can be arranged to form a diagonal matrix which multiplies a transmitted signal vector provided in the frequency domain by a block-wise DFT. This channel *diagonalization* enables straightforward demodulation and coefficient estimation schemes.

The concept of channel diagonalization of OFDM receivers is limited to time-invariant channels. However, by resorting to TF signal representations discussed in Chap. 2, these limitations can be overcome. We discuss a channel diagonalization in the TF domain for a channel which can be modelled as WSSUS. In this channel representation, the signal

mapping by the channel is efficiently formulated as an element-wise multiplication of each coefficient of the TF signal representation by the channel gain at the respective TF location [51]. This concept for parameterizing linear channels can be seen as a generalization of the channel diagonalization known from OFDM for arbitrary signals without cyclic extensions. Moreover, the channel diagonalization can be adapted to different channel conditions by choosing the underlying Gabor window function and the oversampling ratio.

Even though the TF domain channel diagonalization is approximative in the general case of doubly dispersive channels, for typical underspread channels encountered in mobile radio scenarios the inherent model error can be limited to a usually acceptable level by choosing an adequate window underlying the signal analysis. A major concern of this chapter is to define optimized TF signal representations for channels with known statistical properties.

In Sect. 3.2 the WSSUS channel model is discussed for the time-discrete case. A TF domain channel diagonalization is presented in Sect. 3.3, which is suitable to be combined with Gabor multipliers to be introduced in Sect. 3.4. The inherent error introduced by the channel diagonalization is analyzed both in the time domain and the TF domain in Sect. 3.5. To minimize the mean-squared sample error, the window design problem is formulated as a convex optimization problem in Sect. 3.6, and numerical results are presented in Sect. 3.7.

3.2 Representation of WSSUS Channels

The radio channels typically encountered in wireless communications are subject to time-variance and multipath propagation. In [52], Bello proposed a statistical characterization of randomly time-variant linear channels in terms of correlation functions and system functions. In order to describe the input-output behavior of a time-variant time-continuous channel in the time domain, the *time-variant impulse response* $c\,(t, \tau)$ is often employed with t denoting the time dimension and τ the delay dimension. All subsequent signal representations are to be interpreted in the complex baseband. Given the time-continuous channel input signal $x\,(t)$, the noise-free signal at the channel output can be

written as

$$y(t) = \int_{-\infty}^{\infty} x(t-\tau)\, c(t,\tau)\, \mathrm{d}\tau. \tag{3.1}$$

The TF selectivity of the channel is reflected by the *time-variant transfer function* $C(t,f)$, which is obtained by the Fourier transform of $c(t,\tau)$ with respect to τ, i.e.,

$$C(t,f) = \int_{-\infty}^{\infty} c(t,\tau) \exp(-\jmath 2\pi f\tau)\, \mathrm{d}\tau. \tag{3.2}$$

The time-variant impulse response and the time-variant transfer function are two of Bello's so-called *system functions*. The others are the *delay Doppler spread function* and the *Doppler-variant transfer function*. The delay Doppler spread function is the Fourier transformation of the time-variant impulse response with respect to t, which describes the spreading of the input signal in delay and Doppler dimensions, and a Fourier transform of the delay Doppler spread function with respect to τ results in the Doppler-variant transfer function. A detailed description of the relation between the four system functions can be found in [52, 53].

For random channels, the system functions represent stochastic processes of two independent variables and will be termed *two-dimensional* for short[1]. A widely used statistical model for time-variant wireless channels is the WSSUS model introduced in [52]. According to the WSSUS model, the time-variant impulse response $c(t,\tau)$ represents a stochastic process being wide-sense stationary (WSS) in the time dimension and uncorrelated scattering (US) in the delay dimension. Here, WSS means that $E[c(t,\tau)\, c^*(t',\tau')]$ depends on the time difference $t_\Delta = t - t'$ rather than on the absolute times t and t'. As a consequence, the time-variant transfer function $C(t,f)$ is a two-dimensional WSS stochastic process with autocorrelation function

$$E[C(t,f)\, C^*(t',f')] = R(t-t', f-f') = R(t_\Delta, f_\Delta). \tag{3.3}$$

The so-called *coherence time* T_{coh} is the time interval over which the channel gain is

[1] A stochastic process depending on more than one independent variable is sometimes called *random field*.

strongly correlated[2]. Furthermore, two narrow-band signals undergo correlated attenuations by the channel if their frequency separation is less than the *coherence bandwidth* B_{coh}. A signal with bandwidth larger than B_{coh} is subject to frequency selective fading. Let $R_f(f_\Delta)$ denote the autocorrelation function in frequency with $t_\Delta = 0$, i.e., $R_f(f_\Delta) = R(0, f_\Delta)$. The coherence bandwidth is obtained from $R_f(f_\Delta)$, while the coherence time is obtained from the time correlation function of the channel $R_t(t_\Delta) = R(t_\Delta, 0)$. Moreover, the second-order statistics of the multipath behavior of $c(t, \tau)$ are characterized by $R_f(f_\Delta)$, or, equivalently, by the delay power spectrum

$$S_{\text{delay}}(\tau) = \int_{-\infty}^{\infty} R_f(f_\Delta) \exp(\jmath 2\pi\tau f_\Delta) \, \mathrm{d}f_\Delta. \tag{3.4}$$

The delay power spectrum describes the average received power as a function of the delay τ. In order to characterize the time variation of the channel, the related Doppler power spectrum $S_{\text{Doppler}}(\lambda)$ is defined as

$$S_{\text{Doppler}}(\lambda) = \int_{-\infty}^{\infty} R_t(t_\Delta) \exp(-\jmath 2\pi\lambda t_\Delta) \, \mathrm{d}t_\Delta, \tag{3.5}$$

where λ is the Doppler frequency variable. The Doppler power spectrum shows the average power distribution of the channel output as a function of the Doppler frequency.

For characterizing the delay dispersion of a multipath channel, a widely used parameter is the root mean squared (RMS) *delay spread* τ_{RMS} [54], which is defined as

$$\tau_{\text{RMS}} = \sqrt{\frac{\int_{-\infty}^{\infty} \tau^2 S_{\text{delay}}(\tau) \, \mathrm{d}\tau}{\int_{-\infty}^{\infty} S_{\text{delay}}(\tau) \, \mathrm{d}\tau} - \left(\frac{\int_{-\infty}^{\infty} \tau S_{\text{delay}}(\tau) \, \mathrm{d}\tau}{\int_{-\infty}^{\infty} S_{\text{delay}}(\tau) \, \mathrm{d}\tau} \right)^2}, \tag{3.6}$$

where the normalized delay power spectrum $S_{\text{delay}}(\tau) / \int_{-\infty}^{\infty} S_{\text{delay}}(\tau) \mathrm{d}\tau$ represents a probability density function in τ. In analogy to (3.6), the RMS *Doppler spread* ν_{RMS} is defined as the square root of the second central moment of the Doppler frequency based on the normalized Doppler power spectrum $S_{\text{Doppler}}(\lambda) / \int_{-\infty}^{\infty} S_{\text{Doppler}}(\lambda) \mathrm{d}\lambda$. The coherence time of a wireless channel is inversely proportional to the Doppler spread of the channel, and the coherence bandwidth is inversely proportional to the delay spread.

[2]When the symbol duration is much shorter than T_{coh}, the channel is viewed as slowly time-variant [53].

The dispersion of the channel is characterized by the *scattering function* $S(\tau, \lambda)$, which is obtained from $R(t_\Delta, f_\Delta)$ through a two-dimensional Fourier transform, i.e.,

$$S(\tau, \lambda) = \int_{-\infty}^{\infty} \int_{-\infty}^{\infty} R(t_\Delta, f_\Delta) \exp(-\jmath 2\pi \lambda t_\Delta) \exp(\jmath 2\pi \tau f_\Delta) \, \mathrm{d}t_\Delta \mathrm{d}f_\Delta. \tag{3.7}$$

The scattering function can be considered a power spectrum as a function of the delay and Doppler shift.

For typical underspread channels encountered in wireless systems, $S(\tau, \lambda)$ has a compact support in (τ, λ). Assume the scattering function has a support of rectangular shape, i.e.,

$$S(\tau, \lambda) = 0 \quad \text{for} (\tau, \lambda) \notin [-\tau_0, \tau_0] \times [-\lambda_0, \lambda_0]. \tag{3.8}$$

If $4\tau_0\lambda_0 \leq 1$, the channel is said to be underspread [55, 56]. In fact, most wireless channels are highly underspread, with $\tau_0\lambda_0 \ll 1$. In this case, the channel gain varies slowly over both time and frequency.

While the aforementioned time-continuous stochastic model of $C(t, f)$ can be used to describe the propagation channel, the radio channel including the front-ends of digital transceivers and sampling units without amplifier noise, is usually described by a time-discrete stochastic model. The characterization of a time-continuous stochastic process can be carried over to a time-discrete stochastic process by a uniform sampling. The sampling theorem [57] allows a time-discrete modeling of a linear time-variant system if the system input is band-limited. In this case, the time-variant convolution relating the time-continuous input and output signals in (3.1) with each other carries over to a time-discrete time-variant convolution of the sampled input with a sampled version of the time-variant impulse response to provide the sampled output signal. Both time-continuous input and output signals reconstructed from the samples can be shown to equal the original time-continuous stochastic process in the mean-square sense. Hence, given the time-discrete input signal $x[k]$, the output of a time-variant channel is expressed as

$$y[k] = (\mathcal{H}x)[k] = \sum_{q=0}^{\infty} c[k, q] \, x[k - q], \tag{3.9}$$

where $\mathcal{H}$ is used in the following as a compact notation to represent the channel operator for both deterministic and random channels, i.e. the time-variant convolution in (3.9). Furthermore, the time-discrete time-variant channel impulse response

$$c\,[k,q] = c(kT_\mathrm{s}, q\Theta)$$

is obtained from $c\,(t,\tau)$ by uniformly sampling the latter with a time interval T_s and delay interval Θ. Fig. 3.1 shows a time-continuous linear time-variant system and a corresponding linear time-discrete time-variant system. The time-continuous input and

FIGURE 3.1: Time-continuous and time-discrete systems being equivalent for a band-limited input $x(t)$.

output signals $x(t)$ and $y(t)$ can be reconstructed from the time-discrete input and output signals $x[k]$ and $y[k]$, resp., for the assumed band limitation of $x(t)$ and in this case, the both systems are considered equivalent.

In [58], a time-discrete model for WSSUS channels is discussed which includes the pulse shaping and sampling. Moreover, for a slowly time-variant channel, where the Doppler spreads are small with respect to the system bandwidth, the WSS and US properties are preserved in the time-discrete domain and an equivalent WSSUS time-discrete model is discussed in [59] including a transmit filter, the linear time-variant channel and a receive filter.

We consider time-discrete random channels where the time-variant impulse response $c\,[k,q]$ represents a two-dimensional zero-mean random process complying with the WSSUS model. The autocorrelation function of $c\,[k,q]$ representing the second-order statistics of the channel is determined by the time correlation function $\phi_\mathrm{t}\,[k_\Delta]$ and the delay power spectrum $S_\mathrm{delay}\,[q]$ according to

$$E\left[c\,[k,q]\,c^*\,[k',q']\right] = \phi_\mathrm{t}\,[k_\Delta]\,S_\mathrm{delay}\,[q]\,\delta_{q,q'}. \tag{3.10}$$

The argument $k_\Delta = k - k'$ of the time correlation function reflects wide-sense stationarity in the time dimension, while $\delta_{q,q'}$ implies uncorrelated scattering in the delay dimension. In analogy to (3.4) the time-discrete delay power spectrum is related to the frequency correlation function $\phi_\mathrm{f}[\omega_\Delta]$ through

$$\phi_\mathrm{f}[\omega_\Delta] = \sum_{q=0}^{\infty} S_\mathrm{delay}[q] \exp(-\jmath\omega_\Delta q), \tag{3.11}$$

where ω_Δ represents the difference in frequency.

Of interest in the context of TF signal processing is the time-variant transfer function

$$C(k,\omega) = \sum_{q=0}^{\infty} c[k,q] \exp(-\jmath\omega q), \tag{3.12}$$

which shows explicitly the TF selectivity of a channel realization as a function of k and ω. Sampling of $C(k,\omega)$ in both the time and frequency dimensions results in a TF representation of the channel.

3.3 Channel Diagonalization

In a digital signal processor a time-variant random channel can be represented by a sampled version of the time-variant transfer function $C(k,\omega)$ defined by

$$H[\ell,m] = C(\ell N, 2\pi m/K), \quad (\ell,m) \in \Lambda, \tag{3.13}$$

where $H[\ell,m]$ is called the *channel coefficient* in the following. For compatibility with the TF signal representations introduced in Sect. 2.2, the sampling intervals N and $2\pi/K$ are chosen in line with those for the Gabor system (2.1), where N and $2\pi/K$ denote the time and frequency shifts, resp., of the Gabor elementary functions in the TF plane. Note that N represents an integer sampling interval, while $2\pi/K$ is a positive real-valued sampling interval in the frequency domain.

The time-variant transfer function represents the complex-valued channel gain over time and frequency. The time-discrete channel coefficient $H[\ell, m]$ is defined in (3.13) as the channel gain at the time ℓN and the frequency $2\pi m/K$. Hence, given the TF representation $X = \mathcal{G}x$ of a signal $x[k]$ at the channel input, it is straightforward to approximate the signal $y[k]$ at the channel output by the function

$$\hat{y} = \mathcal{G}^* (H \odot X) \tag{3.14}$$

$$= \sum_{(\ell,m)\in\Lambda} H[\ell, m] \langle x, g_{\ell,m} \rangle g_{\ell,m}, \tag{3.15}$$

where $\odot$ represents the element-wise multiplication of two functions $H = H[\ell, m]$ and $X = X[\ell, m]$ defined on a two-dimensional index set $(\ell, m) \in \Lambda$, i.e., $(H \odot X)[\ell, m] = H[\ell, m]X[\ell, m]$. The expression $\mathcal{G}^* (H \odot X)$, namely the concatenation of an analysis operator, an element-wise multiplication and a synthesis operator, is known in the mathematical literature as *Gabor multiplier* [60]. Here, we use a Gabor multiplier to approximate $y[k]$ by $\hat{y}[k]$. A detailed description of Gabor multipliers can be found in the next section.

Fig. 3.2 shows an implementation of (3.14) by paraunitary FBs discussed in Sect. 2.3.1, where $G_m(z) \triangleq G(z \exp(\jmath 2\pi m/K))$ and $\tilde{G}_m(z) = G_m^*(z^{-1})$, $m = 0, \ldots, K-1$, with $G(z)$ denoting the transfer function of the synthesis prototype filter, which is the z-transform of $g[k]$. The TF coefficients $X[\ell, m]$ with $(\ell, m) \in \Lambda$ of the signal $x[k]$ are obtained from

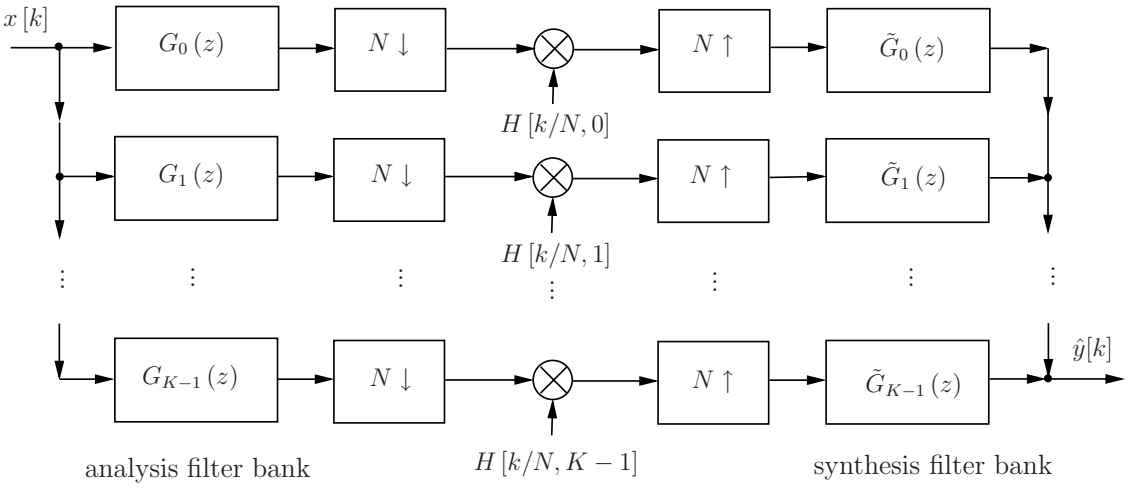

FIGURE 3.2: TF domain channel diagonalization using FB implementation.

an analysis FB using $\tilde{G}_m(z)$. After a down-sampling of the analysis FB output signals by a factor N, the resulting signals in the mth sub-band are weighted element-wise by the channel coefficients $H[\ell, m]$. After up-sampling by factor N, the sub-band signals are transformed back to the time domain via the synthesis FB.

Due to the sampling of the time-variant transfer function $C(k, \omega)$ of the channel, the model (3.14) usually only approximates the mapping of the linear operator in (3.9). As a consequence, the output signal $\hat{y}[k]$ of the synthesis FB is an approximation of the channel output signal $y[k]$. The accuracy of $\hat{y}[k]$ depends on the channel characteristics and the underlying Gabor frame. We may expect the model error to be small if the support of every element $g_{\ell,m}[k]$ of the Gabor frame is highly concentrated around $(\ell N, 2\pi m/K)$ in the TF plane such that $C(k, \omega)$ is essentially constant within the support of $g_{\ell,m}[k]$. TF well-localized window functions fulfilling this condition can be designed for underspread channels typically encountered in mobile radio scenarios via convex optimization, which will be shown in Sect. 3.6.

The TF channel diagonalization offers several advantages. First of all, the sampling intervals N and $2\pi/K$ can be chosen such that they conform with the channel coherence time and frequency, resp., thereby treating time and frequency dispersion by an underspread channel as symmetrical effects. In case of a multipath channel with a small coherence frequency or, equivalently, a large delay spread, the frequency shift shall be chosen accordingly small. In this way, the channel diagonalization can be adapted to channels with different delay and Doppler spreads. Secondly, the formulation of the signal mapping by the channel as the element-wise product (3.14) facilitates scalable and efficient receiver processing known from OFDM, where a "single-tap" frequency domain equalizer is employed. Last but not least, the proposed channel description is independent of the particular signal types, e.g. single-carrier, multi-carrier or spread-spectrum signals, which makes it suitable for reconfigurable receivers to be used for handling signals from different air interfaces. The channel diagonalization also enables an efficient channel parameter estimation scheme [61] and a simple demodulation approach for reconfigurable receivers.

3.4 Gabor Multipliers

To introduce the definition of Gabor multipliers [62], we use the same notations as in Chap. 2, i.e., a Gabor atom is denoted as $g[k]$, a corresponding dual atom is denoted as $w[k]$ and $\Lambda = \mathbb{Z} \times \{0, \ldots, K-1\}$ is a TF-lattice. Furthermore, let $f[k]$ be a time-discrete function in $L^2(\mathbb{Z})$, and $M[\ell, m]$ a time-discrete function in $L^2(\Lambda)$. The Gabor multiplier associated with (g, w, Λ, M) is defined by

$$G_{g,w,\Lambda,M}(f) = \sum_{(\ell,m)\in\Lambda} M[\ell, m] \langle f, g_{\ell,m} \rangle w_{\ell,m}. \tag{3.16}$$

As a consequence, the signal representation of $f[k]$ using normalized tight Gabor frames $\{g_{\ell,m}[k] : (\ell, m) \in \Lambda\}$, i.e. $f = \sum_{(\ell,m)\in\Lambda} \langle f, g_{\ell,m} \rangle g_{\ell,m}$, can be viewed as

$$G_{g,g,\Lambda,1}(f) = f. \tag{3.17}$$

Thus, $G_{g,g,\Lambda,1}$ represents an identity operator, and in this case $g[k] = w[k]$ and $M[\ell, m] = 1$.

The channel diagonalization discussed in Sect. 3.3 has the form of $G_{g,g,\Lambda,H}(x)$ where $H[\ell, m]$ represents the channel coefficient. Given the input signal $x[k]$, approximating the output of a time-variant channel using the form of $\mathcal{G}^*\Big(H \odot \mathcal{G}x\Big)$ can be viewed as a generalization of the representation of the channel output signal used in OFDM systems. In the latter case, given the channel input signal $x[k]$ and the channel gain $h[m], m = 0, \ldots, K-1$, at each frequency sub-band m, the output signal of a time-invariant channel outside the cyclic prefix within a symbol period is represented as $\mathcal{F}^{-1}(h \odot \mathcal{F}x)$, namely the concatenation of a time-discrete Fourier transform $\mathcal{F}$, an element-wise multiplication and an inverse time-discrete Fourier transform $\mathcal{F}^{-1}$.

The properties of the Gabor multiplier depend on the TF concentration properties of the Gabor atom and the lattice constants [62]. Hence, the performance of the Gabor multiplier for approximating the channel output signal $y[k]$ depends on $g[k]$, N and K. In [51], $M[\ell, m]$ is analytically derived for approximating the output signal of a deterministic channel where the objective is to minimize the Euclidean distance between the

approximated signal vector $\hat{\mathbf{y}}$ and the output signal vector $\mathbf{y}$ using the Gabor multiplier. In the following section we are interested in using the Gabor multiplier to approximate the output of a random channel with minimal error for given second order channel statistics. The approximation error will be discussed in the mean-square sense in both time and TF domains.

3.5 Mean-Squared Error Analysis

The TF diagonalization of a time-variant random channel proposed in Sect. 3.3 introduces a certain error, and the error depends on the chosen Gabor frame and the corresponding channel characteristics. In this section, we will discuss the error in the mean-squared sense assuming the random channel is WSSUS. To remain general with respect to signal and channel properties, we consider the error signals both in time and TF domains under the assumptions of

- a white random signal at the channel input,
- a random channel $\mathcal{H}$ complying with the WSSUS model and unit average channel gain (i.e., $\phi_{\mathrm{f}}[0]=\phi_{\mathrm{t}}[0]=1$).

To formulate the MSE, we introduce the aforementioned white random channel input signal $x_Q[k]$ being subject to $E[x_Q[k]]=0$ and

$$E\left[x_Q^*[k]x_Q[k']\right]=\begin{cases}\delta_{k,k'} & \text{for } k,k'\in\left[-\frac{Q}{2},\frac{Q}{2}\right]\\ 0 & \text{otherwise}\end{cases} \tag{3.18}$$

with Q an even positive integer.

3.5.1 Mean-Squared Error in the TF Domain

We first consider the formulation of the MSE in the TF domain. Fig. 3.3 shows the set-up for computing the TF domain channel diagonalization error. Given a random

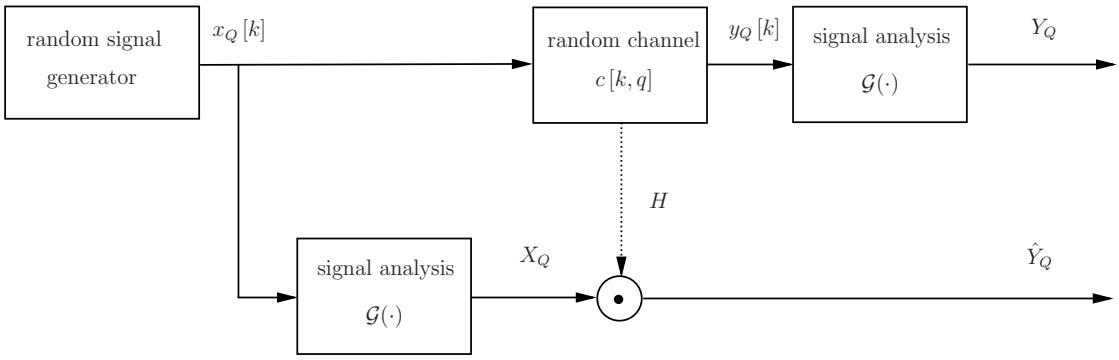

FIGURE 3.3: Set-up for calculating the TF domain channel diagonalization error.

input signal $x_Q[k]$, the TF representation $Y_Q = \mathcal{G}y_Q$ of the actual channel output signal $y_Q[k] = \sum_{q=0}^{\infty} c[k,q]\, x_Q[k-q]$ appears at the right hand side of the upper chain. In the lower chain, the TF representation X_Q of the input signal $x_Q[k]$ is obtained by a signal analysis operator $\mathcal{G}$, i.e. $X_Q = \mathcal{G}x_Q$. Then X_Q is element-wise multiplied by the channel coefficient H, and the resulting $\hat{Y}_Q$ is the approximated channel output signal in the TF domain.

We formulate the TF domain error E_Q introduced by the channel diagonalization (3.14) as the difference between $\hat{Y}_Q \in L^2(\Lambda)$ and $Y_Q \in L^2(\Lambda)$, i.e.,

$$E_Q = \hat{Y}_Q - Y_Q. \tag{3.19}$$

Since the channel is assumed to be WSS in both time and frequency dimensions, the MSE of the channel diagonalization is independent of $(\ell, m) \in \Lambda$. Hence, the MSE ϵ_{TF} per TF coefficient can be expressed as a function of the prototype $g \in L^2(\mathbb{Z})$, i.e.,

$$\begin{aligned} \epsilon_{\mathrm{TF}}(g) &= \lim_{Q\to\infty} E\left[\frac{1}{\frac{Q}{N}\cdot K}\sum_{(\ell,m)\in\Lambda_Q} |E_Q[\ell,m]|^2\right] \\ &= \frac{N}{K}\lim_{Q\to\infty}\frac{1}{Q}E\left[\sum_{(\ell,m)\in\Lambda_Q} |H[\ell,m]\langle x_Q, g_{\ell,m}\rangle - \langle \mathcal{H}x_Q, g_{\ell,m}\rangle|^2\right], \end{aligned} \tag{3.20}$$

with $\Lambda_Q = \left\{-\left\lfloor\frac{Q}{2N}\right\rfloor, \ldots, \left\lfloor\frac{Q}{2N}\right\rfloor\right\} \times \{0, \ldots, K-1\}$.

It follows that the TF domain MSE introduced by the channel diagonalization can be expressed as

$$\epsilon_{\mathrm{TF}}(g) = 2\left(\|g\|^2 - \Re\left[\langle (g * S_{\mathrm{delay}}) \odot \phi_{\mathrm{t}}, g\rangle\right]\right), \tag{3.21}$$

where a detailed derivation of (3.21) from (3.20) is provided in Appendix A. We notice that $\epsilon_{\mathrm{TF}}(g)$ depends on the shape of the window $g[k]$ and the second-order channel statistics. The first term in the brackets of the MSE (3.21) is the energy $E_g = \|g\|^2$ of $g[k]$, and the second term can be viewed as a linear operation on $g[k]$. The convolution of the delay power spectrum S_{delay} with the window g in the time domain is equivalent to the multiplication of the frequency correlation function $\phi_{\mathrm{f}}[\omega]$, i.e., the Fourier transform of the delay power spectrum according to (3.11), with $\mathcal{F}g = \sum_{k=0}^{\infty} g[k] \exp(-\jmath\omega k)$ in the frequency domain. The resulting time domain signal $\mathcal{F}^{-1}(\phi_{\mathrm{f}} \cdot \mathcal{F}g)$ is then element-wise multiplied by the time correlation function ϕ_{t}. For the extreme case when $\phi_{\mathrm{f}}[\omega] = 1$ and $\phi_{\mathrm{t}}[k] = 1$, i.e., the channel is flat fading, the MSE $\epsilon_{\mathrm{TF}}(g) = 0$. If both the time and frequency correlation functions of the channel are constant in the support of the atom $g[k]$ in the TF plane, the error is minimized. Hence, when the support of the atom is highly concentrated in both time and frequency, i.e., it is localized in a relatively small area in the TF plane, the channel can be viewed as approximately flat in that area. As a consequence, the MSE $\epsilon_{\mathrm{TF}}(g)$ approaches zero.

To search for optimized window functions minimizing $\epsilon_{\mathrm{TF}}(g)$ for different channel characteristics, (3.21) is used as a cost function. The window optimization can be solved using SDP methods, which will be discussed in Sect. 3.6.1.

3.5.2 Mean-Squared Error in the Time Domain

Fig. 3.4 shows the set-up for computing the time domain error introduced by the channel diagonalization. Given a random input signal $x_Q[k]$, the actual signal $y_Q[k] = (\mathcal{H}x_Q)[k]$ at the output of a random channel $c[k,q]$ appears at the right hand side of the upper chain. Since we are interested in the time domain error now, the analysis operator is not included in the upper chain unlike in Fig. 3.3. In the lower chain the channel output is reproduced by a signal analysis operator, an element-wise multiplication with the channel coefficient

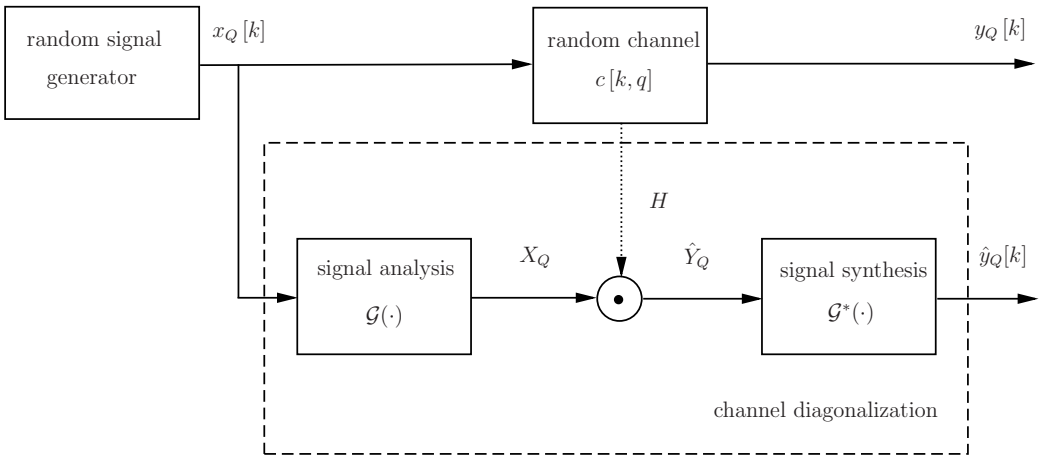

FIGURE 3.4: Set-up for calculating the time domain channel diagonalization error.

and a synthesis operator, which is the channel diagonalization model shown in Fig. 3.2. Thus, the time domain error $e_Q[k]$ is formulated as the difference between the resulting signals from the lower chain $\hat{y}_Q[k]$ and the upper chain $y_Q[k]$, i.e., $e_Q[k] = \hat{y}_Q[k] - y_Q[k]$.

The MSE from the channel diagonalization in the time domain using the set-up in Fig. 3.4 is given by

$$\begin{aligned}\epsilon_{\mathrm{T}}(g) &= \lim_{Q\to\infty} E\left[\frac{1}{Q}\sum_{k=-Q/2}^{Q/2} |e_Q[k]|^2\right] \\ &= \lim_{Q\to\infty} E\left[\frac{1}{Q}\sum_{k=-Q/2}^{Q/2}\left|\sum_{(\ell,m)\in\Lambda} H[\ell,m]\langle x_Q, g_{\ell,m}\rangle g_{\ell,m}[k] - (\mathcal{H}x_Q)[k]\right|^2\right]. \end{aligned} \tag{3.22}$$

Making use of the assumptions at the beginning of this section, the error can be further written as

$$\epsilon_{\mathrm{T}}(g) = 1 + \frac{K}{N}\left(\sum_{(\ell,m)\in\Lambda} \phi_{\mathrm{t}}[\ell N]\phi_{\mathrm{f}}(2\pi m/K)\,|\langle g, g_{\ell,m}\rangle|^2 - 2\Re\left(\langle (g * S_{\mathrm{delay}}) \odot \phi_{\mathrm{t}}, g\rangle\right)\right). \tag{3.23}$$

A detailed derivation of (3.23) from (3.22) can be found in Appendix B. We notice that the first term in the brackets depends on the cross-correlations between different elements of the Gabor frame, weighted by the time and frequency correlation functions, and the second term also appears in $\epsilon_{\mathrm{TF}}(g)$ (3.21) which is regarded as a linear operation on $g[k]$.

Signal analysis using tight frames with $N < K$ results in an overcomplete representation

of the original signal. The time domain error $e_Q[k] = \hat{y}_Q[k] - y_Q[k]$ is related to the TF domain error $E_Q = \hat{Y}_Q - Y_Q$ as

$$e_Q = \mathcal{G}^*(E_Q). \tag{3.24}$$

As from (2.17),

$$\|\mathcal{G}^*(E_Q)\| \leq \|E_Q\|, \tag{3.25}$$

which indicates the MSE in the time domain is not larger than the MSE in the TF domain.

Having formulated both conditions for the window $g[k]$ to define a tight Gabor frame in Sect. 2.4 and resulting MSEs from the channel diagonalization based on $g[k]$, we can now turn to the window design.

3.6 Prototype Design by Convex Optimization

Convex optimization methods aiming at the minimization of convex objective functions are frequently employed in various areas in engineering. Unlike for more general optimization problems, efficient numerical methods are widely available for finding solutions of convex optimization problems. A convex optimization problem [63] has the form

$$\begin{aligned} &\text{minimize} \quad f_0(\mathbf{x}) \\ &\text{subject to} \quad \begin{cases} f_i(\mathbf{x}) \leq 0, i = 1, \ldots, p \\ h_i(\mathbf{x}) = 0, i = 0, \ldots, q \end{cases}, \end{aligned} \tag{3.26}$$

where $\mathbf{x} \in \mathbb{R}^n$ is a vector containing the variables. The functions $\{f_0, \ldots, f_p : \mathbb{R}^n \to \mathbb{R}\}$ are convex, i.e., satisfy

$$f_i\big(\alpha\mathbf{x} + (1-\alpha)\mathbf{y}\big) \leq f_i(\alpha\mathbf{x}) + f_i\big((1-\alpha)\mathbf{y}\big), i = 0, \ldots, p \tag{3.27}$$

for all $\mathbf{x}, \mathbf{y} \in \mathbb{R}^n$ and all $\alpha \in [0, 1]$, and the functions h_i are affine[3]. It is known that for a convex optimization problem, any local optimum is a global optimum. Convex optimization can be classified as geometric programming and quadratic programing which includes SDP, second order cone programming, etc. There are several numerical methods for solving convex optimization problems. The most popular ones among them are interior-point methods which are described in [64, 65].

3.6.1 Formulation of a SDP Problem (TF Domain MSE)

Let us represent the window to be optimized in the vector form $\mathbf{g} \triangleq [g[0] \cdots g[T-1]]^{\mathrm{T}}$ such as to comprise the support of $g[k]$ expressed in Sect. 2.4. We consider real-valued windows $\mathbf{g}$ whose L^2-norm equals $E_{\mathbf{g}}$. The restriction to real-valued windows is common in the literature and limits the complexity. We recall that the TF domain MSE is given by $\epsilon_{\mathrm{TF}}(g) = 2\left(\|g\|^2 - \Re\left[\langle (g * S_{\mathrm{delay}}) \odot \phi_{\mathrm{t}}, g\rangle\right]\right)$ which can be formulated in matrix form as

$$\epsilon_{\mathrm{TF}}(\mathbf{g}) = 2\left(E_{\mathbf{g}} - \Re\left[\mathbf{g}^{\mathrm{T}}\mathbf{B}\mathbf{g}\right]\right), \tag{3.28}$$

[3]A function $f(\mathbf{x})$ is affine if it has the form $f(\mathbf{x}) = \mathbf{A}\mathbf{x} + \mathbf{b}$, which consists of a linear transformation and a translation [63].

where the matrix $\mathbf{B} \in \mathbb{C}^{T\times T}$ describing the delay and Doppler domain distortions of the channel can be expressed as

$$\mathbf{B} = \begin{bmatrix} \phi_{\mathrm{t}}[0]\, S_{\mathrm{delay}}[T-1] & 0 & 0 & 0 & 0 \\ \vdots & \ddots & 0 & 0 & 0 \\ \phi_{\mathrm{t}}[0]\, S_{\mathrm{delay}}\left[\frac{T-1}{2}\right] & \cdots & \phi_{\mathrm{t}}\left[\frac{T-1}{2}\right] S_{\mathrm{delay}}[T-1] & 0 & 0 \\ \vdots & \cdots & \cdots & \ddots & 0 \\ \phi_{\mathrm{t}}[0]\, S_{\mathrm{delay}}[0] & \phi_{\mathrm{t}}[1]\, S_{\mathrm{delay}}[1] & \cdots & \cdots & \phi_{\mathrm{t}}[T]\, S_{\mathrm{delay}}[T-1] \end{bmatrix}. \tag{3.29}$$

Neglecting the constant term $2E_{\mathbf{g}}$, we use $-2\Re\left[\mathbf{g}^{\mathrm{T}}\mathbf{B}\mathbf{g}\right]$ as the objective function for the window optimization. Note that

$$-2\Re\left[\mathbf{g}^{\mathrm{T}}\mathbf{B}\mathbf{g}\right] = -\mathbf{g}^{\mathrm{T}}(\mathbf{B}+\mathbf{B}^{\mathrm{H}})\mathbf{g}, \tag{3.30}$$

and as a consequence the objective function can be rewritten as $\mathbf{g}^{\mathrm{T}}\mathbf{B}_0\mathbf{g}$, where $\mathbf{B}_0 = -(\mathbf{B}+\mathbf{B}^{\mathrm{H}})$ is a Hermitian matrix.

The optimized window $\mathbf{g}$ shall be found to minimize the objective function $\mathbf{g}^{\mathrm{T}}\mathbf{B}_0\mathbf{g}$ for different channel characteristics $\mathbf{B}_0$. In Sect. 2.4, a complete framework is presented for parameterization of tight Gabor frames. In the following, our objective is to find a window $\mathbf{g}$ minimizing ϵ_{TF} and, at the same time, constituting a tight Gabor frame. Thus, the optimization problem is given by

$$\hat{\mathbf{g}} = \arg\min_{\mathbf{g}\in\mathbb{R}^T} \mathbf{g}^{\mathrm{T}}\mathbf{B}_0\mathbf{g}$$

$$\text{subject to} \quad \mathbf{g} \text{ defining a tight frame.} \tag{3.31}$$

Next, we need to incorporate the constraints under which ϵ_{TF} shall be minimized. As discussed in Sect. 2.4, the tight frame constraint in (3.31) is equivalent to B polynomial matrices being paraunitary. With (2.56) we can now translate the polyphase domain constraints (2.45) into constraints on the permuted window defined by $\mathbf{r} = \left[r[0]\cdots r[T-1]\right]^{\mathrm{T}}$, where $T = BLJP$. Therefore (3.31) is expressed as

$$\hat{\mathbf{r}} = \arg\min_{\mathbf{r}\in\mathbb{R}^T} \mathbf{r}^{\mathrm{T}}\mathbf{B}_1\mathbf{r}$$

$$\text{subject to} \quad \mathbf{r}^{\mathrm{T}}\mathbf{A}_l\mathbf{r} = d_l, \quad l = 1,\ldots,W, \tag{3.32}$$

where $d_\ell \in \{K^{-1}, 0\}$ with $l = 1,\ldots,W$, and $\mathbf{B}_1$ is the matrix resulting from $\mathbf{B}_0$ by permuting the rows and columns in accordance with (2.55). We discuss the following two cases based on the number B of the polynomial matrices $\mathbf{W}_b(z), b = 0,\ldots,B-1$.

1. Case $B = 1$: There are J constraints in form of $\mathbf{r}^{\mathrm{T}}\mathbf{A}_\ell\mathbf{r} = K^{-1}$. The ℓth diagonal *constraint matrix* $\mathbf{A}_\ell$ of size $LJP \times LJP$ is defined as

$$[\mathbf{A}_\ell]_{m,n} = \begin{cases} 1 & \text{if } m = n \text{ and } m \in \bigcup\limits_{p=0,\ldots,P-1} \{(pJ+\ell-1)L+1,\ldots,(pJ+\ell)L\} \\ 0 & \text{otherwise} \end{cases}, \tag{3.33}$$

with $\ell = 1,\ldots,J$.

Additionally, there are $J^2P - (J+1)J/2$ constraints $\mathbf{r}^{\mathrm{T}}\mathbf{A}_\ell\mathbf{r} = 0$. The corresponding matrices $\mathbf{A}_{J+1},\ldots,\mathbf{A}_{J^2P-(J-1)J/2}$ can be defined as the elements of the set resulting from deleting duplicate elements and zero-matrices from

$$\Big\{\big(\mathbf{A} \in \mathbb{R}^{LJP\times LJP} \text{ given as } [\mathbf{A}]_{m,n} = I_+(m-jL)\,[\mathbf{A}_\ell]_{m-jL+I_-(m-jL)\cdot LJP,n} + I_+(n-jL)\,[\mathbf{A}_\ell]_{m,n-jL+I_-(n-jL)\cdot LJP}\big) : j = 1,\ldots,JP; \ell = 1,\ldots,J\Big\} \tag{3.34}$$

where

$$I_+(x) = \begin{cases} 1 & x > 0 \\ 0 & x \le 0 \end{cases}, \tag{3.35}$$

and

$$I_-(x) = \begin{cases} 1 & x \le 0 \\ 0 & x > 0 \end{cases}. \tag{3.36}$$

2. Case $B > 1$: From each of the above defined matrices $\mathbf{A}_1,\ldots,\mathbf{A}_{J^2P-(J-1)J/2}$, B unique block diagonal matrices of size $T \times T$ (with $T = BLJP$) are reproduced, each of which contains the original matrix as one of the B diagonal blocks of dimension $LJP \times LJP$.

Hence, there are $W \triangleq B(J^2P-(J-1)J/2)$ constraints in total. The constraint matrices are mutually orthogonal in the sense that $\mathrm{tr}(\mathbf{A}_\ell \mathbf{A}_m^{\mathrm{T}}) = 0$ for $\ell \neq m$.

Let us consider again the example of $N = 6$, $K = 8$, and according to (2.25) $L = 4$, $J = 3$ and $M = 24$. The $B = N/J = 2$ modified matrices $\mathbf{W}_0(z)$ and $\mathbf{W}_1(z)$ of size $L \times J$ are paraunitary, i.e., $\widetilde{\mathbf{W}}_0(z)\mathbf{W}_0(z) = K^{-1}\mathbf{I}_J$, and $\widetilde{\mathbf{W}}_1(z)\mathbf{W}_1(z) = K^{-1}\mathbf{I}_J$. In case of $P = 1$, the matrix $\mathbf{W}_0(z)$ in (2.51) is given by

$$\mathbf{W}_0(z) = \begin{bmatrix} g\,[0] & g\,[8] & g\,[16] \\ g\,[18] & g\,[26] & g\,[34] \\ g\,[12] & g\,[20] & g\,[28] \\ g\,[6] & g\,[14] & g\,[22] \end{bmatrix}, \tag{3.37}$$

and the paraunitary condition on the matrix $\mathbf{W}_0(z)$ can be further expressed as

$$\begin{cases} |g\,[0]|^2 + |g\,[18]|^2 + |g\,[12]|^2 + |g\,[6]|^2 = \frac{1}{8} \\ |g\,[8]|^2 + |g\,[26]|^2 + |g\,[20]|^2 + |g\,[14]|^2 = \frac{1}{8} \\ |g\,[16]|^2 + |g\,[34]|^2 + |g\,[28]|^2 + |g\,[22]|^2 = \frac{1}{8} \\ g\,[0]\,g\,[8] + g\,[18]\,g\,[26] + g\,[12]\,g\,[20] + g\,[6]\,g\,[14] = 0 \\ g\,[8]\,g\,[16] + g\,[26]\,g\,[34] + g\,[20]\,g\,[28] + g\,[14]\,g\,[22] = 0 \\ g\,[0]\,g\,[16] + g\,[18]\,g\,[34] + g\,[12]\,g\,[28] + g\,[6]\,g\,[22] = 0 \end{cases} \tag{3.38}$$

The first equation in (3.38) can be formulated in matrix form as

$$\mathbf{g}^{\mathrm{T}}\bar{\mathbf{A}}_0\mathbf{g} = \frac{1}{8}, \quad \text{with } \bar{\mathbf{A}}_0 = \mathrm{Diag}([1\,0\,0\,0\,0\,0\,1\,0\,0\,0\,0\,0\,1\,0\,0\,0\,0\,0\,1\,0\,0\,0\,0\,0]). \tag{3.39}$$

Employing the sample permutation of the window function in (2.55), we use the resulting vector $\mathbf{r}$ instead of $\mathbf{g}$. The matrix $\bar{\mathbf{A}}_0$ can be reformulated as $\mathbf{A}_0$ taking the sample permutation into account. Thus (3.39) is rewritten as

$$\mathbf{r}^{\mathrm{T}}\mathbf{A}_0\mathbf{r} = \frac{1}{8}, \quad \text{with } \mathbf{A}_0 = \mathrm{Diag}([1\,1\,1\,1\,0\,0\,0\,0\,0\,0\,0\,0\,0\,0\,0\,0\,0\,0\,0\,0\,0\,0\,0\,0]). \tag{3.40}$$

Similarly, $\mathbf{A}_1$ for the second equation in (3.38) is given by

$$\mathbf{A}_1 = \mathrm{Diag}([0\,0\,0\,0\,1\,1\,1\,1\,0\,0\,0\,0\,0\,0\,0\,0\,0\,0\,0\,0\,0\,0\,0\,0]), \tag{3.41}$$

and all the remaining equations can be written in matrix forms accordingly.

Let us introduce a matrix $\mathbf{R} \triangleq \mathbf{r}\mathbf{r}^{\mathrm{T}}$, and thus the objective function $\mathbf{r}^{\mathrm{T}}\mathbf{B}_1\mathbf{r}$ can be written as $\mathrm{tr}(\mathbf{B}_1\mathbf{R})$. The semidefinite relaxation of (3.32) is given by

$$\hat{\mathbf{R}} = \arg\min_{\mathbf{R}\in\mathcal{S}_T} \operatorname{tr}(\mathbf{B}_1\mathbf{R})$$

$$\text{subject to} \quad \begin{cases} \mathbf{R} \geq 0 \\ \operatorname{tr}(\mathbf{A}_l\mathbf{R}) = d_l, \quad l = 1, \ldots, W \end{cases}, \tag{3.42}$$

where $\mathcal{S}_T$ represents the vector space of symmetric matrices of dimension $T\times T$, and $\mathbf{R} \succeq 0$ denotes that $\mathbf{R}$ is positive semidefinite. Via the iterative interior-point algorithm [66], $\hat{\mathbf{R}}$ can be computed numerically. Having found a matrix $\hat{\mathbf{R}} \in \mathcal{S}_T$ corresponding to a global minimum of (3.42), we have two possible cases. If $\operatorname{rank}(\hat{\mathbf{R}}) = 1$, a solution $\hat{\mathbf{r}}$ of (3.32) is readily obtainable from $\hat{\mathbf{r}}\hat{\mathbf{r}}^{\mathrm{H}} = \hat{\mathbf{R}}$ and the optimal window $g_{\mathrm{SDP}}[k]$ is found through (2.55). If $\operatorname{rank}(\hat{\mathbf{R}}) > 1$, which we observe in most of the cases, rank reduction methods must be employed. We compute a possibly suboptimal window $g_{\mathrm{SDP}}[k]$ by the following three steps:

1. We first find the rank-1 matrix $\hat{\mathbf{R}}_0$ which has the least Euclidian distance to $\hat{\mathbf{R}}$. The approximation problem can be represented as

$$\hat{\mathbf{R}}_0 = \arg\min_{\mathbf{R}\in\mathcal{S}_T} \left\|\mathbf{R} - \hat{\mathbf{R}}\right\|$$

$$\text{subject to} \quad \operatorname{rank}(\mathbf{R}) = 1. \tag{3.43}$$

   Since $\hat{\mathbf{R}}$ is a Hermitian matrix, it can be written in the form of $\hat{\mathbf{R}} = \mathbf{V}\Sigma\mathbf{V}^{\mathrm{H}}$ by its eigenvalue decomposition, where Σ is a diagonal matrix containing the eigenvalues of $\hat{\mathbf{R}}$, and the square matrix $\mathbf{V}$ contains all the eigenvectors. We resort to the matrix $\hat{\mathbf{R}}_0 = (N/K)\mathbf{v}_0\mathbf{v}_0^{\mathrm{H}}$ composed by the dominant eigenvector $\mathbf{v}_0$ of $\hat{\mathbf{R}}$, since $\hat{\mathbf{R}}_0$ is the matrix nearest to $\hat{\mathbf{R}}$ in terms of the Frobenius norm [67].

2. From $\hat{\mathbf{R}}_0 = \hat{\mathbf{r}}_0\hat{\mathbf{r}}_0^{\mathrm{H}}$ we obtain the vector $\hat{\mathbf{r}}_0 = \sqrt{N/K}\mathbf{v}_0$, and then $\hat{\mathbf{r}}_0$ is translated into a window $\hat{g}_0[k]$ taking the sample permutation defined in (2.55) into account.

3. After the rank reduction in the first step, the constraints in (3.42) do not hold anymore, i.e., the resulting window $\hat{g}_0[k]$ generally does not constitute a tight Gabor

frame. We finally obtain $g_{\mathrm{SDP}}[k]$ by the algorithm [68], i.e.,

$$g_{\mathrm{SDP}} = (\mathcal{S}^{-1/2}\hat{g}_0), \tag{3.44}$$

where $\mathcal{S}^{-1/2}$ denotes the square root of the inverse frame operator $\mathcal{S}$ discussed in Sect. 2.2. In fact, (3.44) yields a window $g_{\mathrm{SDP}}[k]$ defining a canonical tight frame with frame bound 1 and, at the same time, minimizing the distance to a given window (i.e., $\hat{g}_0[k]$) in terms of the L^2-norm.

3.6.2 Formulation of a Convex Optimization Problem (Time Domain MSE)

In this section we consider the window optimization minimizing the time domain MSE. The time domain MSE $\epsilon_{\mathrm{T}}(g)$ of the channel diagonalization can be formulated as a convex function under certain weak assumptions. We consider only real-valued windows as in the last subsection. In order to eventually arrive at a CO problem, we impose the following restrictions on the channel statistics:

- The time correlation function is subject to $\phi_{\mathrm{t}}[\ell] \geq 0 \ \forall \ell \in \mathbb{Z}$, as being the case for Laplacian and many other symmetric Doppler power spectra.
- The frequency correlation function fulfills $\phi_{\mathrm{f}}(2\pi m/K) + \phi_{\mathrm{f}}(-2\pi m/K) \geq 0$ $\forall m \in \{0, \ldots, K-1\}$, as for instance in the case of exponentially decaying delay power spectra.

We use (3.23) as the objective function, and the term $|\langle g, g_{\ell,m}\rangle|^2$ can be expressed as $\left(\mathbf{g}^{\mathrm{T}}\Re(\mathbf{E}_{\ell,m})\mathbf{g}\right)^2 + \left(\mathbf{g}^{\mathrm{T}}\Im(\mathbf{E}_{\ell,m})\mathbf{g}\right)^2$ using (2.2). Choosing $\ell = 1, m = 1$ and $P = 1$ as an

example, the square matrix $\mathbf{E}_{1,1}$ of dimension $T \times T$ is expressed as

$$\mathbf{E}_{1,1} = \begin{bmatrix} 0 & 0 & \cdots & & & & \cdots & 0 \\ \vdots & & & & & & & 0 \\ 0 & 0 & \cdots & & & & & 0 \\ 1 & 0 & \vdots & & & & & 0 \\ 0 & \exp\left(\frac{\jmath 2\pi}{K}\right) & 0 & \cdots & & & & 0 \\ 0 & 0 & \exp\left(\frac{\jmath 4\pi}{K}\right) & 0 & \vdots & & & 0 \\ 0 & \cdots & 0 & \ddots & 0 & \cdots & & 0 \\ 0 & \cdots & & 0 & \exp\left(\frac{\jmath 2(M-N-1)\pi}{K}\right) & 0 & \cdots & 0 \end{bmatrix}, \tag{3.45}$$

where $T = M$ is the least common multiple of N and K, and the entries of the first $\ell \cdot N$ rows are all zeros. The term $-2\Re\big(\langle (g * S_{\text{delay}}) \odot \phi_{\text{t}}, g\rangle\big)$ of the objective function can be written in matrix form as discussed in the last subsection. As a consequence, the objective function (3.23) can be expressed in the form

$$\epsilon_{\text{T}}(\mathbf{g}) = \sum_{k=1}^{F} c_k \left(\mathbf{g}^{\text{T}}\mathbf{C}_k\mathbf{g}\right)^2 + \mathbf{g}^{\text{T}}\mathbf{D}\mathbf{g} + 1 \tag{3.46}$$

for some $F \in \mathbb{N}$ depending on the support of $g[k]$, where $\mathbf{C}_1, \ldots, \mathbf{C}_F, \mathbf{D}$ are real matrices and the constants $c_1, \ldots, c_F$ are positive given the above restrictions.

We can now formulate the optimization problem in the form

$$\min_{\mathbf{r}\in\mathbb{R}^T} \sum_{k=1}^{F} c_k \left(\mathbf{r}^{\text{T}}\bar{\mathbf{C}}_k\mathbf{r}\right)^2 + \mathbf{r}^{\text{T}}\bar{\mathbf{D}}\mathbf{r}$$

$$\text{subject to} \quad \mathbf{r}^{\text{T}}\mathbf{A}_\ell\mathbf{r} = d_\ell, \quad \ell = 1, \ldots, W, \tag{3.47}$$

where $\bar{\mathbf{C}}_1, \ldots, \bar{\mathbf{C}}_F, \bar{\mathbf{D}}$ are the matrices resulting from $\mathbf{C}_1, \ldots, \mathbf{C}_F, \mathbf{D}$ by permuting the rows and columns in accordance with (2.55), and $d_\ell \in \{K^{-1}, 0\}$. Let us use $\mathbf{R} = \mathbf{r}\mathbf{r}^{\text{T}}$ to reformulate the optimization problem as

$$\min_{\mathbf{R}\in\mathcal{S}_T} \sum_{k=1}^{F} c_k \text{tr}^2\left(\mathbf{R}\bar{\mathbf{C}}_k\right) + \text{tr}\left(\mathbf{R}\bar{\mathbf{D}}\right)$$

$$\text{subject to} \quad \begin{cases} \text{tr}\left(\mathbf{R}\mathbf{A}_\ell\right) = d_\ell, \quad \ell = 1, \ldots, W \\ \text{rank}(\mathbf{R}) = 1 \end{cases} . \tag{3.48}$$

In (3.48) we have a convex objective function, however, the set $\{\mathbf{R} \in \mathcal{S}_T \ : \ \text{rank}(\mathbf{R}) = 1\}$ is non-convex[4]. Resorting to semidefinite relaxation, we obtain

$$\min_{\mathbf{R}\in\mathcal{S}_T} \sum_{k=1}^{F} c_k \text{tr}^2\left(\mathbf{R}\bar{\mathbf{C}}_k\right) + \text{tr}\left(\mathbf{R}\bar{\mathbf{D}}\right)$$

$$\text{subject to} \quad \begin{cases} \text{tr}\left(\mathbf{R}\mathbf{A}_\ell\right) = d_\ell, \quad \ell = 1, \ldots, W \\ \mathbf{R} \succeq 0 \end{cases} . \tag{3.49}$$

Since $\mathcal{S}_T^+ = \{\mathbf{R} \in \mathcal{S}_T \ : \ \mathbf{R} \succeq 0\}$ is a convex subset of $\mathcal{S}_T$, we now have a CO problem [63].

A simple gradient method can be used to find the optimum solution of unconstrained CO problems. In the following, the constraints in (3.49) are transformed for applying the gradient method. Our first step is to rewrite the problem (3.49), making the inequality constraint $\mathbf{R} \succeq 0$ implicit in the objective:

$$\min_{\mathbf{R}\in\mathcal{S}_T} \sum_{k=1}^{F} c_k \text{tr}^2\left(\mathbf{R}\bar{\mathbf{C}}_k\right) + \text{tr}\left(\mathbf{R}\bar{\mathbf{D}}\right) + I(\mathbf{R})$$

$$\text{subject to} \quad \text{tr}\left(\mathbf{R}\mathbf{A}_\ell\right) = d_\ell, \quad \ell = 1, \ldots, W, \tag{3.50}$$

where $I(\mathbf{X})$ is an indicator function defined as

$$I(\mathbf{X}) = \begin{cases} 0 & \mathbf{X} \in \mathcal{S}_T^+ \\ +\infty & \text{otherwise} \end{cases} . \tag{3.51}$$

The *logarithmic barrier function* defined as

$$f(\mathbf{X}) = \begin{cases} -\frac{1}{\mu} \ln \det(\mathbf{X}) & \mathbf{X} \in \mathcal{S}_T^+ \\ +\infty & \text{otherwise} \end{cases} , \tag{3.52}$$

with $\det(\cdot)$ denoting the determinant of a matrix and $\mu > 0$, can be employed for approximating the indicator function (3.51). The quality of the approximation improves when

[4]Clearly, given two $N \times N$ matrices $\mathbf{A}$ and $\mathbf{B}$ with rank 1, a linear combination $c\mathbf{A} + (1-c)\mathbf{B}$, with $c \in (0, 1)$, is in general a matrix with rank 2.

μ increases. The logarithmic barrier function $f(\mathbf{X})$ is a convex function like the indicator function $I(\mathbf{X})$, and moreover $f(\mathbf{X})$ is differentiable [63]. We use $f(\mathbf{R})$ to replace $I(\mathbf{R})$ in (3.50). Then, the resulting objective function reads

$$\sum_{k=1}^{F} c_k \mathrm{tr}^2\left(\mathbf{R}\bar{\mathbf{C}}_k\right) + \mathrm{tr}\left(\mathbf{R}\bar{\mathbf{D}}\right) + f(\mathbf{R}). \tag{3.53}$$

Since the logarithmic barrier function $f(\mathbf{X})$ is infinite when $\mathbf{X} \notin \mathcal{S}_T^+$ and almost zero when $\mathbf{X} \in \mathcal{S}_T^+$ and $\frac{1}{\mu}$ approaches zero, the minimum values of the new objective function in (3.53) and the original objective function (3.49) are the same. Our second step is to handle the equality constraints $\mathrm{tr}\left(\mathbf{R}\mathbf{A}_\ell\right) = d_\ell, \ell = 1, \ldots, W$, in (3.49). Note that the constraint matrices $\mathbf{A}_\ell, \ell = 1, \ldots, W$, are mutually orthogonal, i.e., $\mathrm{tr}(\mathbf{A}_l\mathbf{A}_m) = 0$ for $l \neq m$, and they span a vector space $\mathbb{W}$. Any $\mathbf{R}$ fulfilling the constraints can be written as

$$\mathbf{R} = \mathbf{R}_{\mathbb{W}^\perp} + \mathbf{R}_0, \tag{3.54}$$

where $\mathbf{R}_0$ is a constant matrix given by

$$\mathbf{R}_0 = \sum_{\ell=1}^{W} d_\ell \frac{\mathbf{A}_\ell}{\|\mathbf{A}_\ell\|}, \tag{3.55}$$

and $\mathbf{R}_{\mathbb{W}^\perp} \in \mathbb{W}^\perp$ with $\mathbb{W}^\perp$ denoting the vector space orthogonal to $\mathbb{W}$. Therefore, the CO problem (3.49) can be rewritten as

$$\min_{\hat{\mathbf{R}} \in \mathbb{W}^\perp} \sum_{k=1}^{F} c_k \mathrm{tr}^2\left(\left(\hat{\mathbf{R}} + \mathbf{R}_0\right)\bar{\mathbf{C}}_k\right) + \mathrm{tr}\left(\left(\hat{\mathbf{R}} + \mathbf{R}_0\right)\bar{\mathbf{D}}\right) - \frac{1}{\mu}\ln\det(\hat{\mathbf{R}} + \mathbf{R}_0). \tag{3.56}$$

The gradient in the subspace $\mathbb{W}^\perp$ is obtained by an orthonormal projection of the gradient in $\mathcal{S}_T$ onto $\mathbb{W}^\perp$. We use the opposite direction of the resulting gradient vector. A reasonable step is chosen via the inexact line search [63] such that the objective function decreases in each iteration. When the norm of the gradient is very close to zero after a number of iterations indicating proximity to the minimum of the current objective function, we increase the value of μ, and repeat the whole process until the logarithmic barrier function is approximately zero.

Having found a matrix $\hat{\mathbf{R}} \in \mathcal{S}_T$ corresponding to a global minimum of (3.49), there are two possible cases. If $\text{rank}(\hat{\mathbf{R}}) = 1$, a solution $\hat{\mathbf{r}}$ of (3.47) can be obtained from $\hat{\mathbf{r}}\hat{\mathbf{r}}^{\mathrm{T}} = \hat{\mathbf{R}}$ and the optimal window $g_{\mathrm{CO}}[k]$ is found through (2.55). If $\text{rank}(\hat{\mathbf{R}}) > 1$, rank reduction methods must be employed. A suboptimal window $g_{\mathrm{CO}}[k]$ is found by steps being similar to those presented in Sect. 3.6.1.

3.7 Numerical Results

We consider a WSSUS channel with unit average channel gain (i.e., $\phi_{\mathrm{f}}[0] = \phi_{\mathrm{t}}[0] = 1$) and an exponentially decaying delay power spectrum, the sampled version of which reads

$$S_{\mathrm{delay}}[q] = u(q)\,(1 - \exp(-1/\tau_{\mathrm{RMS}}))\exp(-q/\tau_{\mathrm{RMS}}) \tag{3.57}$$

with $u(q)$ denoting the unit step function and τ_{RMS} the RMS delay spread. Typical values of RMS delay spread are in the order of microseconds in outdoor mobile channels and nanoseconds in the case of short-range radio indoor environments [69]. For the Doppler power spectrum, a two-sided exponentially decaying shape is assumed, which results in the time correlation function

$$\phi_{\mathrm{t}}[k_\Delta] = \frac{1}{1 + 2\pi^2\nu_{\mathrm{RMS}}^2\,|k_\Delta|^2}, \tag{3.58}$$

where ν_{RMS} represents the RMS Doppler spread. Since choosing an oversampling factor K/N larger than one increases the degrees of freedom in the window design, we restrict our attention to scenarios with $K > N$, involving oversampled FBs.

Fig. 3.5 shows optimized window functions $g_{\mathrm{SDP}}[k]$ and $g_{\mathrm{CO}}[k]$ for a doubly dispersive channel with an RMS delay spread $\tau_{\mathrm{RMS}} = 1$ and an RMS Doppler spread $\nu_{\mathrm{RMS}} = 0.01$, as well as their Fourier transforms. The waveforms are obtained numerically for $N = 24$, $K = 32$, $P = 2$, amounting to a window length of 240 samples. The optimized windows are found via SDP and CO, and the Fourier transforms of the optimized windows in (a), (b), resp., versus the normalized frequency $\omega/2\pi$ are shown in Fig. 3.5 (c), (d). The two optimized windows achieve MSEs of $\epsilon_{\mathrm{TF}}(g_{\mathrm{SDP}}) = -8.72$ dB and $\epsilon_{\mathrm{T}}(g_{\mathrm{CO}}) = -9.49$ dB,

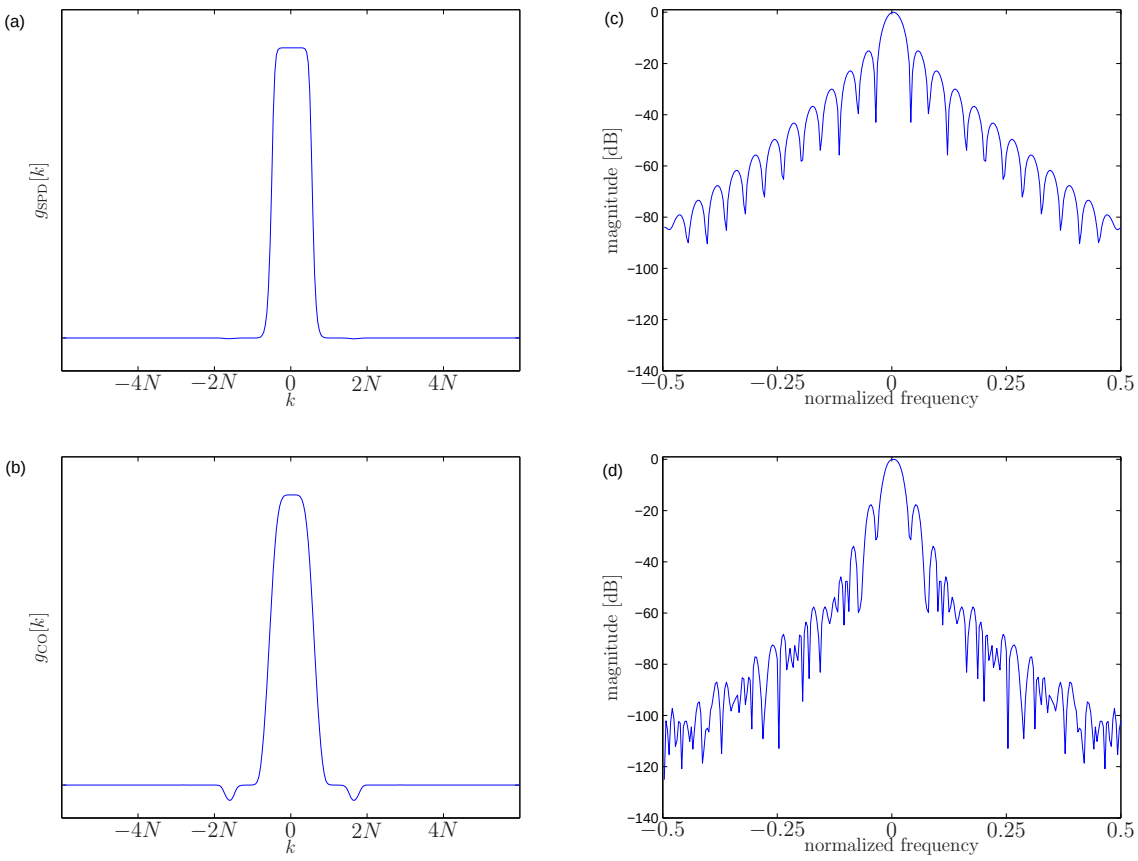

FIGURE 3.5: Examples of optimized window functions $g_{\mathrm{SDP}}[k]$ and $g_{\mathrm{CO}}[k]$ in time domain (left side) and in frequency domain (right side) for $\tau_{\mathrm{RMS}} = 1, \nu_{\mathrm{RMS}} = 0.01$.

where the error is represented in decibel, i.e., $10\log_{10}(\cdot)$. The time domain MSE ϵ_{T} is less than the TF domain MSE ϵ_{TF} as discussed in Sect. 3.5.

By increasing the polynomial order of the matrices $\mathbf{W}_0(z), \ldots, \mathbf{W}_{B-1}(z)$, longer windows are available. The dimension of the optimization problem is increased, as well as the number of constraints. Fig. 3.6 shows the optimized windows $g_{\mathrm{SDP}}[k]$ obtained by solving (3.42) via SDP for $\tau_{\mathrm{RMS}} = 1$ and $\nu_{\mathrm{RMS}} = 10^{-5}$. In Fig. 3.6 (a), $N = 48$, $K = 64$, $P = 1$, amounting to a window length of 384 samples, and in Fig. 3.6 (b) $N = 48$, $K = 64$, $P = 3$, resulting in a waveform of 768 samples. Fig. 3.6 (c) and (d) show the respective Fourier transforms. It is obvious that the optimized window with longer support is more smooth in the time domain. Moreover, the MSE of the optimized window in Fig. 3.6 (b) is -29.83 dB, and it is less than the MSE of the window in Fig. 3.6 (a) which is -28.44 dB. We also observe that the optimized windows $g_{\mathrm{CO}}[k]$ via CO results in a reduced MSE

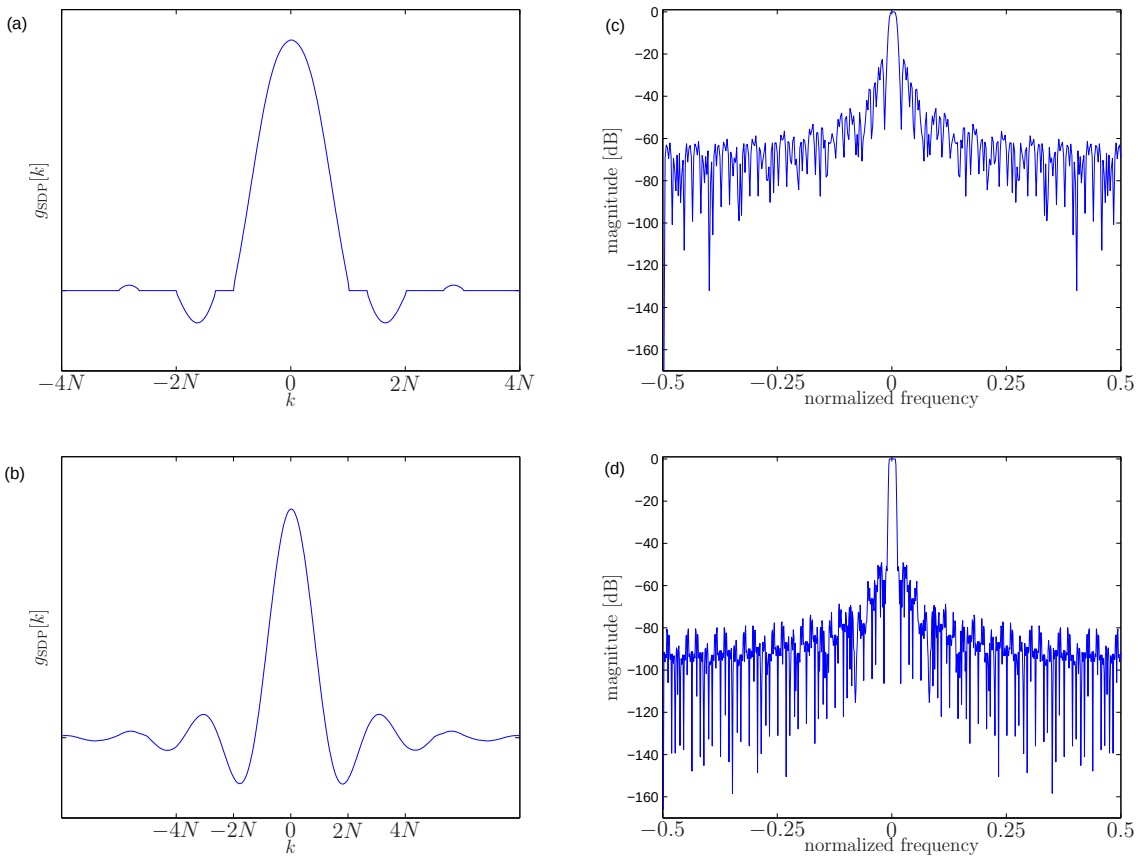

FIGURE 3.6: Examples of optimized window functions via SDP in time domain (left side) and in frequency domain (right side) for different polynomial orders: (a) and (c), $P = 1$; (b) and (d), $P = 3$.

when P increases, however at the cost of an increasing computational complexity.

Fig. 3.7 shows the optimized pulses $g_{\mathrm{CO}}[k]$ obtained by numerically solving the CO problem (3.49) for different channel conditions. An RMS delay spread $\tau_{\mathrm{RMS}} = 3$ and an RMS Doppler spread $\nu_{\mathrm{RMS}} = 0.001$ are assumed in Fig. 3.7 (a), while $\tau_{\mathrm{RMS}} = 3$, $\nu_{\mathrm{RMS}} = 0.01$ in Fig. 3.7 (b). Fig. 3.7 (c) and (d) show the Fourier transforms of the optimized windows in (a) and (b). Obviously, the optimized waveforms become more concentrated in the time domain as the Doppler spread increases (see Fig. 3.7 (b) versus Fig. 3.7 (a)). For increasing Doppler spreads the coherence time of the channel decreases, and thus to limit the MSE the optimized windows have a smaller support. The two shown optimized windows achieve MSEs of -16.01 dB and -8.44 dB, respectively.

Note that the TF shifted versions of the optimized window are used for the channel

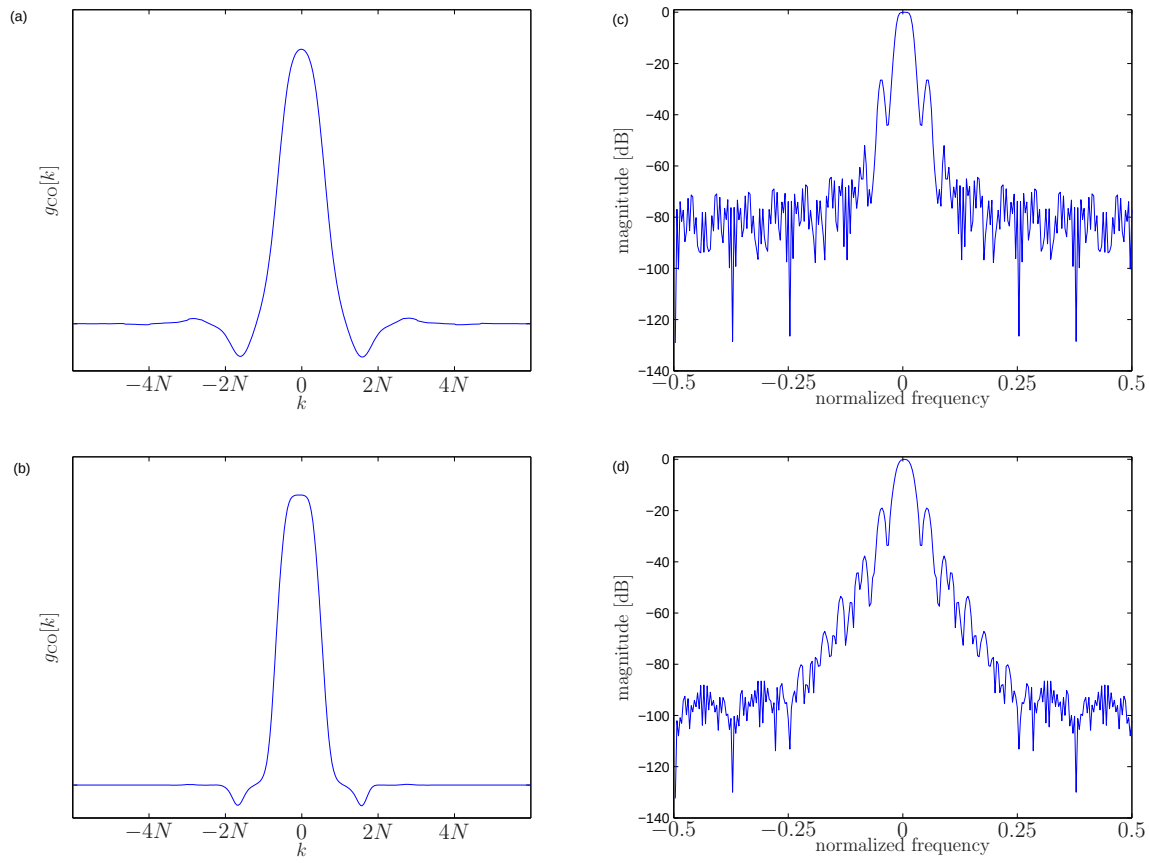

FIGURE 3.7: Examples of optimized window functions via CO in time domain (left side) and in frequency domain (right side) for different channel statistics: (a) and (c), $\tau_{\mathrm{RMS}} = 3, \nu_{\mathrm{RMS}} = 0.001$; (b) and (d), $\tau_{\mathrm{RMS}} = 3, \nu_{\mathrm{RMS}} = 0.01$.

diagonalization. The cross-correlations between the optimized window $g\,[k]$ and its TF shifted versions $\{g_{\ell,m}\,[k] : (\ell, m) \in \Lambda\}$ is known as *ambiguity function*. For $g \in L^2(\mathbb{Z})$, the ambiguity function of g is defined by

$$A_g[\ell, m] = \langle g, g_{\ell,m} \rangle \,, \tag{3.59}$$

where $g_{\ell,m}$ is given by (2.2) as $g_{\ell,m}\,[k] = g\,[k - \ell N] \exp(\jmath 2\pi(k - \ell N)m/K)$ with ℓ, m representing the indices of the time and frequency shifts, respectively. Fig. 3.8 shows as an example the absolute value of the ambiguity function $|A_{g_{\mathrm{CO}}}[\ell, m]|$ obtained from CO with $N = 24$, $K = 32$, $P = 2$ for a channel with $\tau_{\mathrm{RMS}} = 5$, $\nu_{\mathrm{RMS}} = 0.01$. It is shown in Fig. 3.8 that the ambiguity function of the optimized window is concentrated in a small area, which indicates that the optimized window is highly correlated only with functions being

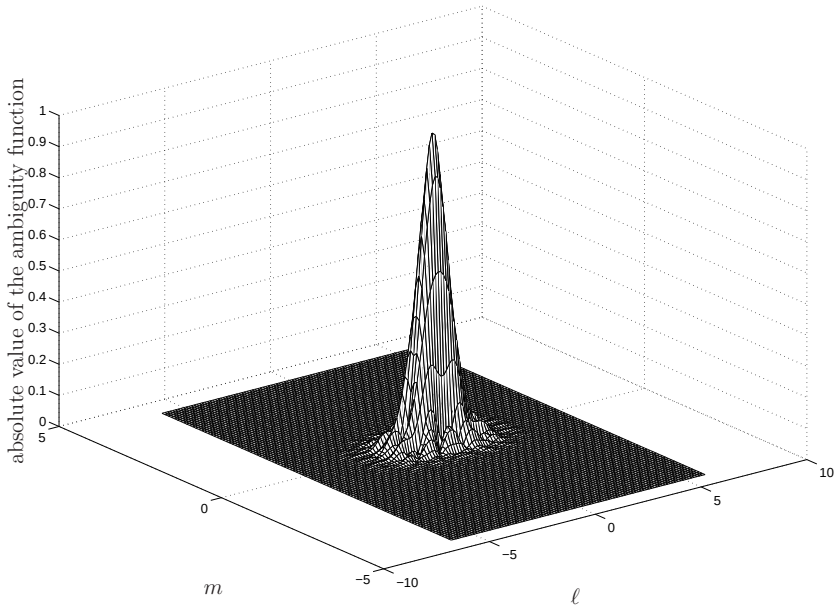

FIGURE 3.8: Ambiguity function of the optimized window $g_{\mathrm{CO}}[k]$ with $N = 24$, $K = 32$, $P = 2$ for a channel with $\tau_{\mathrm{RMS}} = 5$, $\nu_{\mathrm{RMS}} = 0.01$.

located in the direct neighborhood in the TF domain. Hence, the optimized window function has a relatively good TF concentration property.

The achievable MSEs (3.23) by optimized windows are shown in Fig. 3.9 for $N = 24$, $K = 32$, $P = 2$. The RMS delay spread τ_{RMS} ranges between 1 and 8 samples while the RMS Doppler spread ν_{RMS} equals 10^{-2}. For every considered τ_{RMS} a window $g_{\mathrm{CO}}[k]$ is obtained by numerically solving the CO problem (3.49), and a window $g_{\mathrm{SDP}}[k]$ by solving (3.42) through SDP, where both approaches require the aforementioned additional steps for rank reduction. The global minimum of the objective function in (3.49), that is prior to the rank reduction, serves as a lower bound in the figure. The offsets of $\epsilon_{\mathrm{T}}(g_{\mathrm{CO}})$ and $\epsilon_{\mathrm{T}}(g_{\mathrm{SDP}})$ from the lower bound reflect the impact of the rank reduction. Additionally, the figure shows the MSEs resulting from choosing a window $g_{\mathrm{RRC}}[k]$ with a root-raised-cosine (RRC) shaped magnitude spectrum with width $2\pi/K$ and roll-off factor $K/N-1$. We choose this window function for comparison since it can be shown that the window $g_{\mathrm{RRC}}[k]$ with the aforementioned parameter can constitute a tight Gabor frame while exhibiting superior TF localization properties compared to rectangularly shaped windows. Finally, for the verification of $\epsilon_{\mathrm{T}}(g_{\mathrm{CO}})$, we also run system-level Monte-Carlo

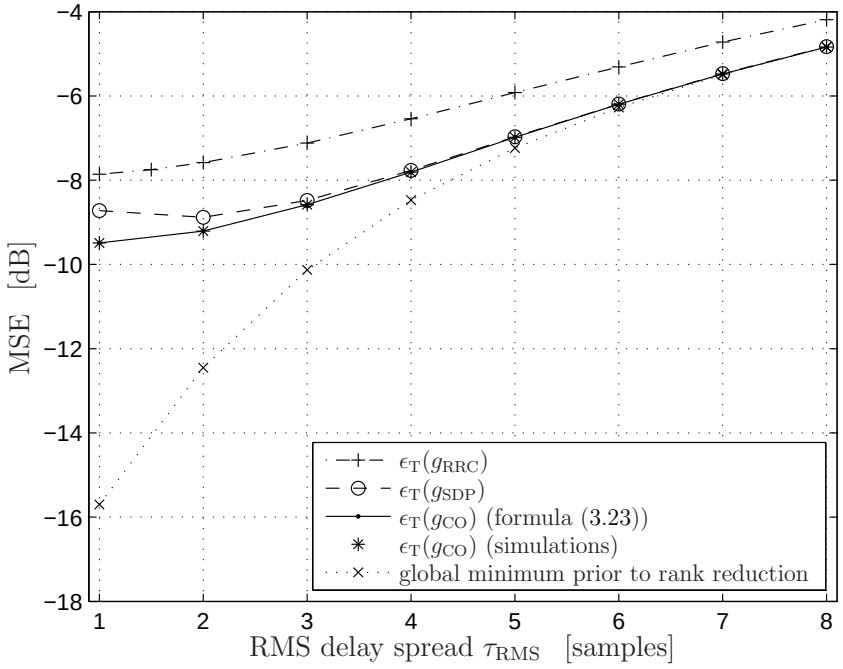

FIGURE 3.9: Model errors by windows $g_{\mathrm{CO}}[k]$ and $g_{\mathrm{SDP}}[k]$ optimized through CO and SDP, resp., and by window $g_{\mathrm{RRC}}[k]$ with RRC shaped magnitude spectrum versus τ_{RMS} at $\nu_{\mathrm{RMS}} = 10^{-2}$.

simulations involving the actual FBs based on the optimized windows $g_{\mathrm{CO}}[k]$. The input signals x and WSSUS channels are generated by random number generators, and the signals $y = \mathcal{H}x$ and $\hat{y} = \mathcal{G}^*(H \odot (\mathcal{G}x))$ are obtained. An analysis of the error signals leads to the same results as given by $\epsilon_{\mathrm{T}}(g_{\mathrm{CO}})$.

Obviously, solving (3.49) leads to pulses with better performance than solving (3.42) for RMS delay spreads less than 5 samples. For larger τ_{RMS} the resulting MSEs are almost the same, where the toll taken by the rank reduction following CO exceeds the one following SDP. The considerable offset of the MSEs from the lower bound for smaller τ_{RMS} further indicates that here the rank reduction has a significant impact on the windows. We observe that rank reduction generally has a limited effect when the delay and Doppler spreads are of similar extent, that is, when in the TF plane the delay spread relative to the sampling interval in time (i.e., τ_{RMS}/N) is of the same order of magnitude as the Doppler spread relative to the sampling interval in frequency (i.e., $\nu_{\mathrm{RMS}}/K^{-1}$). For example, for the scenario with $\tau_{\mathrm{RMS}} = 1$, $\nu_{\mathrm{RMS}} = 0.01$, the optimized window via CO for $N = 24$, $K = 32$, $P = 2$ results in a MSE of -9.49 dB which is shown in Fig. 3.9. To limit the

effect of the rank reduction, we change the lattice constants to be $N = 9$, $K = 12$, however keeping the oversampling ratio K/N as 4/3, and in this case $\tau_{\mathrm{RMS}}/N \approx \nu_{\mathrm{RMS}}/K^{-1}$. The resulting optimized window has a much better performance, which results in a MSE of -16.12 dB. Note that this result is not shown in Fig. 3.9.

The relatively high MSEs found in Fig. 3.9 are a result of the product $\tau_{\mathrm{RMS}}\nu_{\mathrm{RMS}}$ being in the order of 10^{-2}, a much larger value than encountered in typical mobile radio scenarios. In environments with such severe dispersion in both time and frequency, the model error performance can actually be improved by increasing the oversampling ratio K/N. This can be seen in Tab. 3.1, showing some values of $\epsilon_{\mathrm{T}}(g_{\mathrm{CO}})$, $\epsilon_{\mathrm{T}}(g_{\mathrm{SDP}})$ and $\epsilon_{\mathrm{TF}}(g_{\mathrm{SDP}})$ observed for choosing different oversampling ratios. An RMS delay spread of 1 sample and a RMS

N	K	oversampl. ratio	$\epsilon_{\mathrm{TF}}(g_{\mathrm{SDP}})$	$\epsilon_{\mathrm{T}}(g_{\mathrm{SDP}})$	$\epsilon_{\mathrm{T}}(g_{\mathrm{CO}})$
24	32	4/3	-8.29 dB	-7.39 dB	-9.49 dB
20	32	8/5	-9.89 dB	-8.48 dB	-11.78 dB
16	32	2	-12.06 dB	-9.69 dB	-14.83 dB
12	32	8/3	-15.38 dB	-10.90 dB	-18.57 dB
8	32	4	-21.09 dB	-11.70 dB	-22.43 dB
4	32	8	-23.25 dB	-11.79 dB	-23.85 dB

TABLE 3.1: Model error for different oversampling ratios.

Doppler spread $\nu_{\mathrm{RMS}} = 0.01$ are assumed here, and $P = 2$. The oversampling ratio K/N is increased from 4/3 to 8 by decreasing the down-sampling factor N from 24 to 4. The number of sub-bands K is fixed to 32. Both TF and time domain MSE performances clearly improve with the oversampling ratio. Again, as discussed before, the performance of the windows obtained from the CO is always better in comparison with the windows obtained from the SDP.

Chapter 4

Generic Reconfigurable Receiver Architecture

In this chapter, we investigate the design of a reconfigurable baseband receiver architecture which is capable of dealing with various signals from different air interfaces. The proposed TF channel diagonalization in Chap. 3 does not rely on a particular signal format (e.g., single-carrier GSM signals, multi-carrier WLAN signals, spread-spectrum UMTS signals), making it suitable for flexible radio systems. In the following, a flexible baseband receiver architecture is discussed which is based upon the TF channel diagonalization. The receiver includes several key modules implementing signal processing tasks in the TF domain. In addition, the proposed architecture can be configured to both a matched filtering based receiver and an equalization based receiver.

The burst structures defined in the various standards for cellular systems and wireless local and personal area networks differ substantially. However, commonly the bursts incorporate preamble and pilot signals for the synchronization and channel parameter estimation as well as information-bearing signals which are usually subject to a linear modulation scheme. Therefore, we assume in the following that the baseband transmit signals generally follow the form

$$x[k] = \sum_{q=1}^{Q} s_q z_q[k] + p[k] \tag{4.1}$$

with $s_1, \ldots, s_Q$ denoting Q information signals which modulate the elementary waveforms $z_1[k], \ldots, z_Q[k]$, and $p[k]$ representing the pilot signal. An elementary waveform can, for example, be a complex exponential as in the case of OFDM signals, or have the form of a pseudo-noise (PN) sequence as in the case of direct-sequence spread-spectrum (DSSS) signaling. For the purpose of channel estimation at the receiver, a preamble/pilot signal $p[k]$ is often transmitted. The preamble/pilot signal may be confined to isolated time intervals, or exhibit constant power as in the case of a CDMA system with a dedicated pilot channel to be transmitted in the same time and frequency slots as the information bearing signals $s_q z_q[k]$.

The baseband signal at the receiver reads

$$y[k] = (\mathcal{H}x)[k] + v[k], \tag{4.2}$$

where $v[k]$ represents the additive front-end noise, which is a white random process. The TF representation of a burst $y[k]$ to be processed comprises K samples in the frequency dimension (corresponding to the number of FB elements) and D samples in time dimension for a total of DK samples, constituting a $K \times D$ matrix $\mathbf{Y}$. The DK samples relate to the TF grid points in the set

$$\{0, N, \ldots, (D-1)N\} \times \left\{0, \frac{2\pi}{K}, \ldots, \frac{2\pi(K-1)}{K}\right\}, \tag{4.3}$$

where N is the spacing in time (corresponding to the down-sampling factor of the FB), and $\frac{2\pi}{K}$ is the spacing in frequency which is discussed in Sect. 2.2. In this chapter, the TF representations of signals are denoted in the aforementioned matrix forms.

Fig. 4.1 sketches the structure of the reconfigurable baseband receiver. The time-discrete received signal $y\,[k]$ is represented in the TF domain as $\mathbf{Y}$ at the output of the analysis FB. The $K \times D$-dimensional TF matrix representations $\mathbf{Z}_1, \ldots, \mathbf{Z}_Q$, and $\mathbf{P}$ of the elementary waveforms $z_1[k], \ldots, z_Q[k]$ and the pilot signal $p[k]$, resp., are not necessary to be computed on-line by analysis FBs, but they can be pre-computed and read from local repositories. The locally reproduced pilot signal representation $\mathbf{P}$ is used together with the TF representation $\mathbf{Y}$ of the received signal to calculate an estimate $\hat{\mathbf{H}}$ of the matrix $\mathbf{H}$

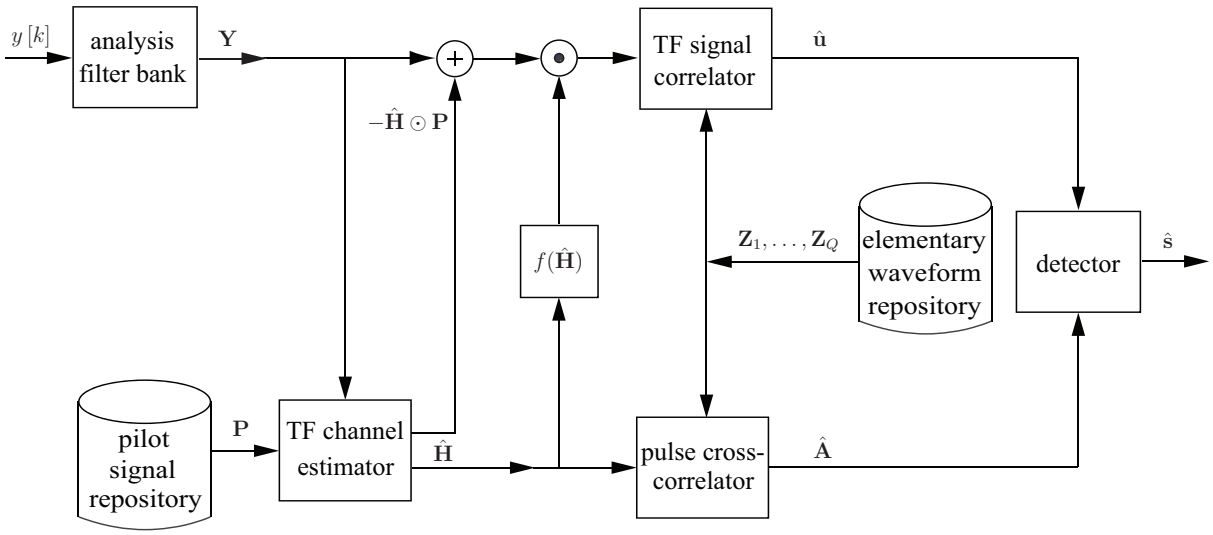

FIGURE 4.1: Reconfigurable baseband receiver architecture.

of size $K \times D$ which contains the channel parameter estimates. The channel parameters are defined in Sect. 3.3 as the channel gain values at the grid points in the TF plane, which correspond to samples of the time-variant channel transfer function. Moreover, the TF domain channel diagonalization enables relatively simple parameter estimation and demodulation schemes. The module of $f(\hat{\mathbf{H}})$ in the figure represents a function of the estimated channel parameter matrix $\hat{\mathbf{H}}$, which can be either $f(\hat{\mathbf{H}}) = \hat{\mathbf{H}}^*$ or $f(\hat{\mathbf{H}}) = \hat{\mathbf{H}}^+$, where $\hat{\mathbf{H}}^*$ denotes the matrix with every element being the complex conjugate of the corresponding element of $\hat{\mathbf{H}}$ and $\hat{\mathbf{H}}^+$ is defined as the result of element-wise inversion of $\hat{\mathbf{H}}$.

In the following, we will discuss the different functional blocks of the receiver architecture in detail. First, the blocks of the function $f(\hat{\mathbf{H}})$ and the calculation of the pulse cross-correlation matrix $\hat{\mathbf{A}}$ will be described for two different ways of demodulation, namely based on matched filtering in Sect. 4.1 or equalization in Sect. 4.2. Then, the channel estimation scheme will be discussed in Sect. 4.3 followed by the detector description in Sect. 4.4. A control scheme for setting up the overall receiver functionality is described in Sect. 4.5. Finally, in Sect. 4.6, the complexity of the receiver is analyzed in terms of the required numbers of complex multiplications and additions per detected symbol.

4.1 Matched Filtering Based Receiver Structure

Fig. 4.1 represents a reconfigurable receiver with signal demodulation based on matched filtering in case $f(\hat{\mathbf{H}}) = \hat{\mathbf{H}}^*$, where the pulse cross-correlation is computed as in Fig. 4.2. The pulse cross-correlator block, which will be described in detail subsequently, includes

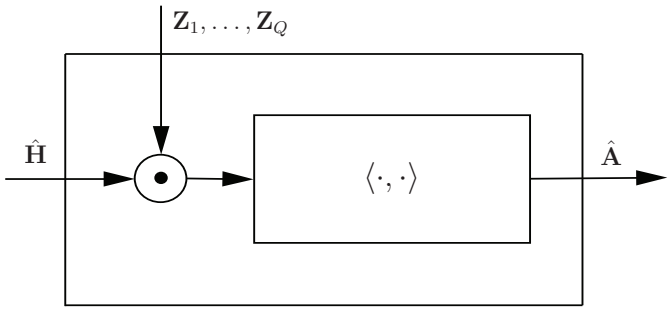

FIGURE 4.2: Pulse cross-correlation block of the matched filtering based receiver architecture.

an element-wise multiplication and an inner product operation, while TF representations $\mathbf{Z}_1, \ldots, \mathbf{Z}_Q$ of the elementary waveforms are provided by a local repository. To compute the TF representations $\mathbf{Z}_1, \ldots, \mathbf{Z}_Q$ of the elementary waveforms and $\mathbf{P}$ of the pilot signal, on-line computations are required for some scenarios, e.g., in UMTS systems where the elementary waveforms and the pilot signal are subject to time-variant signature spreading and scrambling operations. Based on the latter, the signals from different sources can be separated from each other at the receiver. Note that due to the time-variance of the elementary waveform spreading and the scrambling, it is not possible to pre-compute the corresponding TF coefficients. Hence, extra analysis FBs are required for the purpose of calculating the TF coefficients in real time. For other scenarios, e.g., OFDM systems, the TF coefficients can be pre-computed and obtained from local repositories.

Note that matched filtering of the information-bearing part $y[k] - (\mathcal{H}p)[k]$ of the received signal $y[k]$ against the Q distorted waveforms yields

$$u_q = \langle y - \mathcal{H}p, \mathcal{H}z_q \rangle, \quad q = 1, \ldots, Q. \tag{4.4}$$

The coefficients $u_1, \ldots, u_Q$ represent a sufficient statistics for the decoding problem under the assumption of $v[k]$ representing an additive white Gaussian noise (AWGN) process.

The receiver structure in Fig. 4.1 is based on the signal processing in the TF domain, and tight Gabor frames which fulfill Paseval's identity are used for signal analysis at the receiver. Therefore, according to (2.16), the estimated sufficient statistics (4.4) required by the subsequent detector can be computed in the TF domain as

$$\begin{aligned} \hat{u}_q &= \langle \mathbf{Y} - \hat{\mathbf{H}} \odot \mathbf{P}, \hat{\mathbf{H}} \odot \mathbf{Z}_q \rangle \qquad (4.5) \\ &= \sum_{i=1}^{K} \sum_{j=1}^{D} \left([\mathbf{Y}]_{i,j} - [\hat{\mathbf{H}}]_{i,j} [\mathbf{P}]_{i,j} \right) [\hat{\mathbf{H}}^*]_{i,j} [\mathbf{Z}_q^*]_{i,j} \\ &= \langle \hat{\mathbf{H}}^* \odot \left(\mathbf{Y} - \hat{\mathbf{H}} \odot \mathbf{P} \right), \mathbf{Z}_q \rangle, \qquad (4.6) \end{aligned}$$

where $[\mathbf{Y}]_{i,j}$, $[\hat{\mathbf{H}}^*]_{i,j}$, $[\mathbf{P}]_{i,j}$ and $[\mathbf{Z}_q^*]_{i,j}$ denote the ith element in the jth column of $\mathbf{Y}$, $\hat{\mathbf{H}}^*$, $\mathbf{P}$ and $\mathbf{Z}_q^*$, respectively. The qth elementary waveform and the pilot signal at the channel output in the TF domain are approximated as $\hat{\mathbf{H}} \odot \mathbf{Z}_q$ and $\hat{\mathbf{H}} \odot \mathbf{P}$, resp., employing the TF domain channel diagonalization. The receiver is designed to perform an element-wise multiplication of the estimated information-bearing part of the received signal by $\hat{\mathbf{H}}^*$, i.e., $\hat{\mathbf{H}}^* \odot \left(\mathbf{Y} - \hat{\mathbf{H}} \odot \mathbf{P} \right)$ in (4.6), rather than an element-wise multiplication of the elementary waveforms by $\hat{\mathbf{H}}$, i.e., $\hat{\mathbf{H}} \odot \mathbf{Z}_q$ as in (4.5). The reformulation of the sufficient statistics in such a way has two advantages. First, it reduces the complexity in some scenarios considerably. For instance, in the UMTS downlink, the multiplexing of various physical channels results in a large number of elementary waveforms, and the TF representation of each waveform at the channel output needs to be computed according to (4.5). By a rearrangement of the computation of the sufficient statistics in (4.6), the element-wise multiplication of a large number of elementary waveforms in the TF domain can be avoided. Secondly, it facilitates a common receiver architecture of a matched filtering based receiver and an equalization based receiver.

From (4.1) and (4.2), the received signal reads

$$y[k] = \left(\mathcal{H} \left(\sum_{q=1}^{Q} s_q z_q + p \right) \right) [k] + v[k]. \qquad (4.7)$$

By inserting (4.7) in (4.4), the vector $\mathbf{u}$ comprising $u_1, \ldots, u_Q$ as components can be expressed as

$$\mathbf{u} = \mathbf{A}\mathbf{s} + \mathbf{v}, \tag{4.8}$$

where the vector $\mathbf{s}$ comprising the signals $s_1, \ldots, s_Q$ represents the transmitted codeword, and the matrix $\mathbf{A}$ denotes the pulse cross-correlation matrix. The noise vector $\mathbf{v}$ contains the terms $\langle v, \mathcal{H}z_1\rangle, \ldots, \langle v, \mathcal{H}z_Q\rangle$, which are the correlations of the noise signal with all possible waveforms, and consequently the noise is not white any more. The jth element of the ith row of the $Q \times Q$ matrix $\mathbf{A}$ is given as

$$[\mathbf{A}]_{i,j} = \langle \mathcal{H}z_j, \mathcal{H}z_i\rangle, \quad i, j \in \{1, \ldots, Q\}. \tag{4.9}$$

The diagonal of the matrix $\mathbf{A}$ contains the energies of the waveforms $(\mathcal{H}z_1)[k], \ldots, (\mathcal{H}z_Q)[k]$ at the channel output, whereas the off-diagonal values in $\mathbf{A}$ contain the waveform cross-correlations. Furthermore, $E\left[\mathbf{v}\mathbf{v}^{\mathrm{H}}\right] = N_0\mathbf{A}$, where N_0 denotes the spectral power density of $v[k]$.

A baseband receiver may first compute the sufficient statistics $\mathbf{u}$ and pulse cross-correlation matrix $\mathbf{A}$, and then perform demodulation and decoding on the basis of (4.8). As shown in Fig. 4.1, the receiver calculates the estimates $\left(\hat{\mathbf{u}}, \hat{\mathbf{A}}\right)$ of $(\mathbf{u}, \mathbf{A})$, based on the channel parameter estimates $\hat{\mathbf{H}}$. In (4.5) the elements of $\hat{\mathbf{u}}$ are computed in the TF domain, and the elements of $\hat{\mathbf{A}}$ are computed in the TF domain as

$$[\hat{\mathbf{A}}]_{i,j} = \langle \hat{\mathbf{H}} \odot \mathbf{Z}_j, \hat{\mathbf{H}} \odot \mathbf{Z}_i\rangle \quad i, j \in \{1, \ldots, Q\}. \tag{4.10}$$

Fig. 4.2 shows the calculation of the pulse cross-correlations (4.10). As shown in the figure, the TF representation of the transmit side elementary waveforms $\mathbf{Z}_1, \ldots, \mathbf{Z}_Q$ are mapped to the TF representations of the waveforms at the channel output, i.e., $(\hat{\mathbf{H}} \odot \mathbf{Z}_1), \ldots, (\hat{\mathbf{H}} \odot \mathbf{Z}_Q)$, by an element-wise multiplication. This simple operation results from the TF domain channel diagonalization (3.14) discussed in Sect. 3.3. Then the pulse cross-correlation matrix $\hat{\mathbf{A}}$ is computed by the inner product operation between all the distorted elementary waveforms in the TF domain according to (4.10).

The TF representation of the baseband signal at the receiver $y[k]$ can be written for perfectly known channel coefficients $\mathbf{H}$ as

$$\mathbf{Y} = \mathbf{H} \odot \left(\sum_{q=1}^{Q} s_q \mathbf{Z}_q + \mathbf{P} \right) + \mathbf{W}. \tag{4.11}$$

Since, in general, representing the channel output using the proposed TF channel diagonalization is only an approximation, the matrix $\mathbf{W}$ in (4.11) represents the inherent error from the channel diagonalization together with the TF representation $\mathbf{V}$ of the noise $v[k]$, i.e., $\mathbf{W} = \mathbf{V} - \mathbf{E}$. The TF domain error from the channel diagonalization is expressed as

$$\mathbf{E} = \mathbf{H} \odot \left(\sum_{q=1}^{Q} s_q \mathbf{Z}_q + \mathbf{P} \right) - \mathcal{G}\left(\mathcal{H}\left(\sum_{q=1}^{Q} s_q z_q + p \right) \right), \tag{4.12}$$

with the channel input signal $\sum_{q=1}^{Q} s_q z_q + p$ instead of x_Q in Fig. 3.3, which is in line with (3.19). In the following, we treat the model error as a part of the noise, and refer to $\mathbf{W}$ as the TF representation of the noise signal.

4.2 Equalizer Based Receiver Structure

If we choose the function block $f(\hat{\mathbf{H}}) = \hat{\mathbf{H}}^{+}$ and the pulse cross-correlation depicted in Fig. 4.3, Fig. 4.1 shows a baseband receiver architecture based on the TF domain equalization. Note that the pulse cross-correlator in Fig. 4.3 does not use the estimated

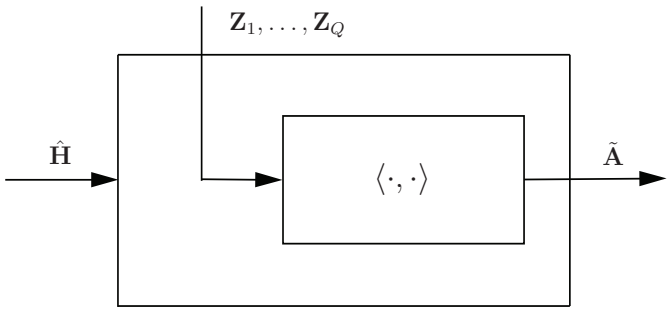

FIGURE 4.3: Pulse cross-correlation block of the equalizer based receiver architecture.

channel coefficients $\hat{\mathbf{H}}$, since the signal at the TF signal correlator input is assumed

perfectly equalized corresponding to $H[\ell, m] = 1 \; \forall (\ell, m) \in \Lambda$, so that a premultiplication of $\mathbf{Z}_q$ in Fig. 4.3 can be saved. In Fig. 4.1, the equalization is carried out in the TF domain by an element-wise multiplication of the TF representation of the information-bearing part $\mathbf{Y} - \hat{\mathbf{H}} \odot \mathbf{P}$ of the received signal with the inverse of the individual channel coefficients $\hat{\mathbf{H}}^{+}$. The resulting signal in the TF domain reads $\hat{\mathbf{H}}^{+} \odot \left(\mathbf{Y} - \hat{\mathbf{H}} \odot \mathbf{P} \right)$. As shown in Fig. 4.3, the pulse cross-correlations are computed by the inner product operation between all of the elementary waveforms. Therefore, the jth element of the ith row of the pulse cross-correlations matrix $\tilde{\mathbf{A}}$ is given by

$$[\tilde{\mathbf{A}}]_{i,j} = \langle \mathbf{Z}_j, \mathbf{Z}_i \rangle \quad i, j \in \{1, \ldots, Q\}. \tag{4.13}$$

The correlations of the equalized signal with the elementary waveforms $z_1[k], \ldots, z_Q[k]$ are also computed in the TF domain, which yields

$$\tilde{u}_q = \left\langle \hat{\mathbf{H}}^{+} \odot \left(\mathbf{Y} - \hat{\mathbf{H}} \odot \mathbf{P} \right), \mathbf{Z}_q \right\rangle. \tag{4.14}$$

Assume the vector $\tilde{\mathbf{u}}$ comprises the elements $\tilde{u}_1, \ldots, \tilde{u}_Q$. In analogy with (4.8), the vector $\tilde{\mathbf{u}}$ can be expressed as

$$\tilde{\mathbf{u}} = \tilde{\mathbf{A}}\mathbf{s} + \tilde{\mathbf{v}}, \tag{4.15}$$

where the elements of the vector $\tilde{\mathbf{v}}$ are given by

$$[\tilde{\mathbf{v}}]_j = \left\langle \hat{\mathbf{H}}^{+} \odot \mathbf{W}, \mathbf{Z}_j \right\rangle. \tag{4.16}$$

Subsequently, demodulation and decoding are carried out based on $\tilde{\mathbf{u}}$ and the pulse cross-correlation matrix $\tilde{\mathbf{A}}$. However, when the estimated channel gain $\hat{\mathbf{H}}$ is small in certain TF locations, the noise is amplified.

An equalizer based receiver is a favorable choice for certain system scenarios such as in the UMTS downlink. In this case, the transmit signal comprises signals to be used commonly by all users, like e.g. pilot signals, as well as signals dedicated to the individual users. As mentioned above, the signals belonging to the various so-called physical channels are encoded by different spreading codes and additionally scrambled, where only the desired

user is able to correlate and decode the corresponding signal. The signals of the other users are regarded as interferences to the desired signal for a certain user. However, since the signals for all users are distorted by a common channel in the downlink, the orthogonality of signals associated with different users can be restored by channel equalization. Thus, the channel equalization option is more suitable in this scenario than matched filtering.

4.3 Channel Estimation

It has been shown that the choice of the receiver architecture translates to a corresponding choice of $f(\hat{\mathbf{H}})$ and pulse cross-correlation according to Sect. 4.1 and Sect. 4.2. In this section, the TF domain channel estimation will be discussed. The aforementioned estimate $\hat{\mathbf{H}}$ of the channel coefficients is provided by a channel estimator, which operates in the TF domain and takes as input the observation $\mathbf{Y}$ and a locally reproduced pilot signal representation $\mathbf{P}$ in a similar manner as channel estimators in OFDM receivers.

The channel estimator in Fig. 4.1 provides estimates of the sampled version $\mathbf{H}$ of the time-variant transfer function. Only non-blind parameter estimation is considered in the receiver since the common standards indeed include pilot signals for the purpose of channel estimation. The transmitted signal is assumed to contain both an information signal and a pilot signal $p[k]$ being known at the receiver. The embedding of $p[k]$ in the transmit signal (4.1) is arbitrary. The pilot signal may precede the information signal (as a preamble) or it may be superimposed to the information signal, as in the case of CDMA systems with a common pilot channel. Rather than knowing the pilot signal in the time domain, the receiver shall have knowledge of the TF coefficients $\mathbf{P}$ of the pilot signal.

We consider the case of a pilot signal superimposed to the Q information signals in (4.1). With the discussed channel diagonalization, the output of the analysis FB in Fig. 4.1 can be written as in (4.11). Note that the channel gains $[\mathbf{H}]_{i,j}$ and $[\mathbf{H}]_{i',j'}$ belonging to nearby TF slots (i, j) and (i', j'), resp., are highly correlated if $\left|i - i'\right| NT_{\mathrm{s}}$ is much smaller than the coherence time of the channel and $\left|j - j'\right| / (KT_{\mathrm{s}})$ is much smaller than the coherence bandwidth of the channel. Pilot aided channel estimation in OFDM systems usually has

two steps. In the first step, the initial estimate $[\breve{\mathbf{H}}]_{i,j}$ of the channel parameter is obtained by dividing the received signal $\mathbf{Y}$ element-wise by the transmitted pilot signal $\mathbf{P}$ in the TF domain, i.e.,

$$\begin{aligned} \breve{\mathbf{H}} &= \mathbf{Y} \odot \mathbf{P}^{+} && (4.17) \\ &= \mathbf{H} + \mathbf{H} \odot \left(\sum_{q=1}^{Q} s_q \mathbf{Z}_q \right) \odot \mathbf{P}^{+} + \mathbf{W} \odot \mathbf{P}^{+}, && (4.18) \end{aligned}$$

where (4.18) is obtained from (4.17) by applying (4.11).

In the second step, the final estimates $[\hat{\mathbf{H}}]_{i,j}$ of the channel parameter are attained from $[\breve{\mathbf{H}}]_{i,j}$ by a two-dimensional interpolation or filtering. The two-dimensional filtering has the form

$$[\hat{\mathbf{H}}]_{i,j} = \sum_{i'=1}^{K} \sum_{j'=1}^{D} q(i,j,i',j')[\breve{\mathbf{H}}]_{i',j'}. \tag{4.19}$$

The estimates interpolated over the entire TF grid in such a way form a two-dimensional Wiener filtering [70]. The choice of the two-dimensional estimation window $q(i,j,i',j')$ depends on the cross-correlations of the channel parameters and thus on delay and Doppler spreads. Smaller Doppler spreads suggest the inclusion of a larger number of samples in the time dimension, while smaller delay spreads suggest the inclusion of a larger number of samples in the frequency dimension for the estimation of $[\mathbf{H}]_{i,j}$. In general, the channel estimator needs knowledge of the TF representation of the pilot signal and additionally the information of the delay and Doppler spreads in order to compute the estimation window.

Efficient TF channel parameter estimators operating on the basis of (4.11) for doubly dispersive channels are presented in [61]. Upon stacking the TF coefficients of the received signal, the pilot signal, the information signal and the noise into corresponding vectors, the two-dimensional estimation problem can be translated into a one-dimensional problem. This leads to a reformulation of (4.11) according to

$$\mathrm{st}\left[\mathbf{Y}\right] = \mathrm{st}\left[\mathbf{H}\right]\left(\mathrm{Diag}\left[\mathrm{st}\left[\mathbf{S}\right]\right] + \mathrm{Diag}\left[\mathrm{st}\left[\mathbf{P}\right]\right]\right) + \mathrm{st}\left[\mathbf{W}\right], \tag{4.20}$$

where $\mathbf{S} = \sum_{q=1}^{Q} s_q \mathbf{Z}_q$.

Assume that $\mathrm{st}[\mathbf{S}]$ represents a white random process with $E[\mathrm{st}[\mathbf{S}]] = 0$, and $E\left[\mathrm{st}[\mathbf{S}](\mathrm{st}[\mathbf{S}])^{\mathrm{H}}\right] = \epsilon_s \mathbf{I}_{DK}$. The noise $\mathrm{st}[\mathbf{W}]$ is also white, i.e., $E[\mathrm{st}[\mathbf{W}]] = 0$ and $E\left[\mathrm{st}[\mathbf{W}](\mathrm{st}[\mathbf{W}])^{\mathrm{H}}\right] = \epsilon_w \mathbf{I}_{DK}$. The information signal $\mathrm{st}[\mathbf{S}]$, the noise signal $\mathrm{st}[\mathbf{W}]$, and the channel $\mathrm{st}[\mathbf{H}]$ are further assumed to be mutually independent random vectors. The linear minimum mean-squared error (LMMSE) estimate of $\mathrm{st}[\mathbf{H}]$ can be expressed as

$$\mathrm{st}\left[\hat{\mathbf{H}}_{\mathrm{LMMSE}}\right] = \mathbf{R}_h \left(\left(\mathbf{B}^{\mathrm{H}}\mathbf{B}\right)\mathbf{R}_h + \left(\epsilon_s + \epsilon_w\right)\mathbf{I}_{DK}\right)^{-1} \mathbf{B}^{\mathrm{H}}\mathrm{st}[\mathbf{Y}], \tag{4.21}$$

where $\mathbf{B} = \mathrm{Diag}[\mathrm{st}[\mathbf{P}]]$. The covariance matrix is defined as $\mathbf{R}_h = E\left[\mathrm{st}[\mathbf{H}](\mathrm{st}[\mathbf{H}])^{\mathrm{H}}\right]$, which depends on the environment and can be computed from the delay and Doppler power spectra.

By replacing $\mathbf{B}^{\mathrm{H}}\mathbf{B}$ by $\epsilon_p \mathbf{I}_{DK}$, where ϵ_p denotes the mean pilot energy per TF slot, we obtain the modified LMMSE (MLMMSE) estimate

$$\mathrm{st}\left[\hat{\mathbf{H}}_{\mathrm{MLMMSE}}\right] = \mathbf{R}_h \left(\epsilon_p \mathbf{R}_h + \left(\epsilon_s + \epsilon_w\right)\mathbf{I}_{DK}\right)^{-1} \mathbf{B}^{\mathrm{H}}\mathrm{st}[\mathbf{Y}]. \tag{4.22}$$

However, the computational complexity of the estimator is very high due to the large matrix dimensions. For WSSUS channels with a separable scattering function, the covariance matrix $\mathbf{R}_h$ can be written as

$$\mathbf{R}_h = \mathbf{R}_{\mathrm{t}} \otimes \mathbf{R}_{\mathrm{f}}, \tag{4.23}$$

where $\mathbf{R}_{\mathrm{t}}$ represents the $D \times D$ covariance matrix defined by $[\mathbf{R}_{\mathrm{t}}]_{i,j} = \phi_{\mathrm{t}}[(i-j)N]$, $\mathbf{R}_{\mathrm{f}}$ represents the $K \times K$ covariance matrix defined by $[\mathbf{R}_{\mathrm{f}}]_{i,j} = \phi_{\mathrm{f}}\left[\frac{2\pi(i-j)}{K}\right]$, and $\otimes$ denotes the Kronecker product [67]. The time correlation function ϕ_{t} and the frequency correlation function ϕ_{f} have been defined in Sect. 3.2.

Let $\mathbf{R}_{\mathrm{t}} = \mathbf{U}_{\mathrm{t}}\mathbf{\Xi}_{\mathrm{t}}\mathbf{U}_{\mathrm{t}}^{\mathrm{H}}$ and

$$\mathbf{R}_{\mathrm{f}} = \mathbf{U}_{\mathrm{f}}\mathbf{\Xi}_{\mathrm{f}}\mathbf{U}_{\mathrm{f}}^{\mathrm{H}} \tag{4.24}$$

represent the singular value decompositions of the two Hermitian covariance matrices [71]. The matrices $\mathbf{U}_{\mathrm{t}}$ and $\mathbf{U}_{\mathrm{f}}$ are unitary and $\mathbf{\Xi}_{\mathrm{t}}$ and $\mathbf{\Xi}_{\mathrm{f}}$ are diagonal matrices with real non-negative diagonal elements. Using some properties of the Kronecker product [67], the

MLMMSE estimate in (4.22) can be further written as

$$\hat{\mathbf{H}}_{\mathrm{MLMMSE}} = \mathbf{U}_{\mathrm{f}} \left(\mathbf{C} \odot \left(\mathbf{U}_{\mathrm{f}}^{\mathrm{H}} \left(\mathbf{Y} \odot \mathbf{P}^{*} \right) \mathbf{U}_{\mathrm{t}}^{*} \right) \right) \mathbf{U}_{\mathrm{t}}^{\mathrm{T}}, \tag{4.25}$$

with the $K \times D$ matrix $\mathbf{C}$ defined by $\mathrm{st}\left[\mathbf{C}\right] = \mathrm{diag}\left[\boldsymbol{\Xi}_{\mathrm{h}}\right]$, where

$$\boldsymbol{\Xi}_{\mathrm{h}} \triangleq \left(\boldsymbol{\Xi}_{\mathrm{t}} \otimes \boldsymbol{\Xi}_{\mathrm{f}} \right) \left(\epsilon_p \left(\boldsymbol{\Xi}_{\mathrm{t}} \otimes \boldsymbol{\Xi}_{\mathrm{f}} \right) + \left(\epsilon_s + \epsilon_w \right) \mathbf{I}_{DK} \right)^{-1}. \tag{4.26}$$

The simplified estimator (4.25) has a lower computational complexity. Moreover, the complexity can be further reduced with low-rank approximation of the covariance matrices $\mathbf{R}_{\mathrm{t}}$ and $\mathbf{R}_{\mathrm{f}}$ by neglecting the diagonal elements of $\boldsymbol{\Xi}_{\mathrm{t}}$ and $\boldsymbol{\Xi}_{\mathrm{f}}$ which are below a certain threshold value.

When the symbol duration of the signal is much smaller than the channel coherence time, the channel can be regarded purely frequency-selective. In this case, the channel parameters are constant in the time dimension, i.e., $[\mathbf{H}]_{i,1} = [\mathbf{H}]_{i,2} = \ldots = [\mathbf{H}]_{i,j} = [\mathbf{h}]_i$, which simplifies their estimation. Here, $\mathbf{h}$ is the column vector whose ith component is given by $[\mathbf{h}]_i$ which, in turn, represents the channel gain in the ith sub-band. According to (4.24), (4.25) and (4.26) the MLMMSE estimate of $\mathbf{h}$ is given by

$$\hat{\mathbf{h}}_{\mathrm{MLMMSE}} = \mathbf{R}_{\mathrm{f}} \left(\mathbf{R}_{\mathrm{f}} + D^{-1} \left(\frac{\epsilon_s}{\epsilon_p} + \frac{\epsilon_w}{\epsilon_p} \right) \mathbf{I}_K \right)^{-1} D^{-1} \epsilon_p^{-1} \left(\mathbf{Y} \odot \mathbf{P}^{*} \right) \mathbf{1}, \tag{4.27}$$

where $\mathbf{1}$ is a vector of size D with all elements being one.

4.4 Detector

In the following, different detection methods for the matched filtering based receiver architecture are discussed. Given the estimated sufficient statistics $\hat{\mathbf{u}}$, the pulse cross-correlation matrix $\hat{\mathbf{A}}$ and the codebook Ω, different standard decoding methods are available on the basis of (4.8). Options for the estimation of the codeword $\mathbf{s} \in \Omega$ include

- the maximum-likelihood (ML) estimate given as $\hat{\mathbf{s}}_{\mathrm{ML}} = \arg\min_{\mathbf{s}\in\Omega} \mathbf{s}^{\mathrm{H}} \hat{\mathbf{A}} \mathbf{s} - 2\Re(\hat{\mathbf{u}}^{\mathrm{H}} \mathbf{s})$,

- the zero-forcing (ZF) based estimate given as $\hat{\mathbf{s}}_{\mathrm{ZF}} = \mathcal{D}(\hat{\mathbf{A}}^{-1}\hat{\mathbf{u}})$ with $\mathcal{D} : \mathbb{C}^Q \rightarrow \Omega$ a certain detection rule,
- the LMMSE based estimate given as $\hat{\mathbf{s}}_{\mathrm{LMMSE}} = \mathcal{D}((\hat{\mathbf{A}} + \gamma^{-1}\mathbf{I}_Q)^{-1}\hat{\mathbf{u}})$,

with γ denoting the ratio of the mean energy of the signals $s_1, \ldots, s_Q$ over N_0.

For the ZF approach, the multiplication of $\hat{\mathbf{u}}$ by $\hat{\mathbf{A}}^{-1}$ yields

$$\hat{\mathbf{s}}_{\mathrm{ZF}} = \hat{\mathbf{A}}^{-1}\hat{\mathbf{u}} = \mathbf{s} + \hat{\mathbf{A}}^{-1}\mathbf{v}. \tag{4.28}$$

The multiplication with the inverse of $\hat{\mathbf{A}}$ can be efficiently implemented using iterative methods like the Gauss-Seidel iteration [67]. The demodulation and decoding procedure based on the resulting $\hat{\mathbf{s}}_{\mathrm{ZF}}$ may first calculate the log-likelihood ratios for all bits encoded in the symbols in $\hat{\mathbf{s}}_{\mathrm{ZF}}$, using $[\hat{\mathbf{A}}]_{i,i}^{-1} N_0$ as the estimate for the ith noise variance, and then perform soft-decision decoding.

When the ZF approach is applied to the equalizer based receiver architecture, the output of the TF signal correlator $\tilde{\mathbf{u}}$ is multiplied by $\tilde{\mathbf{A}}^{-1}$, i.e.,

$$\tilde{\mathbf{s}}_{\mathrm{ZF}} = \tilde{\mathbf{A}}^{-1}\tilde{\mathbf{u}} = \mathbf{s} + \tilde{\mathbf{A}}^{-1}\tilde{\mathbf{v}}. \tag{4.29}$$

It turns out that the statistics of the noise terms resulting from ZF in a matched filtering based receiver and from ZF in an equalizer based receiver are identical, i.e., $E\left[\hat{\mathbf{A}}^{-1}\mathbf{v}\mathbf{v}^{\mathrm{H}}\hat{\mathbf{A}}^{\mathrm{H}^{-1}}\right] = E\left[\tilde{\mathbf{A}}^{-1}\tilde{\mathbf{v}}\tilde{\mathbf{v}}^{\mathrm{H}}\tilde{\mathbf{A}}^{\mathrm{H}^{-1}}\right]$. A detailed proof is shown in Appendix C. However, if the transmitted signal includes orthogonal signal components destined for other users, in the case of an equalization the orthogonality is preserved and the vector $\tilde{\mathbf{u}}$ does thus not contain multiple access interference (MAI). In contrast, in the case of a matched filtering based receiver, the output of the TF signal correlator $\hat{\mathbf{u}}$, in general, does contain MAI. Therefore, if the performance of the matched filtering based receiver is interference-limited, the equalizer based receiver can be used to overcome the interference limitation.

4.5 Parametric Control

Since the operation of the various receiver entities in Fig. 4.1 is defined by the signal format at hand, they can be implemented in the form of a reconfigurable hardware, being controlled by a limited number of parameters. For example, parameters for describing analysis FB configurations are required, including the down-sampling factor, the number of sub-bands, and the window function related to the impulse response of the prototype filters, which can be optimized for different channel conditions. Further parameters may be used for specifying the signal subsets for the two repositories, providing the channel statistics for the window optimization and defining the signal mapping schemes and decoding methods.

Tab. 4.1 shows the control parameters for the reconfigurable receiver with the possible values for each parameter and a short description explaining the used parameter acronyms. The baseband receiver architecture can be configured to a matched filtering based receiver or an equalizer based receiver by choosing different parameters for the block $f(\hat{\mathbf{H}})$, and both types are flexible to handle signal formats of various air interfaces. The analysis FB is configured by the window function $g[k]$, the down-sampling factor N, and the number of sub-bands K. Two repositories contain the TF representations of the elementary waveforms and the pilot signals for all possible modes. An exception are modes where the transmit signals are subject to scrambling in the form of a multiplication by a PN sequence. In this case the repositories need to replicate the scrambling operations, hence, the TF representations of the elementary waveforms and pilot signals need to be computed on-line. For the channel estimation the RMS delay and Doppler spreads of the channel are required, as well as for obtaining the optimized window. The channel estimation schemes discussed in Sect. 4.3 for both time-invariant and time-variant channels can be employed. The mapping scheme of the transmitted signal is required by the receiver and therefore shown in the table. There is also a parameter describing the detection method which can be chosen from the three discussed methods in Sect. 4.4.

parameter	parameter set	description
ROM	{1,2}	receiver operation mode ROM =1: matched filtering ($f(\hat{\mathbf{H}}) = \hat{\mathbf{H}}^*$) ROM =2: equalization ($f(\hat{\mathbf{H}}) = \hat{\mathbf{H}}^+$)
$g[k]$	$\mathbb{R}^T$	window function
N	$\mathbb{N}$	down-sampling factor of the analysis FB
K	$\mathbb{N}$	number of sub-bands of the analysis FB
EWR	{1,2}	TF elementary waveform representation EWR=1: pre-compute EWR=2: on-line compute
PR	{1,2}	pilot signal representation PR=1: pre-compute PR=2: on-line compute
CEM	{1,2}	channel estimation method CEM=1: channel estimation for time-invariant channel CEM=2: channel estimation for time-variant channel
τ_{RMS}	$\mathbb{R}_+$	RMS delay spreads in samples
ν_{RMS}	$\mathbb{R}_+$	RMS Doppler spreads in samples
MAP	{BPSK, QPSK, 16-QAM, 64-QAM}	bit-to-signal mapping scheme
DEC	{ZF, LMMSE, ML}	decoding method

TABLE 4.1: Parameters for baseband receiver control.

4.6 Complexity

In this section the complexity of the reconfigurable baseband receiver in Fig. 4.1 is investigated. The complexities of the various functional blocks, such as the analysis FB for computing the TF representation of the received signal, channel estimation, TF domain correlation, and signal detection are assessed in terms of complex multiplications (CMs) and complex additions (CAs). Since on-line computations for TF representations of the elementary waveforms and the pilot signal are only necessary for UMTS signals, we discuss their complexity in the next chapter. Moreover, the complexity of the waveform cross-correlation block is also not included in this section since it crucially depends on the signal format, so that we discuss it later using a UMTS downlink signal as an example.

4.6.1 TF Representation of the Received Signal

The TF coefficients $\mathbf{Y}$ are computed by means of an analysis FB from the received signal $y[k]$ in the baseband. The FB is implemented as a uniform DFT FB [13] based on the time-discrete window $g[k]$ with a length of T samples. A DFT FB includes a polyphase filtering and a K-point FFT, and yields sequences of K-dimensional vectors, one vector per time slot. The computational complexity of the DFT FB per output vector is as follows:

- The K-point FFT requires no more than $(K/2)\log_2 K$ CMs and $K\log_2 K$ CAs if K is a power of 2.
- The polyphase filtering requires no more than T CMs and $T-K$ CAs.

Thus, for computing the TF coefficients describing the received signal,

$$((K/2)\log_2 K + T)\,\text{CMs} \;\text{ and }\; (K\log_2 K + T - K)\,\text{CAs} \tag{4.30}$$

per FB output vector are required.

4.6.2 Channel Estimation

The receiver calculates the channel parameter estimates by means of the TF representation of the known pilot signal. As in (4.25), the unitary matrices $\mathbf{U}_\mathrm{t}$, $\mathbf{U}_\mathrm{f}$, and $\mathbf{C}$ are determined by the channel covariance matrix $\mathbf{R}_h$, and they can be computed off-line. The estimated channel parameters computed on-line from the analysis FB output $\mathbf{Y}$ via (4.25) involves four matrix multiplications and two element-wise multiplications. Thus, the number of CMs is $2DK(D+K+1)$ per TF coefficient, and the number of CAs is $2DK(D+K-1)$ per TF coefficient, where $D = \left\lceil \frac{T_\mathrm{r}}{N} \right\rceil$ with T_r denoting the length of the received signal.

Note that the computational complexity can be further reduced by reducing the rank of the covariance matrices $\mathbf{R}_\mathrm{t}$ and $\mathbf{R}_\mathrm{f}$ to D_0 and K_0, resp, where $D_0 \leq D$ and $K_0 \leq K$. As a

result of the reduced matrix dimensions, the computation of the channel estimates requires only $D_0K_0(D+K+1)+DK(D_0+K_0+1)$ CMs, and $D_0K_0(D+K-1)+DK(D_0+K_0-1)$ CAs, or approximately

$$(D_0 + K_0 + 1)\,\text{CMs} \;\text{ and }\; (D_0 + K_0 - 1)\,\text{CAs} \tag{4.31}$$

per channel coefficient if D_0 and K_0 are relatively small numbers.

4.6.3 TF Domain Correlation

For the matched filtering based receiver, the correlation of $y[k]$ with $(\mathcal{H}z_q)[k]$ in the TF domain involves an element-wise multiplication of $\hat{\mathbf{H}}^*$, $\mathbf{Y}$ and $\mathbf{Z}_q$ and a summation. This requires

$$\left(2\left\lceil\frac{T_\mathrm{r}}{N}\right\rceil K\right)\text{CMs} \;\text{ and }\; \left(\left\lceil\frac{T_\mathrm{r}}{N}\right\rceil K-1\right)\text{CAs} \tag{4.32}$$

per symbol. For the equalizer based receiver, the TF domain correlator performs an element-wise multiplication of $\hat{\mathbf{H}}^+$, $\mathbf{Y}$ and $\mathbf{Z}_q$ and a summation. The number of the operations is the same as in (4.32).

4.6.4 Detection

For analyzing the computational complexity of the detector, we consider the ZF approach as an example. As shown in (4.28), a matrix inversion is required followed by a matrix multiplication. For the matched filtering based receiver, the inversion of the matrix $\hat{\mathbf{A}}$ of dimension $Q \times Q$ has a complexity $O(Q^3)$ using, for example, Gauss-Jordan elimination methods. In contrast, for the equalization based receiver, the matrix $\tilde{\mathbf{A}}$ is often a diagonal matrix, in which case inversion requires only Q multiplications.

Chapter 5

Application of Flexible Radios

The matched filtering/equalizer based baseband receiver architecture discussed in Chap. 4 can principally be applied to all burst types featuring linear modulation and pilot/preamble signals. In the following, receiver configurations for OFDM and DSSS signals are investigated. Other forms of single-carrier and multi-carrier signals can be handled in similar ways. Through linearization even some nonlinear modulation schemes – such as Gaussian-filtered minimum shift keying adopted in the GSM standard – can be dealt with [72], but elaborating on this issue is beyond the scope of this thesis.

The proposed receiver architecture in Chap. 4 can easily be configured to a conventional OFDM receiver, as shown in Sect. 5.1.1. It is clear that the performance is expected to be similar to the conventional OFDM receiver, and thus this issue is not discussed in this chapter. Rather, we will focus on the receiver configuration for the UMTS downlink with wide-band CDMA (WCDMA). The corresponding performance is studied on different levels, from the inner receiver performance with perfect and imperfect channel estimation to the link level performance. Moreover, the computational complexity of the matched filtering/equalizer based receiver is discussed for UMTS signals. Finally, some issues related to reconfigurable receiver design, which were investigated within the framework of the IST project URANUS, are addressed.

5.1 Legacy Systems

5.1.1 OFDM-Based Air Interfaces

In an OFDM system, the input data stream is divided into several parallel sub-streams of reduced data rate and each sub-stream is modulated and transmitted on a separate orthogonal sub-carrier. The increased symbol duration due to the reduced data rate and the introduction of the CP, which is typically a repetition of the last samples of data portion of the block prepended to the data payload, improve the robustness of OFDM signals against the frequency-selective fading of multipath channels in wireless communications [73]. The inter-symbol-interference (ISI) can be eliminated as long as the CP duration is longer than the channel delay spread. Furthermore, OFDM systems exploit the frequency diversity of multipath channels by coding and interleaving the information across the sub-carriers prior to transmissions. As a spectrum efficient multiplexing technique which is capable of achieving high data rates, OFDM has been adopted in standards as: IEEE802.11a, WLAN, DVB-T and IEEE 802.16 WiMAX.

The reconfigurable receiver architecture in Fig. 4.1 can easily be configured to emulate a conventional OFDM receiver by properly chosen control parameters as shown in Tab. 5.1. The down-sampling factor N and the number of sub-bands K of the FB are chosen in

parameter	parameter value
ROM	1
$g[k]$	$g[k] = \begin{cases} 1 & \text{for } k = 0, \ldots, K-1 \\ 0 & \text{otherwise} \end{cases}$
N	OFDM symbol length
K	the number of sub-carriers
EWR	1
PR	1
CEM	1
τ_{RMS}	$\mathbb{R}_+$
ν_{RMS}	approximately zero
MAP	QPSK, 16-QAM, 64-QAM
DEC	ZF, MMSE

Table 5.1: Parameters for baseband receiver control for OFDM signals.

line with the OFDM symbol length and the number of sub-carriers, respectively. Here, we have $N > K$. The window function $g[k]$ of the analysis FB has a rectangular shape with length K, while the length of the CP equals $T_g = N - K$. The CP is inserted at the beginning of each OFDM symbol in the transmitter. By choosing a window having a rectangular shape with length K in the receiver, the FB operations are reduced to plain FFT/IFFT operations and the CPs are eliminated before the further signal processing. In this configuration, because of $N > K$, (2.1) does not represent a Gabor frame but rather a Gabor system with undercritical sampling. This has to do with the fact that the receiver disregards the signal parts in the CP. Moreover, the elementary waveforms are orthogonal to each other, and their TF representations $\mathbf{Z}_1, \ldots, \mathbf{Z}_Q$ as well as the TF representation of the pilot signal $\mathbf{P}$ can be pre-computed and read from the local repositories. The channel is usually regarded as static during the transmission of at least one OFDM symbol. In indoor scenarios as encountered in indoor WLANs the channel is even considered quasi-stationary during a whole data packet period [30].

In this configuration, the time-discrete signal analysis corresponds to block-wise performed DFTs. Perfect timing recovery is assumed, i.e., the system clock at the receiver is synchronized with that at the transmitter taking into account the delay associated with signal propagation. We further assume that the channel has a negligible Doppler dispersion and the delays of the essential signal parts do not exceed the length of the CP, such that an elementary waveform at the channel output, e.g., $(\mathcal{H}z_q)[k]$, is perfectly represented as $\mathbf{H} \odot \mathbf{Z}_q$. The cross-correlation matrix $\mathbf{A}$ has the form of a diagonal matrix due to the orthogonality between the elementary waveforms. The error-rate performance of this receiver mode matches the performance of conventional OFDM receivers. Furthermore, the channel estimator presented in Chap. 4.3 reduces to an OFDM channel estimator taking the second-order channel statistics into account, the performance of which is investigated in [70].

5.1.2 DSSS-Based Air Interfaces

In DSSS signalling, the data signal is spread over a much wider frequency band than required [74]. Due to the multiplication of the user data signal with a PN sequence, the

resulting DSSS signal appears similar to random noise to receivers having no knowledge of the used PN sequence [28]. The PN sequence is also called a spreading sequence and represents a user signature. The spreading sequence is composed of chips of duration T_{chip}. One of the most important parameters of a DSSS system is the *spreading factor* S_F denoting the ratio of the chip rate and the data rate. The frequency diversity inherent in spread spectrum signals makes them robust to fading from multipath propagation and also to narrow-band interference. In wireless communications there are a number of air interfaces adopting DSSS signaling, such as WLANs, UMTS or Bluetooth.

Tab. 5.2 shows the control parameters for a DSSS compliant mode, which are used below for the inner receiver performance evaluation. Unlike the configuration for OFDM

parameter	parameter description
ROM	1
$g[k]$	optimized window
N	96
K	128
EWR	2
PR	2
CEM	2
τ_{RMS}	$\mathbb{R}_+$
ν_{RMS}	$\mathbb{R}_+$
MAP	16-QAM, 64-QAM, 256-QAM
DEC	ZF

TABLE 5.2: Parameters for baseband receiver control for DSSS signals.

signals, optimized window functions as presented in Chap. 3 are used for signal analysis. Furthermore, real-time computations for the TF coefficients of the elementary waveforms and the pilot signal may be required. If so, the two local repositories in Fig. 4.1 are replaced by the blocks shown in Fig. 5.1.

5.1.2.1 Performance

In the universal mobile telecommunications system terrestrial radio access (UTRA) frequency division duplexing (FDD) air interface, the chip rate is 3.84Mchip/s [1]. One signal frame has a length of 10ms which is divided into 15 slots as shown in Fig. 5.2 for

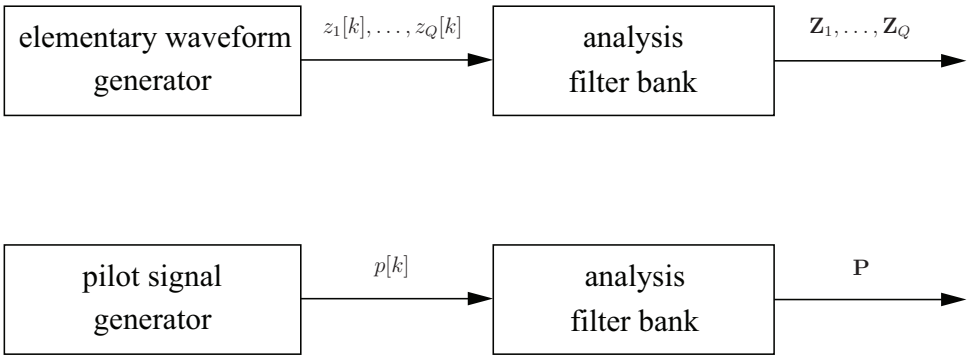

FIGURE 5.1: Set-up for the on-line computation of TF representations of the elementary waveforms and the pilot signal.

the case of the downlink. The downlink Dedicated Physical Channel (DPCH) applies time multiplexing for physical control information and user data transmission [75]. The dedicated physical data channel (DPDCH) carries the user data whereas the dedicated physical control channel (DPCCH) carries the control information, including the transmit power control (TPC) signal, the transport format combination indicator (TFCI) signal, and the pilot signal. In UTRA FDD, a slot comprises 2560 chips of duration $T_{\text{chip}} = 260$ ns

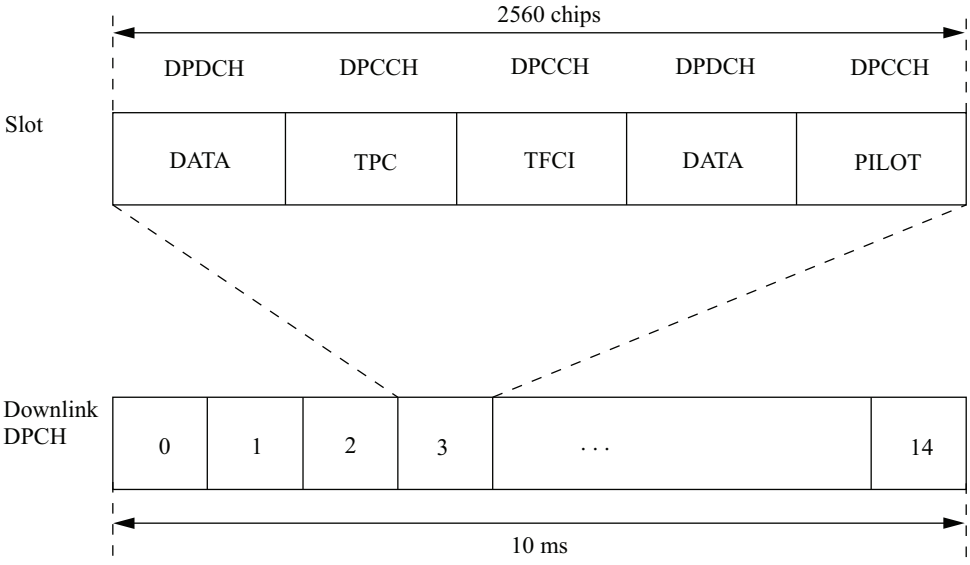

FIGURE 5.2: Downlink DPCH control/data multiplexing [1].

each. All downlink physical channels are subject to a spreading and a scrambling operation as shown in Fig. 5.3 except for the synchronization channel. In the figure, $C_{\text{ch},S_F,n}$ represents the nth PN sequence, in the UMTS standard named channelization code, with spreading factor S_F. Spreading/channelization codes are used for the separation of the

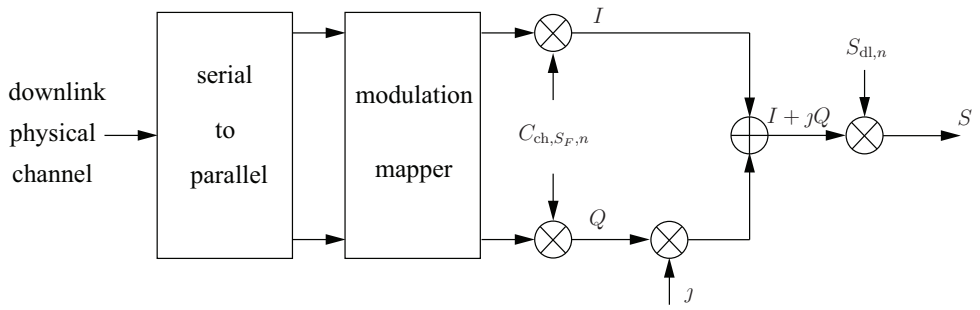

FIGURE 5.3: UMTS downlink spreading and scrambling [2].

signals belonging to different physical channels. Orthogonal variable spreading factor (OVSF) codes are employed in UTRA FDD, allowing for generating channelization codes $C_{\mathrm{ch},S_F,n}$ with different lengths. The codes are real valued, and a certain channelization code $C_{\mathrm{ch},S_F,n}$ is employed for the spreading of both the inphase I and quadrature Q branches. A single complex valued chip sequence is obtained after the combining of the two branches. For facilitating the separation of signals from different base stations in the user terminal, in addition to the spreading a scrambling is performed. That is, the spread signal is chip-wise multiplied by a certain scrambling code $S_{\mathrm{dl},n}$, without having an effect on the sampling rate [2].

In the following performance evaluation, we assume a spreading factor $S_F = 16$, resulting in $Q = 160$ symbols per burst, randomly generated complex channelization/scrambling codes with elements from $\{\pm 1 \pm j\}$, and Q-ary quadrature amplitude modulation (QAM) with Gray encoding. Also randomly generated for every simulated burst reception is a realization of a doubly dispersive channel in line with the Gaussian WSSUS model with a one-sided exponentially decaying delay power spectrum and a two-sided exponentially decaying Doppler power spectrum with a RMS Doppler spread 400Hz and different values of RMS delay spreads. The matched filtering based baseband receiver proposed in Sect. 4.1 is considered with the signal analysis operation using $N = 96$ and $N/K = \frac{3}{4}$ along with optimized window functions. Since $K = 128 = 64 \cdot T_{\mathrm{chip}}$, the signal analysis involves 128-point FFT computations at a double chip rate sampling. The detector performs ZF and symbol detection.

The observed bit-error rates (BERs) in the absence of front-end noise are shown in Fig. 5.4

for perfect channel estimation (i.e., $\widehat{\mathbf{H}} = \mathbf{H}$) and RMS delay spreads between 0.5μs and 4μs, and in Fig. 5.5 for computing $\widehat{\mathbf{H}}$ on the basis of an overlaid pilot signal with similar form and equal power as the information-bearing signal and τ_{RMS} between 0.25μs and 2μs.

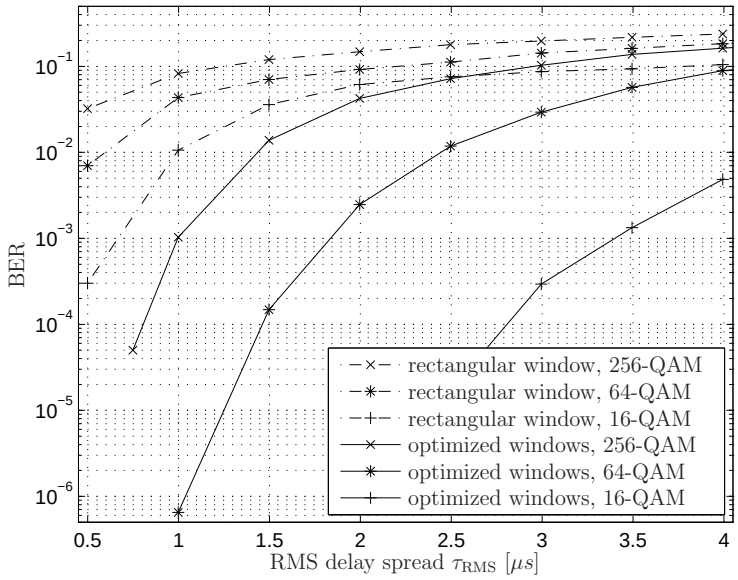

FIGURE 5.4: : BER performance of reconfigurable receiver in UTRA FDD compliant mode with perfect channel knowledge.

Choosing orthogonal channelization codes for the information and pilot signals, $\widehat{\mathbf{H}}$ is computed according to formula (4.25) in Sect. 4.3. For comparison, the two figures also show the performance of a similar receiver based on block-wise DFT computations, that is, $N = 48 \cdot T_{\mathrm{chip}}$ and $N/K = 1$ along with a rectangularly shaped window of length N.

The error-rate performance can obviously be substantially improved through window optimization. Since no forward error correction (FEC) is employed a BER of up to 10^{-3} may be acceptable. With optimized window functions and perfect channel knowledge this is achieved even with 256-QAM unless the RMS delay spread exceeds 1μs, which is usually not the case in UTRA cells[1]. As in most receiver architectures deviations in the channel parameters resulting from pilot signal-based channel estimation have a dominant effect on the error rates, as can be concluded from Fig. 5.5. Higher-order QAM may

[1]In [76] RMS delay spreads of 0.17μs for suburban and 0.65μs for urban environments have been found.

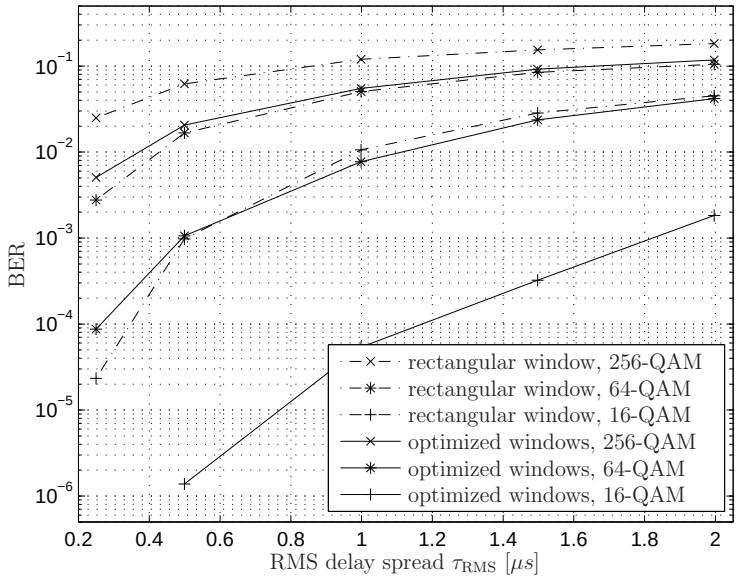

FIGURE 5.5: : BER performance of reconfigurable receiver in UTRA FDD compliant mode with pilot signal-based channel estimates.

only be viable at smaller delay spreads, yet there is also a clear benefit from window optimization in scenarios with imperfect channel knowledge.

In the following, we show the matched filtering based receiver performance taking into account the front-end noise with FEC. The BERs are obtained from employing the multipath channel model defined as case 6 in [77]. Four paths with four different delays and Rayleigh fading characteristics, and a classical U-shaped Doppler spectrum are assumed. The RMS delay spread is approximately 240 ns, and the Doppler spectrum results from assuming a speed of 250 km/h and a 2140 MHz carrier frequency. In the simulations the transmitted signal is constituted by two physical channels, i.e., a data channel with spreading factor 16 and channelization code $C_{\mathrm{ch},16,1}$, and the common pilot channel using channelization code $C_{\mathrm{ch},16,0}$. Furthermore, QPSK modulation and a RRC pulse shaping filter are employed.

Fig. 5.6 shows BERs versus $\frac{E_\mathrm{b}}{N_0}$ defining bit energy over noise power spectral density, which is the signal-to-noise ratio (SNR) per bit. The simulation results are obtained with FEC, employing the rate-$\frac{1}{2}$ convolutional code defined in the IEEE 802.11a standard. The transmitter generates sequences comprising 32000 coded bits. Each bit sequence is

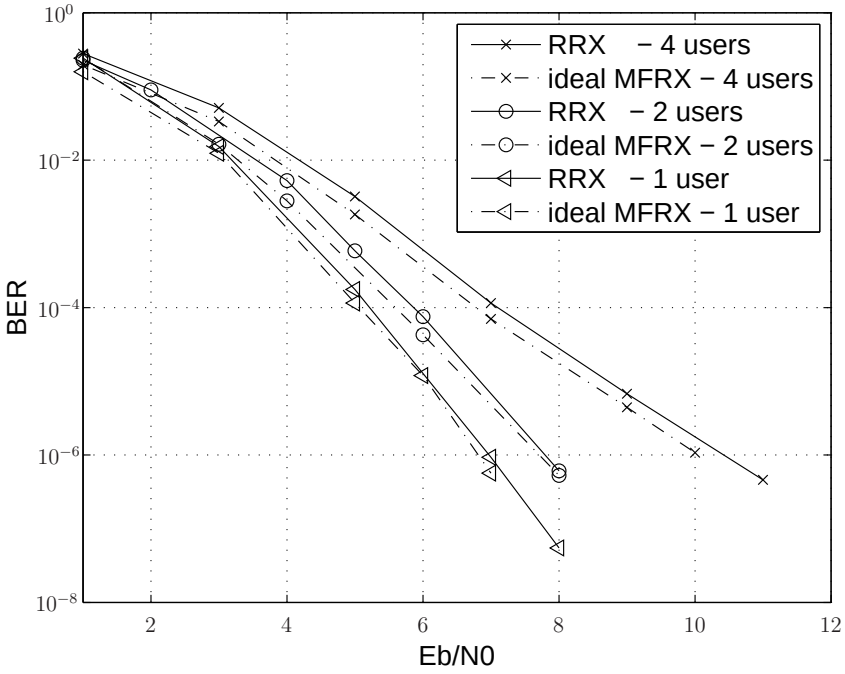

FIGURE 5.6: Coded BER performance over a doubly dispersive channel of an ideal matched filtering receiver and the reconfigurable receiver.

interleaved and divided into 100 blocks of 320 bits each. Each block forms the 160 QPSK signals transmitted within one slot of a superframe. The channels associated with the 100 blocks are generated independently, adopting the channel model described above. In the receiver the signals resulting from the demodulation are de-interleaved. The information bits are finally obtained by a Viterbi decoder.

Fig. 5.6 shows the resulting error rates by the receiver configuration based on matched filtering with the channel estimation scheme described in Sect. 4.3, and for scenarios with only one user, for two users (i.e., with an additional data channel using the channelization code $C_{\mathrm{ch},16,2}$), and for four users (i.e., with three additional data channels with $C_{\mathrm{ch},16,2}$, $C_{\mathrm{ch},16,3}$, $C_{\mathrm{ch},16,4}$). As shown in the figure, the performance degradation in the reconfigurable receiver (RRX) compared to an ideal matched filter (MFRX) is very small. The RRX uses the pilot-aided channel estimation scheme discussed in Chap. 4, while the MFRX employs an ideal matched filtering, that is, the observed signal is matched in the time domain against the elementary waveforms as appearing at the channel output, being computed using perfect channel knowledge.

5.1.2.2 Complexity

In this subsection we discuss the total complexities of the matched filtering based receiver and the equalizer based receiver for UMTS signals. With a spreading factor S_F and an oversampling factor F, one elementary waveform spans $T_\mathrm{e} = S_F F$ samples. Note that because the scrambling is employed on top of the channelization codes, the TF representations of the elementary waveforms and the pilot signal are required to be computed on-line as discussed before.

The complexity of computing the TF coefficients $\mathbf{Z}_1, \ldots, \mathbf{Z}_Q$ of the elementary waveforms via a DFT FB is analogous to the complexity of the received signal expansion. Since on average a transmit side elementary waveform coincides with portions of the base functions associated with $\left\lceil \frac{T_\mathrm{e}+T}{N} \right\rceil$ time slots per symbol, the complexity related to the DFT FB amounts to

$$\left\lceil \frac{T_\mathrm{e}+T}{N} \right\rceil \left((K/2)\log_2 K + T\right) \text{CMs and } \left\lceil \frac{T_\mathrm{e}+T}{N} \right\rceil \left(K \log_2 K + T - K\right) \text{CAs} \qquad (5.1)$$

per symbol. A DFT FB with the same computational complexity per output vector is employed for representing the pilot signal.

For the matched filtering based receiver architecture, the energies of the elementary waveforms are required in order to facilitate demodulation of higher-order QAM signals and soft-decision decoding. The signal cross-correlations, on the other hand, are only needed in more sophisticated receivers such as receivers performing cancellation of ISI, an issue which is not considered here. The energies of the elementary waveforms can be obtained by computing the sums of the squared magnitudes of the respective TF coefficients. This requires

$$\left(\left\lceil \frac{T_\mathrm{e}+T}{N} \right\rceil K \right) \text{CMs and } \left(\left(\left\lceil \frac{T_\mathrm{e}+T}{N} \right\rceil K - 1 \right) \right) \text{CAs} \qquad (5.2)$$

per symbol on average.

For the equalization based receiver architecture, the cross-correlations of the transmitted elementary waveforms are also needed. Since the transmitted elementary waveforms are often designed to be orthogonal, the corresponding pulse cross-correlation matrix has the

form of a diagonal matrix containing the energies of the elementary waveforms. This requires the same number of operations as in (5.2).

Tab. 5.3 provides the numbers of CMs and CAs for the matched filtering based receiver configuration. Assume that $K = 128$, $N = 96$, and a window function of length $T = 136$. For different spreading factors the resulting complexities are listed separately for the signal correlation (the sum of (4.30), (4.32) and (5.1)), the channel estimation (4.31), and the waveform cross-correlation computation (5.2).

spreading factor S_F	(CMs,CAs) for signal correlation	(CMs,CAs) for channel estimation	(CMs,CAs) for waveform cross-correlation
16	$(2264, 2967)$	$(2560, 2304)$	$(256, 255)$
32	$(3104, 3999)$	$(2560, 2304)$	$(384, 383)$
64	$(3688, 4903)$	$(5120, 4608)$	$(384, 383)$
128	$(5952, 7871)$	$(7680, 6912)$	$(640, 631)$
256	$(9384, 12647)$	$(15360, 13824)$	$(896, 895)$

TABLE 5.3: Matched filtering based receiver complexities per symbol in (CMs,CAs).

The numbers in Tab. 5.3 define the number of operations per symbol. The equalizer based receiver has the similar computational complexity as the matched filtering based receiver. A conventional rake receiver requires even less operations than the matched filtering based receiver, but more sophisticated receiver architectures being considered today like, e.g., receivers performing frequency domain equalization may be similarly complex as the equalizer based receiver. In fact, the bulk of the above operations account for FFTs. Furthermore, there is plenty of room for complexity optimization. For instance, all correlations are assumed above to be carried out over the entire frequency spectrum. However, at $F > 1$ and proper pulse shaping filtering, almost $K(F-1)/F$ of the K sub-bands essentially do not carry signals and can thus be neglected.

5.2 URANUS

In the context of flexible radio design for next generation communication systems, the reconfigurable baseband receiver architecture discussed in Chap. 4 has been investigated in the European IST project URANUS. The main objective of the URANUS project was

to develop a universal radio link platform able to be incorporated in any existing proprietary or standardized radio access system, in a seamless way [9]. The URANUS approach supports the simultaneous usage of links with different air interfaces and, in particular, eases the introduction of future user-defined mode operation and reconfigurable air interfaces [9]. Fig. 5.7 shows the scenarios for employing the aforementioned URANUS concept. The scenarios include standard selection diversity, the aforementioned possi-

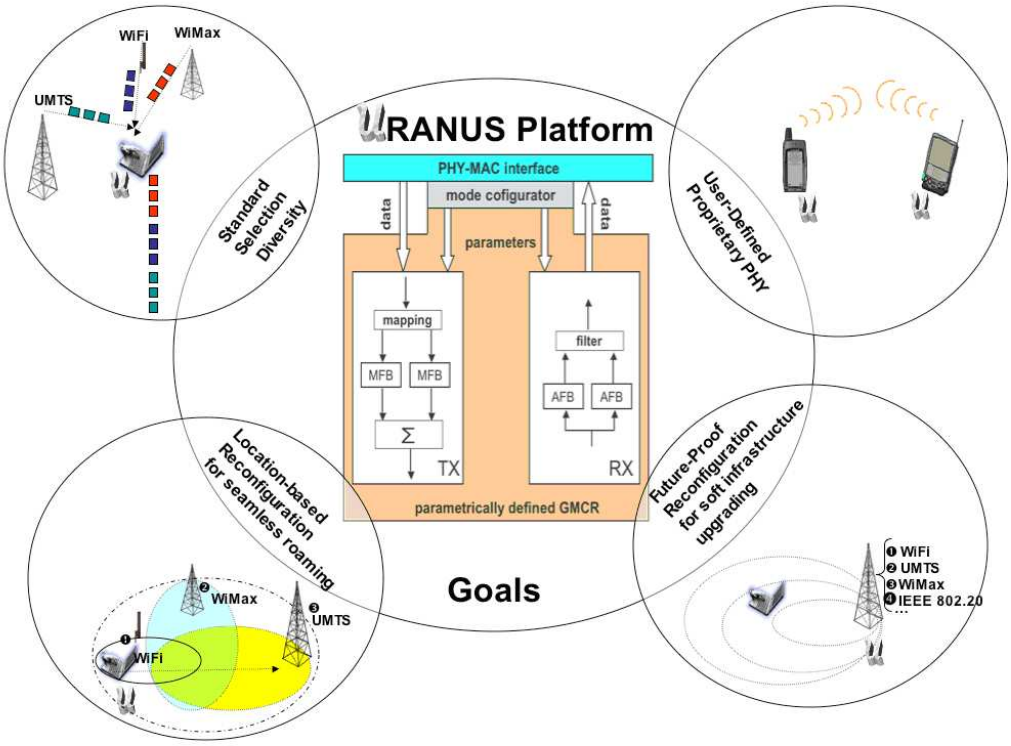

FIGURE 5.7: Scenarios for using URANUS concept [3].

bility of user-defined proprietary PHY transmission, location-based reconfiguration for seamless roaming and future-proof reconfiguration for soft infrastructure upgrading.

The core of the URANUS concept is the PHY design. Apart from flexible front-ends and interfaces to higher layers, the efficient baseband implementation of the PHY plays the key role in universal radio-link platforms. It combines the advantageous implementation properties of orthogonal multi-carrier transmission with the required generality of the baseband signaling format or mode, where each mode is uniquely represented by a corresponding set of parameters. The proposed overall transceiver structure is independent

of the specific choice of the parameter set and, thus, of the mode at hand. URANUS is therefore the solution that implements a generalized modem that can be quickly and easily tailored to the given application. Due to the fixed transceiver architecture, the URANUS approach is also a hardware approach. It attains both the efficiency and compactness of hardware and the flexibility that we can typically attain with a pure software based approach.

In [78], a reconfigurable baseband transmitter architecture is presented with a common waveform processing module for different standards/modes. Linear, single-carrier and multi-carrier modulation schemes are considered. For single-carrier modulations some extra processing on the digital level is required in order to generate transmit signals by a conventional transmitter, while multi-carrier modulation schemes can be directly encompassed with no extra signal processing. The reconfigurable transmitter design also employs the Gabor theory of TF signal representations, and thus involves DFT FBs in the architecture. Although the complexity of the reconfigurable transmitter increases compared to a conventional transmitter implementation, it gains the flexibility of generating various signal formats with a fixed baseband architecture.

Some of the reconfigurable baseband receiver concepts presented in this thesis are outcomes of the URANUS project. While the TF channel diagonalization by means of properly designed paraunitary FBs has been shown to have a great potential, there are a number of related issues that need to be addressed on the way to practical solutions, such as adequate channel estimation methods, synchronization, radio resource management, and others. In [79], a matched filtering based TF domain synchronization scheme has been discussed. The known PN sequences are used as preambles for synchronization. To be compatible with the TF signal processing at the receiver, the conventional frequency domain synchronization is extended to a generic approach of acquisition in the TF domain. Another related topic investigated within the project is bit and power loading for reconfigurable transmitters. The one-dimensional water filling principle in the frequency domain has been generalized to a two-dimensional water surface principle which is applicable in the TF domain [80]. Optimized power allocation strategies have been derived taking into account the dependencies of the power between the elementary functions used to synthesize the transmit signal.

The URANUS validation has been accomplished using a digital baseband implementation with focus on PHY aspects. Both the reconfigurable transmitter and receiver functionalities have been implemented. The ST Microelectronics GreenSIDE board developed for base stations [81] has been used as validation platform. The PHY functions defined by both UMTS/WCDMA and WiMAX/IEEE802.16e standards are included in the implementation. The validation platform enables real-time operation and the switching between different modes of operation. The measurement results have been presented in [82] with a concise description of the set-up for the test scenarios. The measurements included transceiver characteristics such as the signal spectra, receiver sensitivity, throughput, BERs, symbol-error rates, and block-error rates.

Chapter 6

Conclusions and Outlook

6.1 Conclusions

The growing number of standards for wireless access and networking motivates a trend towards reconfigurable transceiver devices. Since the assembling of tailored solutions for single standards into hybrid devices has clear limitations, multi-mode monolithic receiver devices for universal wireless communications that support a wide range of air interfaces are highly desired.

In this thesis, a reconfigurable baseband receiver architecture with multi-standard capability is proposed, which represents a generalization of OFDM receivers in the following aspects. First, since tight frames used for signal transformations in the proposed receiver are natural generalizations of orthonormal bases used for signal transforms in OFDM receivers, the efficient handling of dispersive channels by OFDM receivers can be inherited by the reconfigurable receiver being not limited to signals with cyclic extensions. Secondly, the signal processing in an OFDM receiver is performed in the frequency domain, whereas the proposed reconfigurable receiver processes the signals in the TF domain. Thirdly, the reconfigurable receiver is designed to handle the signals at the output of doubly dispersive channels, while OFDM receivers are usually limited to deal with signals from time-invariant multipath channels. Finally, the reconfigurable receiver employs

FB implementations with window functions of arbitrary shapes, while in OFDM a block-wise FFT is performed.

The TF domain channel diagonalization is the key for deriving a uniform architecture of the baseband receiver. Optimized paraunitary FB configurations are presented which facilitate diagonalization of doubly dispersive channels with limited values of the inherent MSE between the received signal and its model used for the receiver design. It is shown that the optimization of paraunitary FBs for given channel statistics can be formulated as a CO problem making use of a suitable parameterization of tight frames. However, in certain scenarios the necessary rank reduction following the CO has a significant impact on the window shapes. The induced potential degradation of the MSE performance may be evaded by choosing appropriate lattice constants N and K, specifying the down-sampling factor and the number of sub-bands, respectively. In general, the MSE performance can be improved at the cost of a higher complexity in terms of numbers of coefficients by increasing the oversampling ratio.

Flexible radio architectures based on the TF domain channel diagonalization have been investigated for both OFDM and DSSS signals. The proposed receiver architecture can be easily configured to a matched filtering based receiver and an equalizer based receiver. The case of DSSS signals in line with the downlink UTRA FDD air interface specification has been studied as an example. We find that in typical urban and suburban environments the impact of the channel diagonalization error can be limited to acceptable levels through window design, however, the performance degradation due to imperfect channel estimation may be considerable. The computational complexity required for demodulation depends on signal structures associated with specific air interfaces. However, in general the complexity can be assumed to be comparable to the complexity of corresponding single mode receivers with frequency domain processing. Of course generality and reconfigurability always come at a certain cost in error-rate performance and/or complexity.

6.2 Open Problems

The FB based reconfigurable baseband receiver is designed so far for employing single user detection methods. An extension towards the inclusion of multiuser detection methods would make the architecture even more attractive for base stations for example in UMTS systems.

It has been discussed that one may benefit from the equalizer based receiver architecture with respect to complexity due to the restoring the orthogonality of signals in scenarios such as UMTS downlink transmission. However, the simple inversion of the channel coefficients clearly leads to a noise amplification and more robust detection schemes should therefore be investigated like e.g. LMMSE approaches.

As for the window optimization of the TF domain channel diagonalization, more efficient convex optimization algorithms can be employed. Furthermore, by alternative rank reduction procedures the MSE of the channel diagonalization can be reduced which will result in improved receiver performance.

Appendix A

Derivation of MSE in the TF Domain

The MSE (3.20) in the TF domain ϵ_{TF} can be written as

$$\begin{aligned}\epsilon_{\mathrm{TF}}(g) = & \underbrace{\frac{N}{K}\lim_{Q\to\infty}\frac{1}{Q}E\left[\sum_{(\ell,m)\in\Lambda_Q}\left|H\left[\ell,m\right]\left\langle x_Q, g_{\ell,m}\right\rangle\right|^2\right]}_{\varphi_1} \\ & + \underbrace{\frac{N}{K}\lim_{Q\to\infty}\frac{1}{Q}E\left[\sum_{(\ell,m)\in\Lambda_Q}\left|\left\langle \mathcal{H}x_Q, g_{\ell,m}\right\rangle\right|^2\right]}_{\varphi_2} \\ & \underbrace{-2\,\frac{N}{K}\lim_{Q\to\infty}\frac{1}{Q}E\left[\sum_{(\ell,m)\in\Lambda_Q}\Re\big(\left\langle \mathcal{H}x_Q, g_{\ell,m}\right\rangle H^*[\ell,m]\left\langle x_Q, g_{\ell,m}\right\rangle^*\big)\right]}_{\varphi_3}, \end{aligned} \tag{A.1}$$

where $\Re\left(\cdot\right)$ denotes the real part operator. Both the input signal power and the gain of the channel are normalized to unity, and therefore

$$\varphi_1 = \varphi_2 = \left\|g\right\|^2. \tag{A.2}$$

By applying (3.12) and (3.13) φ_3 can be rewritten as

$$\begin{aligned}
\varphi_3 &= \frac{N}{K}\lim_{Q\to\infty}\frac{1}{Q}E\Bigg[\Re\Bigg(\sum_{(\ell,m)\in\Lambda_Q}\sum_{k=-Q/2}^{Q/2}\sum_{q=0}^{\infty}c\left[k,q\right]x\left[k-q\right]g^{*}_{\ell,m}[k] \\
&\quad\times\sum_{q'=0}^{\infty}c^{*}\left[\ell N,q'\right]\exp\left(\jmath 2\pi mq'/K\right)\sum_{k'=-Q/2}^{Q/2}x^{*}[k']g_{\ell,m}[k']\Bigg)\Bigg] \qquad \text{(A.3)}\\
&= \frac{N}{K}\lim_{Q\to\infty}\frac{1}{Q}E\Bigg[\Re\Big(\sum_{(\ell,m)\in\Lambda_Q}\sum_{k=-Q/2}^{Q/2}\sum_{q=0}^{\infty}\sum_{q'=0}^{\infty}c\left[k,q\right]g^{*}_{\ell,m}[k]c^{*}\left[\ell N,q'\right]\exp\left(\jmath 2\pi mq'/K\right) \\
&\quad\times g_{\ell,m}[k-q]\Big)\Bigg] \qquad \text{(A.4)}\\
&= \frac{N}{K}\lim_{Q\to\infty}\frac{1}{Q}\Re\Bigg(\sum_{(\ell,m)\in\Lambda_Q}\sum_{k=-Q/2}^{Q/2}\sum_{q=0}^{\infty}\phi_t[k-\ell N]S_{\text{delay}}\left[q\right]g^{*}_{\ell,m}[k]g_{\ell,m}[k-q] \\
&\quad\times\exp\left(\jmath 2\pi mq/K\right)\Bigg) \qquad \text{(A.5)}\\
&= \Re\left[\langle(g*S_{\text{delay}})\odot\phi_{\text{t}},g\rangle\right], \qquad \text{(A.6)}
\end{aligned}$$

where $*$ denotes convolution. To obtain (A.4) from (A.3) we apply (3.18), and to arrive at (A.5), (3.10) is used. For the derivation of (A.6) from (A.5), the definition of time-discrete Gabor systems (2.2) is applied.

Thus, $\epsilon_{\text{TF}}(g)$ is given by

$$\epsilon_{\text{TF}}(g)=2\left(\|g\|^2-\Re\left[\langle(g*S_{\text{delay}})\odot\phi_{\text{t}},g\rangle\right]\right). \qquad \text{(A.7)}$$

Appendix B

Derivation of MSE in the Time Domain

The MSE (3.22) in the time domain ϵ_{T} can be written as

$$\begin{aligned}\epsilon_{\mathrm{T}}(g) = & \underbrace{\lim_{Q\to\infty} E\left[\frac{1}{Q}\sum_{k=-Q/2}^{Q/2}\left|\sum_{(\ell,m)\in\Lambda} H\left[\ell,m\right]\left\langle x_Q, g_{\ell,m}\right\rangle g_{\ell,m}\left[k\right]\right|^2\right]}_{\tilde{\varphi}_1\triangleq} \\ & \underbrace{+\lim_{Q\to\infty} E\left[\frac{1}{Q}\sum_{k=-Q/2}^{Q/2}\left|\sum_{q=0}^{\infty} c\left[k,q\right] x_Q\left[k-q\right]\right|^2\right]}_{\tilde{\varphi}_2\triangleq} \\ & \underbrace{-2\lim_{Q\to\infty} E\left[\frac{1}{Q}\sum_{k=-Q/2}^{Q/2}\Re\left(\sum_{q=0}^{\infty}\sum_{(\ell,m)\in\Lambda} c\left[k,q\right] x_Q\left[k-q\right] H^*\left[\ell,m\right]\left\langle x_Q, g_{\ell,m}\right\rangle^* g^*_{\ell,m}[k]\right)\right]}_{\tilde{\varphi}_3\triangleq}.\end{aligned} \tag{B.1}$$

Both the input signal power and the gain of the channel are normalized to unity, and therefore $\tilde{\varphi}_2 = 1$.

In (B.1), $\tilde{\varphi}_1$ can be expressed as

$$\begin{aligned}
\tilde{\varphi}_1 &= \lim_{Q\to\infty}\frac{1}{Q}\sum_{k=-Q/2}^{Q/2}\sum_{(\ell,m)\in\Lambda}\sum_{(\ell',m')\in\Lambda} E\left[H^*\left[\ell,m\right]H\left[\ell,m\right]\right] \\
&\quad\times\sum_{k'=-Q/2}^{Q/2}\sum_{k''=-Q/2}^{Q/2} E\left[x_Q^*\left[k'\right]x_Q\left[k''\right]\right] g_{\ell,m}\left[k'\right]g_{\ell',m'}^*\left[k''\right]g_{\ell,m}^*\left[k\right]g_{\ell',m'}\left[k\right] \qquad \text{(B.2)} \\
&= \lim_{Q\to\infty}\frac{1}{Q}\sum_{k=-Q/2}^{Q/2}\sum_{(\ell,m)\in\Lambda}\sum_{(\ell',m')\in\Lambda}\sum_{q=0}^{\infty}\sum_{q'=0}^{\infty} E\left[c^*\left[\ell N,q\right]c\left[\ell' N,q'\right]\right] \\
&\quad\times\exp\left(\jmath 2\pi(mq-m'q')/K\right)\sum_{k'=-Q/2}^{Q/2} g_{\ell,m}\left[k'\right]g_{\ell',m'}^*\left[k'\right]g_{\ell,m}^*\left[k\right]g_{\ell',m'}\left[k\right] \qquad \text{(B.3)} \\
&= \lim_{Q\to\infty}\frac{1}{Q}\sum_{(\ell,m)\in\Lambda_Q}\sum_{(\ell',m')\in\Lambda_Q}\phi_{\mathrm{t}}\left[\ell N-\ell' N\right]\sum_{q=0}^{\infty}S_{\mathrm{delay}}\left[q\right]\exp\left(\jmath 2\pi(m-m')q/K\right) \\
&\quad\times\left\langle g_{\ell,m},g_{\ell',m'}\right\rangle\left\langle g_{\ell',m'},g_{\ell,m}\right\rangle, \qquad \text{(B.4)}
\end{aligned}$$

where $\Lambda_Q=\left\{-\left\lfloor\frac{Q}{2N}\right\rfloor,\ldots,\left\lfloor\frac{Q}{2N}\right\rfloor\right\}\times\{0,\ldots,K-1\}$. To obtain (B.3) from (B.2) we apply (3.12), (3.13), and (3.18), and to arrive at (B.4) we use (3.10). Using (2.2) and (3.11), $\tilde{\varphi}_1$ can now be expressed as

$$\begin{aligned}
\tilde{\varphi}_1 &= \lim_{Q\to\infty}\frac{1}{Q}\,\frac{K}{N}\sum_{(\ell,m)\in\Lambda_Q}\phi_{\mathrm{t}}\left[\ell N\right]\phi_{\mathrm{f}}\left[2\pi m/K\right]\left\langle g_{\ell,m},g_{0,0}\right\rangle\left\langle g_{0,0},g_{\ell,m}\right\rangle \\
&= \frac{K}{N}\sum_{(\ell,m)\in\Lambda}\phi_{\mathrm{t}}\left[\ell N\right]\phi_{\mathrm{f}}\left[2\pi m/K\right]\left|\left\langle g_{0,0},g_{\ell,m}\right\rangle\right|^2. \qquad \text{(B.5)}
\end{aligned}$$

Finally, $\tilde{\varphi}_3$ can be rewritten as

$$\begin{aligned}
\tilde{\varphi}_3 = \lim_{Q\to\infty} \frac{1}{Q} \sum_{k=-Q/2}^{Q/2} \Re \Bigg(E \Bigg[\sum_{(\ell,m)\in\Lambda} \sum_{q=0}^{\infty} c\left[k,q\right] \sum_{q'=0}^{\infty} c^*\left[\ell N, q'\right] \exp\left(\jmath 2\pi m q'/k\right) g^*_{\ell,m}\left[k\right] \\
\times \sum_{k'=-Q/2}^{Q/2} x_Q\left[k-q\right] x^*_Q\left[k'\right] g_{\ell,m}\left[k'\right] \Bigg] \Bigg) \qquad \text{(B.6)} \\
= \lim_{Q\to\infty} \frac{1}{Q} \Re \Bigg(\sum_{(\ell,m)\in\Lambda} \sum_{k=-Q/2}^{Q/2} \sum_{q=0}^{\infty} \sum_{q'=0}^{\infty} E\left[c\left[k,q\right] c^*\left[\ell N, q'\right]\right] \\
\times g^*_{\ell,m}\left[k\right] \exp\left(\jmath 2\pi m q'/k\right) g_{\ell,m}\left[k-q\right] \Big) \qquad \text{(B.7)} \\
= \lim_{Q\to\infty} \frac{1}{Q} \Re \Bigg(\sum_{(\ell,m)\in\Lambda} \sum_{k=-Q/2}^{Q/2} \sum_{q=0}^{\infty} \phi_{\mathrm{t}}\left[k-\ell N\right] S_{\mathrm{delay}}\left[q\right] \\
\times g^*_{\ell,m}\left[k\right] g_{\ell,m}\left[k-q\right] \exp\left(\jmath 2\pi m q/k\right) \Big) \qquad \text{(B.8)} \\
= \lim_{Q\to\infty} \frac{1}{Q} \frac{K}{N} \Re \Bigg(\sum_{k=-Q/2}^{Q/2} \phi_{\mathrm{t}}\left[k\right] \sum_{q=0}^{\infty} S_{\mathrm{delay}}\left[q\right] g_{0,0}\left[k-q\right] g^*_{0,0}\left[k\right] \Bigg) \qquad \text{(B.9)} \\
= \frac{K}{N} \Re\left(\left\langle \left(g_{0,0} * S_{\mathrm{delay}}\right) \odot \phi_{\mathrm{t}}, g_{0,0} \right\rangle \right). \qquad \text{(B.10)}
\end{aligned}$$

We use (3.18) to obtain (B.7) from (B.6), and for the derivation of (B.8), (3.10) is applied.

Thus, $\epsilon_{\mathrm{T}}(g)$ is given by

$$\epsilon_{\mathrm{T}}(g) = 1 + \frac{K}{N} \left(\sum_{(\ell,m)\in\Lambda} \phi_{\mathrm{t}}\left[\ell N\right] \phi_{\mathrm{f}}\left[2\pi m/K\right] \left|\left\langle g, g_{\ell,m}\right\rangle\right|^2 - 2\Re\left(\left\langle \left(g * S_{\mathrm{delay}}\right) \odot \phi_{\mathrm{t}}, g \right\rangle \right) \right). \qquad \text{(B.11)}$$

Appendix C

The Statistics of the Noise Term Resulting from ZF

Assume the matrix $\bar{\mathbf{Z}}$ of dimension $(DK) \times Q$ with jth column $\mathrm{st}\left[\mathbf{Z}_q\right]$ containing the TF coefficients of the qth elementary waveforms z_q. As a consequence, the matrix $\tilde{\mathbf{A}}$ with elements $[\tilde{\mathbf{A}}]_{i,j} = \langle \mathbf{Z}_j, \mathbf{Z}_i \rangle$ can be written as $\tilde{\mathbf{A}} = \bar{\mathbf{Z}}^{\mathrm{H}}\bar{\mathbf{Z}}$. Assume the noise is white with power density N_0, i.e, $E\left[\mathbf{W}\mathbf{W}^{\mathrm{H}}\right] = N_0\mathbf{I}$. According to (4.16), the covariance of $\tilde{\mathbf{v}}$ is expressed as

$$E\left[\tilde{\mathbf{v}}\tilde{\mathbf{v}}^{\mathrm{H}}\right] = N_0\bar{\mathbf{Z}}^{\mathrm{H}}\mathrm{Diag}\left[\mathrm{st}\left[\hat{\mathbf{H}}\right]\right]^{-1}\mathrm{Diag}\left[\mathrm{st}\left[\hat{\mathbf{H}}\right]\right]^{\mathrm{H}^{-1}}\bar{\mathbf{Z}}. \tag{C.1}$$

Thus, the covariance of the term $\tilde{\mathbf{A}}^{-1}\tilde{\mathbf{v}}$ is given by

$$\begin{aligned} E\left[\tilde{\mathbf{A}}^{-1}\tilde{\mathbf{v}}\tilde{\mathbf{v}}^{\mathrm{H}}\tilde{\mathbf{A}}^{\mathrm{H}^{-1}}\right] &= \left(\bar{\mathbf{Z}}^{\mathrm{H}}\bar{\mathbf{Z}}\right)^{-1}E\left[\tilde{\mathbf{v}}\tilde{\mathbf{v}}^{\mathrm{H}}\right]\left(\bar{\mathbf{Z}}^{\mathrm{H}}\bar{\mathbf{Z}}\right)^{\mathrm{H}^{-1}} \\ &= N_0\bar{\mathbf{Z}}^{-1}\mathrm{Diag}\left[\mathrm{st}\left[\hat{\mathbf{H}}\right]\right]^{-1}\mathrm{Diag}\left[\mathrm{st}\left[\hat{\mathbf{H}}\right]\right]^{\mathrm{H}^{-1}}\bar{\mathbf{Z}}^{\mathrm{H}^{-1}}. \end{aligned} \tag{C.2}$$

Similar to the above result, the covariance of $\hat{\mathbf{A}}^{-1}\mathbf{v}$ in (4.28) of the matched filtering based receiver can be written as

$$E\left[\hat{\mathbf{A}}^{-1}\mathbf{v}\mathbf{v}^{\mathrm{H}}\hat{\mathbf{A}}^{\mathrm{H}^{-1}}\right] = N_0\hat{\mathbf{A}}^{\mathrm{H}^{-1}}. \tag{C.3}$$

Note that the matrix $\hat{\mathbf{A}}$ with the entries $[\hat{\mathbf{A}}]_{i,j} = \langle \hat{\mathbf{H}} \odot \mathbf{Z}_j, \hat{\mathbf{H}} \odot \mathbf{Z}_i \rangle$ can be written as $\hat{\mathbf{A}} = \bar{\mathbf{Z}}^{\mathrm{H}} \mathrm{st}\left[\hat{\mathbf{H}}\right]^{\mathrm{H}} \mathrm{st}\left[\hat{\mathbf{H}}\right] \bar{\mathbf{Z}}$, and its inverse $\hat{\mathbf{A}}^{-1}$ can therefore be expressed as

$$\hat{\mathbf{A}}^{-1} = \bar{\mathbf{Z}}^{-1} \left(\mathrm{st}\left[\hat{\mathbf{H}}\right]^{\mathrm{H}} \mathrm{st}\left[\hat{\mathbf{H}}\right] \right)^{-1} \bar{\mathbf{Z}}^{\mathrm{H}^{-1}}. \tag{C.4}$$

Applying (C.4), the covariance of $\hat{\mathbf{A}}^{-1}\mathbf{v}$ in (C.3) can be further written as

$$\begin{aligned} E\left[\hat{\mathbf{A}}^{-1}\mathbf{v}\mathbf{v}^{\mathrm{H}}\hat{\mathbf{A}}^{\mathrm{H}^{-1}}\right] &= N_0 \bar{\mathbf{Z}}^{-1} \left(\mathrm{st}\left[\hat{\mathbf{H}}\right]^{\mathrm{H}} \mathrm{st}\left[\hat{\mathbf{H}}\right] \right)^{\mathrm{H}^{-1}} \bar{\mathbf{Z}}^{\mathrm{H}^{-1}} \\ &= \frac{N_0}{\left\langle \mathrm{st}\left[\hat{\mathbf{H}}\right], \mathrm{st}\left[\hat{\mathbf{H}}\right] \right\rangle} \bar{\mathbf{Z}}^{-1} \bar{\mathbf{Z}}^{\mathrm{H}^{-1}}. \end{aligned} \tag{C.5}$$

Note that $\mathrm{Diag}\left[\mathrm{st}\left[\hat{\mathbf{H}}\right]\right]^{-1} \mathrm{Diag}\left[\mathrm{st}\left[\hat{\mathbf{H}}\right]\right]^{\mathrm{H}^{-1}} = \left(\left\langle \mathrm{st}\left[\hat{\mathbf{H}}\right], \mathrm{st}\left[\hat{\mathbf{H}}\right] \right\rangle \right)^{-1}$. From (C.2) and (C.5), we have

$$E\left[\hat{\mathbf{A}}^{-1}\mathbf{v}\mathbf{v}^{\mathrm{H}}\hat{\mathbf{A}}^{\mathrm{H}^{-1}}\right] = E\left[\tilde{\mathbf{A}}^{-1}\tilde{\mathbf{v}}\tilde{\mathbf{v}}^{\mathrm{H}}\tilde{\mathbf{A}}^{\mathrm{H}^{-1}}\right], \tag{C.6}$$

which indicates the statistics of the noise term after the ZF approach from both matched filtering based receiver and equalizer based receiver are the same.

Bibliography

[1] *UMTS; Physical channels and mapping of transport channels onto physical channels (FDD) (Release 1999).* Technical specification, 3GPP T63-25.211 V3.11.0.

[2] *UMTS; Spreading and modulation (FDD) (Release 7).* Technical specification, 3GPP TS 25.213 version 7.0.0 Release 7.

[3] http://www.IST-URANUS.org/.

[4] M. Dillinger, K. Madani, and N. Alonistioti, *Software Defined Radio: Architectures, Systems and Functions.* West Sussex, England: John Wiley & Sons, 1993.

[5] W. Tuttlebee, *Software Defined Radio Enabling Technologies.* West Sussex, England: John Wiley & Sons, 2002.

[6] R. Kakerow, M. Mueller, D. Pienkowski, R. Circa, and G. Boeck, "Reconfigurable receiver approach for 4G terminals and beyond," in *Proc. IEEE-NEWCAS Conference*, pp. 9–12, 2005.

[7] M. Mehta and M. Wesseling, "Adaptive baseband sub-system for 'TRUST'," in *Proc. IEEE PIMRC'00*, vol. 1, pp. 29–33, Sept. 2000.

[8] *Transparently Reconfigurable UbiquitouS Terminals (TRUST) project, conducted as part of the IST Programme of the European Unions Fifth Framework.* http://www.IST-TRUST.org/.

[9] *User Scenarios and Physical layer requirements for Specification U-technology.* http://www.IST-URANUS.org/.

[10] D. W. Bennett, P. B. Kenington, and J. P. McGeehan, "The ACTS FIRST project and its approach to software radio design," in *IEE Colloquium on "Adaptable and Multistandard Mobile Radio Terminals"*, (London, UK), pp. 4/1–4/6, May 1998.

[11] J. M. Pereira, "Reconfigurable radio: the evolving perspectives of different players," in *Proc. IEEE Int. Sym. on Personal, Indoor and Mobile Radio Communications*, pp. 79–84, Sept. 2001.

[12] H. Harada, Y. Kamio, and M. Fujise, "Multimode software radio system by parameter controlled and telecommunication component block embedded digital signal processing hardware," *IEICE Trans. Commun.*, vol. E83-B, pp. 1217–1228, June 2000.

[13] P. P. Vaidyanathan, *Multirate Systems and Filter Banks*. Englewood Cliffs, NJ: Prentice-Hall, 1993.

[14] C. Siclet, P. Siohan, and D. Pinchon, "Perfect reconstruction conditions and design of oversampled DFT-modulated transmultiplexers," *EURASIP Journal on Applied Signal Processing archive*, pp. 1–14, 2006.

[15] A. Scaglione, G. B. Giannakis, and S. Barbarossa, "Redundant filter bank precoders and equalizers part I: Unification and optimal designs," *IEEE Trans. Signal Processing*, vol. 47, pp. 1988–2006, July 1999.

[16] S. Weiss, "On the design of oversampled filter banks for channel coding," in *Proc. EUSIPCO*, pp. 885–888, Sept. 2004.

[17] G. B. Giannakis, "Filter banks for blind channel identification and equalization," *IEEE Sig. Processing Lett.*, vol. 4, pp. 184–187, June 1997.

[18] W. Kozek and A. F. Molisch, "Nonorthogonal pulseshapes for multicarrier communications in doubly dispersive channels," *IEEE J. Select. Areas Commun.*, vol. 16, pp. 1579–1589, Oct. 1998.

[19] P. Jung and G. Wunder, "The WSSUS pulse design problem in multicarrier transmission," *IEEE Trans. Commun.*, vol. 55, pp. 1918–1928, Oct. 2007.

[20] T. Hunziker and D. Dahlhaus, "Iterative detection for multicarrier transmission employing time-frequency concentrated pulses," *IEEE Trans. Commun.*, vol. 51, pp. 641–651, Apr. 2003.

[21] M. Bellanger, "Specification and design of a prototype filter for filter bank based multicarrier transmission," in *Proc. IEEE Int. Conf. Acoustics, Speech, and Signal Processing*, vol. 4, pp. 2417–2420, 2001.

[22] S.-M. Phoong, Y. Chang, and C.-Y. Chen, "DFT-modulated filterbank transceivers for multipath fading channels," *IEEE Trans. Signal Processing*, vol. 53, pp. 182–192, Jan. 2005.

[23] P. Jung and G. Wunder, "On time-variant distortions in multicarrier transmission with application to frequency offsets and phase noise," *IEEE Trans. Signal Processing*, vol. 11, pp. 883–886, Nov. 2004.

[24] W.-K. Ma, P. C. Ching, and K. M. Wong, "Maximum likelihood detection for multicarrier systems employing non-orthogonal pulse shapes," in *Proc. IEEE Int. Conf. on Acoustics, Speech, and Signal Processing (ICASSP)*, (Istanbul, Turkey), pp. 2489–2492, June 2000.

[25] P. Schniter, "A new approach to multicarrier pulse design for doubly-dispersive channels," in *Proc. Allerton Conf. Commun., Control, and Computing*, (Monticello, IL), pp. 1012–1021, Oct. 2003.

[26] T. Strohmer and S. Beaver, "Optimal OFDM design for time-frequency dispersive channels," *IEEE Trans. Commun.*, vol. 51, pp. 1111–1122, July 2003.

[27] M. Schwartz, W. R. Bennett, and S. Stein, *Communication Systems and Techniques*. Wiley-IEEE Press, 1st ed., 1995.

[28] J. G. Proakis, *Digital Communications*. New York, NY: McGraw-Hill, 4th ed., 2001.

[29] A. Saadani, S. Wendt, P. Gelp, and D. Duponteil, "A tapped delay line model of multipath channel for CDMA systems," in *First International Symposium on Control, Communications and Signal Processing*, (San Francisco, CA), pp. 783–786, Sept. 2004.

[30] R. Prasad, *OFDM for Wireless Communications Systems*. Norwood, MA: Artech House, 1st ed., 2000.

[31] F. Hlawatsch and G. F. Boudreaux-Bartels, "Linear and quadratic time-frequency signal representations," *IEEE Sig. Processing Mag.*, vol. 9, pp. 21–67, Aug. 2002.

[32] H. G. Feichtinger and T. Strohmer, *Gabor Analysis and Algorithms: Theory and Applications*. Boston, MA: Birkhäuser, 1998.

[33] I. Daubechies, *Ten Lectures on Wavelets*. Philadelphia, PA: SIAM, 1992.

[34] K. Gröchenig, *Foundations of Time-Frequency Analysis*. Boston, MA: Birkhäuser, 2001.

[35] H. Bölcskei, F. Hlawatsch, and H. G. Feichtinger, "Equivalence of DFT filter banks and Gabor expansions," in *SPIE Proc. Vol. 2569, "Wavelet Applications in Signal and Image Processing III"*, (San Diego, CA), pp. 128–139, July 1995.

[36] O. Christensen, *An Introduction to Frames and Riesz Bases*. Boston, MA: Birkhäuser, 2003.

[37] S. Houwen, T. Chen, and S. A. Norman, "Design of FIR multirate filter banks using convex optimization," in *Proc. IEEE Pacific Rim Conf. on Communications, Computers and Signal Processing*, (Victoria, Canada), pp. 469–472, Aug. 1997.

[38] J. Xu and T. Strohmer, "Pulse construction in OFDM systems via convex optimization," *IEEE Trans. Commun.*, vol. 56, pp. 1225–1230, Aug. 2008.

[39] B. Borna and T. N. Davidson, "Efficient filter bank design for filtered multitone modulation," in *Proc. IEEE Int. Conf. Commun.*, (Paris, France), pp. 38–42, June 2004.

[40] M. R. Wilbur, T. N. Davidson, and J. P. Reilly, "Efficient design of oversampled NPR GDFT filterbanks," *IEEE Trans. Signal Processing*, vol. 52, pp. 1947–1963, July 2004.

[41] H. H. Kha, H. D. Tuan, and T. Q. Nguyen, "Efficient design of cosine-modulated filter banks via convex optimization," *IEEE Trans. Signal Processing*, vol. 57, pp. 966–976, Mar. 2009.

[42] A. Karmakar, A. Kumar, and R. K. Patney, "Design of an optimal two-channel orthogonal filter bank using semidefinite programming," *IEEE Sig. Processing Lett.*, vol. 14, pp. 692–694, Oct. 2007.

[43] S. Akkarakaran and P. P. Vaidyanathan., "Filter bank optimization with convex objectives, and the optimality of principal component forms," *IEEE Trans. Signal Processing*, pp. 100–114, Jan. 2001.

[44] H. Bölcskei and F. Hlawatsch, "Discrete Zak transforms, polyphase transforms, and applications," *IEEE Trans. Signal Processing*, vol. 45, pp. 851–866, Apr. 1997.

[45] Z. Ju, T. Hunziker, and D. Dahlhaus, "Time-frequency parameterization of doubly dispersive channels," in *European Signal Processing Conf. (EUSIPCO '09)*, (Glasgow, Scotland), pp. 1675–1679, Aug. 2009.

[46] Z. Ju, T. Hunziker, and D. Dahlhaus, "Optimized paraunitary filter banks for time-frequency channel diagonalization," *EURASIP Journal on Advances in Signal Processing (accepted)*, Dec. 2009.

[47] Z. Cvetkovic and M. Vetterli, "Tight Weyl-Heisenberg frames in $\ell^2(\mathbb{Z})$," *IEEE Trans. Signal Processing*, vol. 46, pp. 1256–1259, May 1998.

[48] D. Gabor, "Theory of communication," *I.E.E.*, vol. 93(III), pp. 429–457, Nov. 1946.

[49] I. Daubechies, "The wavelet transform, time-frequency localization and signal analysis," *IEEE Trans. Inform. Theory*, vol. 36, pp. 961–1005, 1990.

[50] M. Bellanger, G. Bonnerot, and M. Coudreuse, "Digital filtering by polyphase network:application to sample-rate alteration and filter banks," *IEEE Trans. Acoustics, Speech and Signal Processing*, vol. 24, pp. 109–114, Apr. 1976.

[51] T. Hunziker, Z. Ju, and D. Dahlhaus, "Efficient channel description in time-frequency domain with application to flexible radio," in *Proc. European Signal Processing Conf. (EUSIPCO '07)*, (Poznan, Poland), pp. 866–870, Sept. 2007.

[52] P. A. Bello, "Characterization of randomly time-variant linear channels," *IEEE Trans. Commun. Syst.*, vol. 11, pp. 360–393, Dec. 1963.

[53] A. F. Molisch, *Wireless Communications*. West Sussex, England: John Wiley & Sons, 2005.

[54] M. Ibnkahla, *Signal Processing for Mobile Communications Handbook*. USA: CRC Press, 2004.

[55] W. Kozek, *Matched Weyl-Heisenberg expansions of nonstationary environments*. Ph.D. thesis, Vienna University of Technology, Department of Electrical Engineering, Vienna, Austria, 1997.

[56] G. Durisi, H. Bölcskei, and S. Shamai, "Capacity of underspread WSSUS fading channels in the wideband regime," in *Proc. IEEE Int. Symposium on Information Theory (ISIT)*, (Seattle, WA), pp. 1500–1504, July 2006.

[57] K. Soonman and D. R. Fuhrmann, "Sampling theorems for linear time-varying systems with bandlimited inputs," in *Proc. IEEE ICASSP '99*, pp. 1385–1388, Mar. 1999.

[58] P. Hoeher, "A statistical discrete-time model for the WSSUS multipath channel," *IEEE Trans. Veh. Technol.*, vol. 41, pp. 461–468, Nov. 1992.

[59] C. Sgraja and C. Xiao, "On discrete-time modeling of time-varying WSSUS fading channels," in *Proc. IEEE ICC '06*, vol. 12, pp. 5486–5490, June 1999.

[60] H. G. Feichtinger, M. Hampejs, and G. Kracher, "Approximation of matrices by Gabor multipliers," *IEEE Trans. Signal Processing*, vol. 11, pp. 883–886, Nov. 2004.

[61] T. Hunziker and S. Stefanatos, "Efficient two-dimensional filters for doubly-dispersive channel estimation in time-frequency signal processing," in *Proc. Int. Symp. on Spread Spectrum Techn. and Appl. (ISSSTA '08)*, (Bologna, Italy), pp. 381–385, Aug. 2008.

[62] H. G. Feichtinger and K. Nowak, "A first survey of Gabor multipliers," in *Advances in Gabor Analysis*, (Boston, MA), pp. 99–128, Birkhäuser, 2002.

[63] S. Boyd and L. Vandenberghe, *Convex Optimization*. West Nyack, NY: Cambridge University Press, 2004.

[64] J. Renegar, *A Mathematical View of Interior-Point Methods in Convex Optimization*. Philadelphia, PA: SIAM, 2001.

[65] C. Roos, T. Terlaky, and J. P. Vial, *Interior Point Methods for Linear Optimization*. Berlin: Springer, 2006.

[66] K. C. Toh, M. J. Todd, and R. H. Tutuncu, "SDPT3 a MATLAB software package for semidefinite programming," *Optimization Methods and Software*, vol. 11, pp. 545–581, 1999.

[67] G. H. Golub and C. F. V. Loan, *Matrix computations*. Baltimore, MD, USA: Johns Hopkins University Press, 3rd ed., 1996.

[68] A. J. E. M. Janssen and P. L. Soendergaard, "Iterative algorithms to approximate canonical Gabor windows: Computational aspects," *Fourier Analysis and Applications*, pp. 211–241, Jan. 2006.

[69] M. Jankiraman, *Space-Time Codes and MIMO Systems*. Norwood, MA: Artech House Publishers.

[70] P. Hoeher, S. Kaiser, and P. Robertson, "Two-dimensional pilot-symbol-aided channel estimation," *Proc. IEEE Int. Conf. Acoustics, Speech , Signal Processing*, pp. 1845–1848, Apr. 1997.

[71] G. Stewart, *Matrix Agorithms: Eigensystems*. Philadelphia, PA: SIAM, 1998.

[72] J. Liang, B. Ng, J. Chen, and A. Paulraj, "GMSK linearization and structured channel estimate for GSM signals," in *Proc. IEEE Military Commun. Conf. (MILCOM 97)*, (Monterey, CA), pp. 817–821, Nov. 1997.

[73] *Mobile WiMAX Part I:A Technical Overview and Performance Evaluation*. WiMAX Forum, 2004.

[74] M. S. Gast, *802.11 Wireless Networks: The Definitive Guide*. Sebastopol, CA: O'Reilly Media, 2002.

[75] H. Holma and A. Toskala, *WCDMA for UMTS: Radio Access for Third Generation Mobile Communications*. NY, USA: John Wiley & Sons, 2002.

[76] G. Calcev, D. Chizhik, B. Goransson, S. Howard, H. Huang, A. Kogiantis, A. Molisch, A. Moustakas, D. Reed, and H. Xu, "A wideband spatial channel model for system-wide simulations," *IEEE Trans. Veh. Technol.*, vol. 56, pp. 389–403, Mar. 2007.

[77] *3rd Generation Partnership Project; Technical Specification Group Radio Access Network; User Equipment (UE) radio transmission and reception (FDD) (Release 6)*. http://q-t.jp/3GPP/Specs/25101-6c0.pdf.

[78] S. Stefanatos and A. Polydoros, "Gabor-based waveform generation for parametrically flexible, multi-standard transmitters," in *European Signal Processing Conference (EUSIPCO-2007)*, pp. 871–875, Sept. 2007.

[79] H. Puska and H. Saarnisaari, "Matched filter time and frequency synchronization method for OFDM systems using PN-sequence preambles," in *Proc. IEEE PIMRC'07*, (Athens, Greece), pp. 1–5, Sept. 2007.

[80] A. Kliks and H. Bogucka, "The application of the water-filling principle for generalized multicarrier signals," in *Proc. 13th International OFDM-Workshop 2008 (InOWo'08)*, (Hamburg, Germany).

[81] *Uranus Deliverable 5.2: Building Blocks for the Validation Platform*. http://www.IST-URANUS.org/.

[82] *Uranus Deliverable 5.6: Validation Platform Performances Report*. http://www.IST-URANUS.org/.